Copyright statement

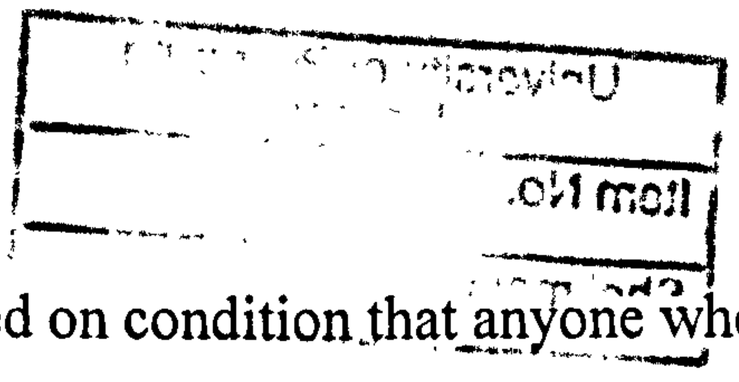

This copy of the thesis has been supplied on condition that anyone who consults it is understood to recognise that its copyrights rests with its author and that no quotation from the thesis and no information derived from it maybe published without the author's prior consent.

Signed

R.C.N. Cherukuru

REMOTE SENSING OF OPTICALLY ACTIVE MARINE COMPONENTS

by

RAGHU CHANDRA NAGUR CHERUKURU

A thesis submitted to the University of Plymouth
in partial fulfilment for the degree of

DOCTOR OF PHILOSOPHY

School of Earth, Ocean and Environmental Sciences
Faculty of Science

In collaboration with
Plymouth Marine Laboratory

October 2004

To my parents and teachers

Abstract

REMOTE SENSING OF OPTICALLY ACTIVE MARINE COMPONENTS

by

RAGHU CHANDRA NAGUR CHERUKURU, M.Sc [Technology].

Remote sensing is an efficient tool to monitor the aquatic ecology. The optical signature in coastal marine environment is a reflection of the complex distribution of optically active marine components. It is essential to understand the relationship between the remote sensing signal and marine constituent material to take advantage of high resolution remote sensing data available from spaceborne and airborne platforms. The objective of this research was to develop a semi-analytical forward model to predict the remote sensing optical signature in coastal waters dominated by non-planktonic material. Laboratory and *in situ* measurements collected over a 5 year period (1998-2003) were used to compile a biogeooptical database for coastal waters. The database is exploited to realise various biogeophysical relationships. A major advancement proposed in the thesis towards the modelling of backscattering probability was the synthesis of knowledge from Mie theory and particulate composition from geochemical analysis. This approach was used to derive particulate backscattering from *in situ* absorption and attenuation measurements. Results show that this model can produce backscattering values in a realistic way than with a constant value as proposed by Petzold. Absorption and backscattering values derived from ac-9 measurements were used to calculate radiance reflectance and remote sensing reflectance. The biogeophysical relationships developed were incorporated into the forward optics model to successfully simulate the inherent optical property ratio. Further development of the model and applications through inversion were discussed and outlined.

List of Contents

List of Figures

List of Tables

Acknowledgements

I would like to take this opportunity to express my heartfelt gratitude, to all the people who have helped and encouraged me throughout this period of study.

I thank both my supervisors Dr. S. J. Lavender (University of Plymouth) and Prof. James Aiken (Plymouth Marine Laboratory) for their support, advice and guidance. I am particularly indebted to Prof. James Aiken for resourcing my work and enabling access to facilities at PML.

I am indebted to Mr. G. F. Moore for his guidance and advice with optical modelling and investigations.

I am also indebted to Dr. P. Pascoe, Dr. G. H. Tilstone, Prof. G. Millward, Dr. Tony Bale, Mr. J. Fishwick, Dr. V. Abbott, Dr. D. Doxaran, Dr. T. J. Smyth and Mr. Y. Pradhan for their help and advice at various stages of my study.

I thank Dr. D. Perrie (CSM) and Dr. E. Aietchbergh (SEOES, UoP) for providing XRD and ICPAES results.

I thank the Masters and crew of RV Squilla for their help in providing weekly water samples from Plymouth Sound.

My thanks to all my friends and family for their never ending encouragement.

Authors declaration

At no time during the registration for the degree of Doctor of Philosophy has the author been registered for any other University award.

This study was financed by the University of Plymouth and carried out in collaboration with Plymouth Marine laboratory.

The word count of this thesis is 34,957.

Publications

Samantha Lavender and C.R.C.Nagur. (2002).Mapping UK coastal waters with high resolution imagery, Journal of Optics A: Pure and Applied Optics., 4, No 4, S50.

D Doxaran, R C Nagur Cherukuru and S J Lavender. (2004). Estimation of surface reflection effects on upwelling radiance field measurements in turbid waters Journal of Optics A: Pure and Applied Optics, 6, No 7, 690-697.

D Doxaran, R C Nagur Cherukuru and S J Lavender. (2004) Use of reflectance band ratios to estimate suspended and dissolved matter concentrations in estuarine waters. Int. Journal of Remote Sensing. (accepted - August 2004)

D Doxaran, R C Nagur Cherukuru and S J Lavender. (2004) Use of spectralon panel to measure the downwelling irradiance signal: case studies and recommendations. Applied Optics. November, 2004.

Conference contributions

Nagur, CRC. and Lavender, S.J. Mapping of suspended sediment in the Tamar estuary, NERC Airborne Remote Sensing Facility Workshop, RAL, Dec., 2002.

Lavender, S. and Nagur, C. Mapping of processes in the Plymouth coastal zone and Tamar estuary. Challenger Centenary Conference: Marine Science, Plymouth, September. 2002.

Lavender, S.J., Cherukuru, R.C.Nagur. and Doxaran, D. Identification and Classification of Bio-geophysical Parameters in Plymouth Coastal Waters, UK. ASLO/TOS 2004 Ocean Research Conference, Hawaii, February. 2004.

D Doxaran, R C Nagur Cherukuru and S J Lavender Mapping suspended solids in turbid esturine waters using airborne imagery. NERC EO Conference, June 2004.

Signed..... Date...24/02/2005

Chapter 1 : Introduction

1.1 Rationale for research

The effects of climate change and the pressure of human population growth have significant impacts on coastal environment and their communities (UNESCO 2003). Predicted effects of climate include sea-level rise and increased frequency and intensity of storms with accompanying coastline erosion, river discharge and sedimentation. Human activities in catchments, such as, mining, dams, agriculture and industrial development can all result in major changes in the volume and pattern of runoff, and in increased loads of nutrients and suspended sediments into estuaries and adjacent coastal waters. Changes in the pattern of freshwater runoff (due to catchment modification) may profoundly affect circulation and salinity regimes in estuaries and adjacent coastal regions, with impacts on key habitats and on fish recruitment.

The development and maintenance of coastal infrastructure often resuspends sediments. This can result in a temporary or permanent increase in light attenuation, loss of benthic habitat through shading and remobilization of contaminants and organic matter (IOCCG 2000). Land-derived materials (e.g. sediments, nutrients, and carbon) are massively injected into the coastal zone at specific locations such as river mouths and estuaries, and therefore any changes in these inputs from human activities can have major consequences for the entire sediment and carbon balance of the coastal waters.

Thus, the coastal marine environment is a sensitive environment, which has a strong influence on the economic, social and health of human population living in the coastal zone. The heavy pressures placed on the coastal environments and ecosystems through growth and concentration of human population, activity and resource utilisation pose enormous challenges for coastal monitoring.

Monitoring marine systems has always been difficult and expensive, but adequate monitoring at appropriate spatial and temporal scales is essential to support coastal environment monitoring. Coastal environment is generally influenced by optically active mineral particles in suspension, particulate and dissolved humic substances

along with non dominant phytoplankton (IOCCG, 2000; Doerffer, 1992). Optical investigations can provide good estimates of these constituent materials. An understanding of the optical signature can provide links towards the biogeochemical status of the environment.

Advancements in spaceborne and airborne ocean colour technology, with its ability to monitor at a wide range of time and space scales, can play a critical role. When these advances in remote sensing are synchronised with knowledge from *in situ* measurement and advances in our ability to model coastal systems and assimilate satellite and *in situ* data, a positive confidence can be achieved (UNESCO 2003).

This Ph.D. focuses on improving the confidence in coastal environmental monitoring by developing a forward model with region specific *in situ* measurements, to predict the optical signature in such complex environments. The forward approach (when used in combination with remotely sensed data) can provide high resolution biogeophysical maps. Availability of such detailed information can greatly support the managers in decision making for coastal zone management.

1.2 Objectives of research

This research aims at developing a forward model that can explain the optical signature in coastal waters. Plymouth coastal waters are chosen as the study area for this research due to availability of historical data and access to the weekly sampling. These waters are dominated by non-planktonic material (except in summer) which influence the underwater optical environment (COLORS 2001). As a first step towards understanding this optical environment, this research focuses on developing the forward model which can explain the optical signature in the presence of dominant non-planktonic material and plans to include the contribution of planktonic material in future research.

To achieve the objective, the research is structured into the following tasks:

- To collect and compile a knowledge base of biogeooptical measurements representative of the optical domain.
- To understand and model the relationships between inherent optical properties and optically active marine constituents.
- To develop a forward model to predict the above water optical remote sensing signal.

1.3 Thesis overview

It is essential to understand the nature of light before attempting to investigate its interaction with material in an aquatic medium. The nature of light, its propagation and ability to interact with the containment medium are explained in Chapter 2. The source and nature of light (Sections 2.1-2.2) and photon matter interactions (Section 2.3) at atomic level are used to explain the inherent optical properties. Aquatic optics is introduced in Section 2.5, both inherent and apparent optical properties are defined and various interrelationships are explained.

Chapter 3 is an introduction to biogeooptics of coastal waters. Various optically active components in the coastal waters are introduced. The origin of various bio-geophysical components and their domination in natural waters is discussed. The specific optical nature of each of these optically active marine constituents is explained along with their ability to interact with light. Finally their contribution towards the above water remote sensing signal is explained (Section 3.3).

Measurements and methodology followed are explained in Chapter 4. Data was collected and compiled from two major sources (COLORS and UoP-PML research projects) to achieve the objective of this research. The data is processed following the protocols of COLORS. The PML Bio-optics rig is introduced in Section 4.7.

Chapter 5 deals with the dynamics of the coastal marine optical environment. This chapter, structured into 3 sections presents the results achieved in this research. Section I presents the *in situ* data and observations that introduce the boundaries of

the variations in biogeophysical measurements. Section II outlines and models the particulate interaction behaviour. Section III introduces different biogeooptical relationships and incorporates them into the model to predict the optical signature. Finally, Chapter 6 discusses the results obtained from the research, its application and future research.

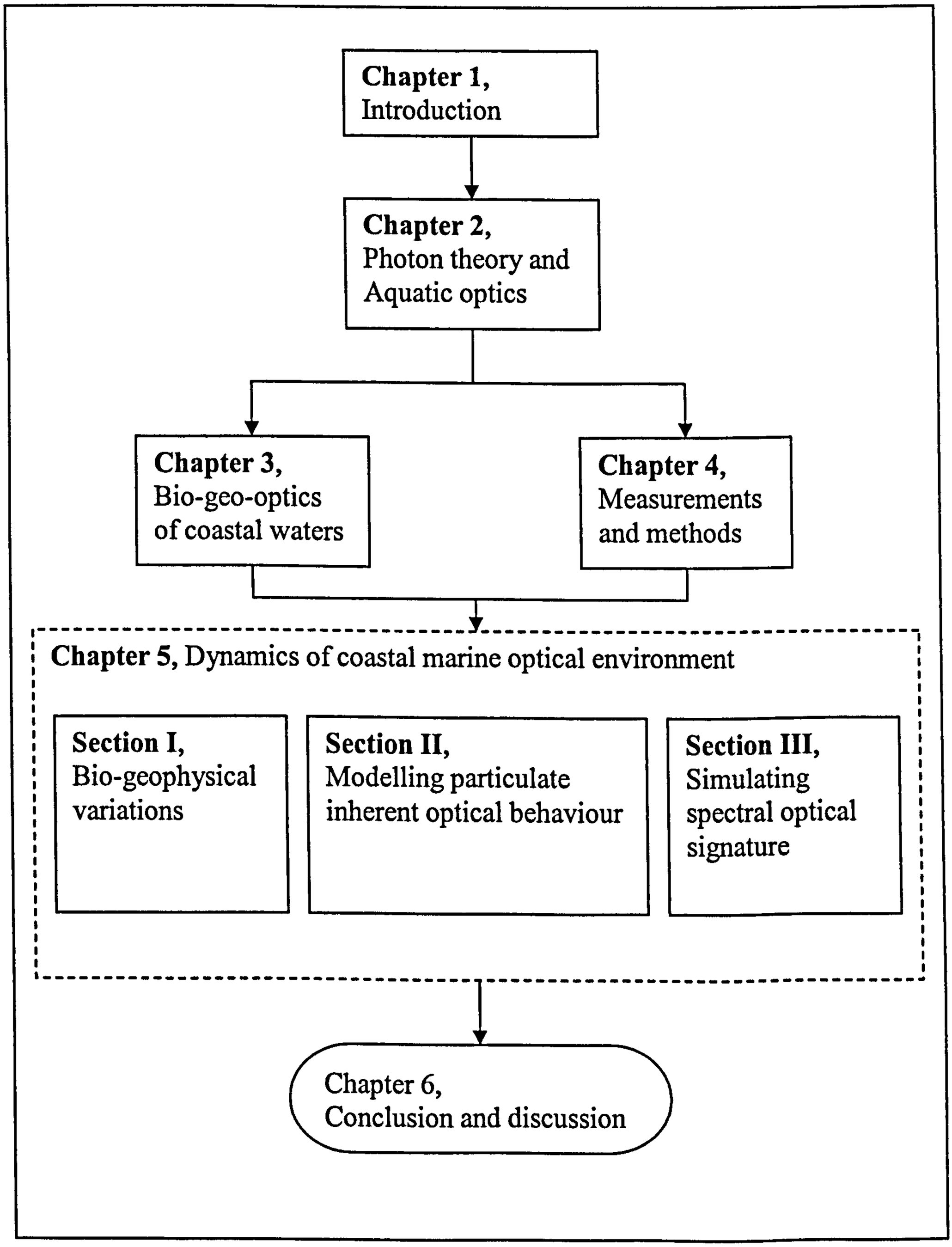

Figure 1.1: The structure of thesis

Chapter 2 : Photon theory and Aquatic optics

It is very important to understand the source, basic structure and behaviour of light before attempting to investigate its interactions with its containment medium. Aquatic optics further explains different possible interaction mechanisms that light may involve while propagating through natural water.

2.1 Nuclear reactions in the Sun and light

Most of the extraterrestrial energy reaching the earth originates in the Sun. The Sun shines by a sequence of nuclear reactions, called proton-proton chain. This proton-proton chain occurs basically at temperatures of 10 to 20 * 10^6 K and densities of about 100 gm cm^{-3} (Audouze and Vauclair, 1980). It is the basic nuclear process that occurs inside the sun, which is a highly dense mixture of completely ionized Hydrogen and Helium.

In the first step of the proton-proton chain, two protons (hydrogen nuclei) are fused to form a deuteron, the nucleus of a heavy form of hydrogen known as deuterium. Since a deuteron consists of one proton and one neutron, one of the protons entering the reaction must be transformed into a neutron, emitting a positron, to carry away the proton's charge, together with a low-energy neutrino, to balance the energy in the reaction (Lang, 1995).

$$proton + proton \rightarrow deuteron + positron + neutrino \qquad \text{eq (2.1)}$$

Part of the energy liberated during this reaction is converted into radiation when an electron collides with a positron. Then matter and anti-matter annihilate each other to produce photons at short gamma ray wavelengths. This radiation-producing interaction can be written as:

$$positon + electron \rightarrow photon \qquad \text{eq (2.2)}$$

In the next step the deuteron in eq (2.1) collides with another proton to form a nucleus of light Helium, He^3.

$$deuteron + proton \rightarrow He^3 + photon \qquad \text{eq (2.3)}$$

This reaction also creates a photon, which in fact carries most of the energy released in the reaction. He^3 nuclei are in turn able to fuse with each other in the final step of the proton-proton chain.

$$He^3 + He^3 \rightarrow He^4 + 2protons \qquad \text{eq (2.4)}$$

There are exothermic reactions other than the proton-proton chain, like the CN cycle, which involves heavy Carbon and Nitrogen. The CN cycle involves the collision of protons with those elements to build up He nuclei; the higher nuclear charge of C and N produces a strong electrostatic repulsion and much steeper temperature dependence. This restricts the CN cycle to be dominant in stars hotter than the Sun (Zirin, 1988).

The various photons created in the proton-proton chain are all extremely energetic (gamma radiation). They strongly interact with the matter and undergo repeated scattering, absorption and re-emission on their way towards the surface of the sun. The photons lose energy in these interactions, so that they are predominantly in the visible and infrared parts of the spectrum by the time they arrive at the surface of the Sun and escape into space towards earth.

2.2 Nature of light

Light is neither particles or waves; it is somehow both, and only shows one or other aspect depending on the experiment conducted. More exactly, the particle nature of light is an artefact of material observation. It is not, in fact, the nature of the light, but the nature of observations, which has particle attributes. The quantized behaviour of light prompts physicists to treat it as a particle. Again, the zero mass of the photon is another hurdle in continuing with this assumption. Our inability to classify light is not so much a failure to understand the nature of light as it is a failure of our limited vocabulary (based on the experiences with ordinary particles and waves) to describe a phenomenon that is more elegant and mysterious than either simple particles or waves (Krane, 1996). The complete picture, which unifies the whole thing into one model, will not be available to us for a long time (Feynman *et al.*, 1966). This dilemma of

wave-particle (continuous - quantised energy) duality, which is a general property of nature, can not be resolved with a single explanation. The best thing one can do is to accept this duality as the nature and that both the explanations are complimentary to one another. Certainly physicists are still trying to understand this concept. Section 2.2, aims at exploring different explanations and the current understanding of the nature of light and its relevance in explaining the interactions of light in an aquatic medium.

2.2.1 Wave nature of light

Equations 2.5, 2.6, 2.7 and 2.8 are called Maxwell's equations; they play an important role in classical electromagnetism. In principle, all problems in electricity and magnetism can be solved using Maxwell's equations (Tipler, 1999).

$$\oint_s E_n \, dA = \frac{1}{\varepsilon 0} Q_{inside} \qquad \text{eq (2.5)}$$

$$\oint_s B_n \, dA = 0 \qquad \text{eq (2.6)}$$

$$\oint_c \vec{E} \cdot \vec{dl} = -\frac{d}{dt} \int_s B_n \quad dA \qquad \text{eq (2.7)}$$

$$\oint_c \vec{B} \cdot \vec{dl} = \mu_0 I + \mu_0 \varepsilon_0 \frac{d}{dt} \int_s E_n \quad dA \qquad \text{eq (2.8)}$$

Equation 2.5 is Gauss's law; it states that the flux of the electric field (E_n) through any closed surface equates to $1/\varepsilon_0$ (ε_0 is called the permittivity of free space) times the net charge inside (Q_{inside}) the surface. Gauss's law implies that the electric field due to point charge varies inversely as the square of the distance from the charge. This law describes how electric field lines diverge from a positive charge and converge on a negative charge. Its experimental basis is Coulomb's law.

Equation 2.6, sometimes called Gauss's law for magnetism, states that the flux of the magnetic field vector $\vec{B}$ is zero through any closed surface. This equation describes the experimental observation that magnetic field lines do not diverge from any point in space or converge on any point; that is, it implies that isolated magnetic poles do not exist.

Equation 2.7 is Faraday's law; it states that the integral of the electric field around any closed curve C, which is the electro motive force (emf), equals the negative rate of change of the magnetic flux through any surface S bounded by the curve. Faraday's law describes how electric field lines encircle any area through which the magnetic flux is changing, and it relates the electric field vector $\vec{E}$ to the rate of change of magnetic field vector $\vec{B}$.

Equation 2.8, Ampère's law modified to include Maxwell's displacement current, states that the line integral of the magnetic field $\vec{B}$ around any closed curve C equals to μ_0 (permeability of free space) times the current through any surface bounded by the curve plus $\mu_0\varepsilon_0$ times the rate of change of electric flux through the surface. This law describes how the magnetic field lines encircle an area through which a current is passing or through which the electric flux is changing.

Figure 2.1 shows the electric and magnetic field vectors of an electromagnetic wave. The electric and magnetic fields are perpendicular to each other and perpendicular to the direction of propagation of wave. Electromagnetic waves are thus transverse waves. Maxwell showed that equations 2.5,2.6,2.7 and 2.8 can be combined to yield a wave equation for the electric and magnetic field vectors $\vec{E}$ and $\vec{B}$. Such electromagnetic waves are caused by accelerating charges. In such waves magnitudes of $\vec{E}$ and $\vec{B}$ are in phase and are related by (Tipler, 1999)

$$E = c\,B \qquad \text{eq (2.9)}$$

$$\text{and } c = 1/\sqrt{\mu_0\varepsilon_0} \qquad \text{eq (2.10)}$$

where ε_0, the permittivity of free space, is the constant appearing in Coulomb's and Gauss's laws and μ_0, the permeability of free space, is the constant appearing in the Biot - Savart's law and Ampère's law. When the measured and defined values of ε_0 and μ_0 are used in equation 2.10, the value is found to be around $3 * 10^8$, the same as the measured speed of light. This coincidence was noted by Maxwell and he correctly summarised that light itself is an electromagnetic wave.

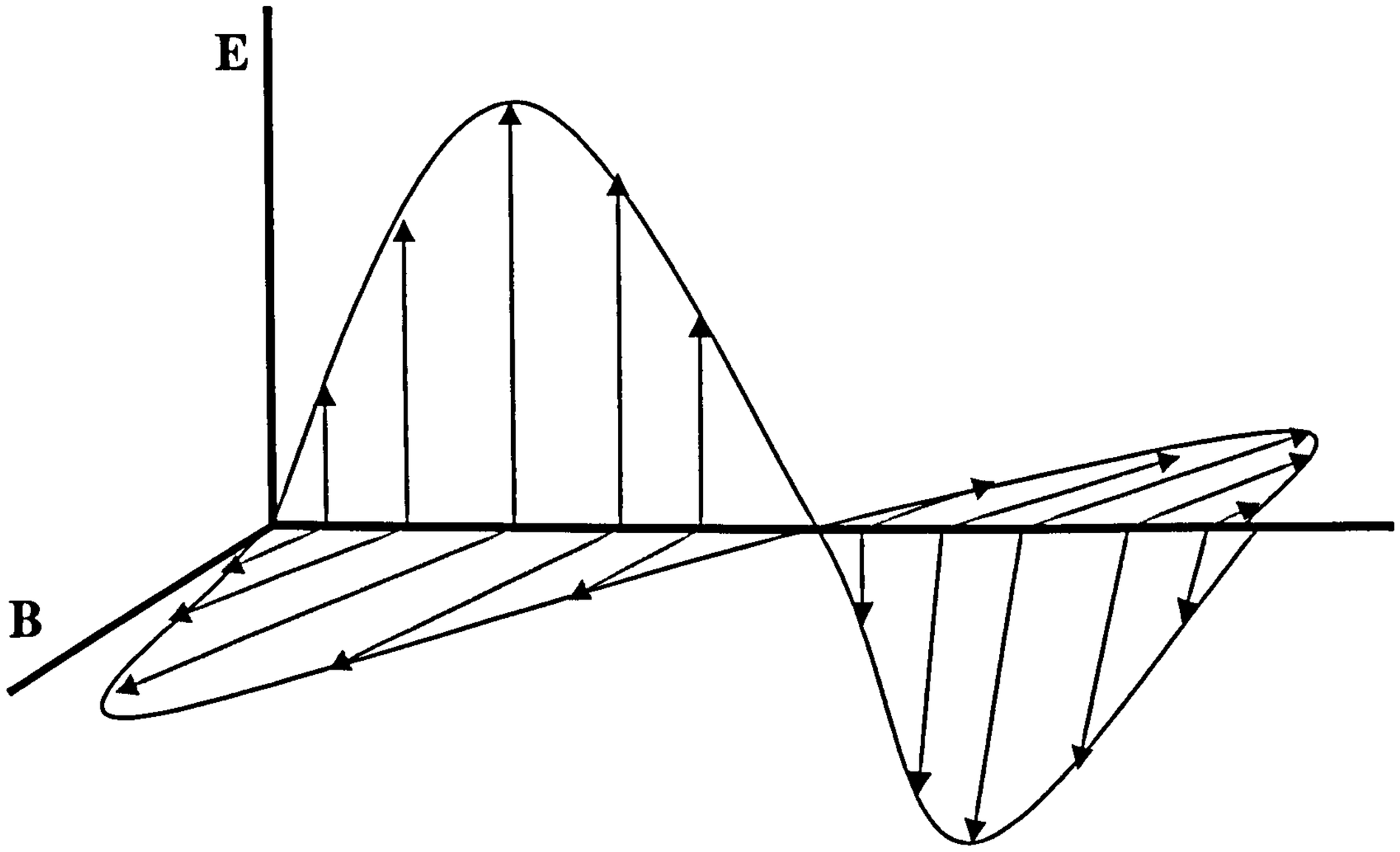

Figure 2.1: Electric (E) and magnetic (B) field vectors of an electromagnetic wave

2.2.2 The Quantization of Light

Quantum physics is largely the study of microscopic world. Many quantities are found only in a certain minimum amount, or integer multiples of those elementary amounts; they are then said to be quantized. The elementary amount that is associated with such a quantity is called the quantum of that quantity.

The first clue as to the quantum nature of the radiation came from the study of radiation emitted by opaque bodies. Stefan-Boltzman's law gives an empirical relation between the power per unit area radiated by a black body and the temperature.

$$W = \sigma T^4 \qquad \text{eq (2.11)}$$

Where W is the power per unit area, T is the absolute temperature and $\sigma = 5.6703*10^{-8}$ W m^{-2} K^4 is a constant called Stefan's constant. Note that the power per unit area depends only on the temperature, and not on any other characteristic of the object. The same is true of the spectral distribution of the radiation emitted by a blackbody.

The dominant wavelength, or wavelength at which a blackbody radiation curve reaches a maximum is related to its temperature by Wien's displacement Law,

$\lambda_m = A/T$ eq (2.12)

where

λ_m = wavelength of maximum spectral radiant exitance, μm

A = 2898 μm K

T = temperature, K

Thus for a blackbody, the wavelength at which the maximum spectral radiant exitance occurs varies inversly with the blackbody's absolute temperature.

The calculation of the distribution function, $W(\lambda)$, involves the calculation of the energy density of electromagnetic waves in a cavity. The spectral distribution of the power emitted from the cavity hole is proportional to the spectral distribution of the energy in the cavity

$W(\lambda) = 1/4 * c * u(\lambda)$ eq (2.13)

The energy-density distribution function, $u(\lambda)$, can be calculated from classical physics in a straightforward way. The classical theory predicts the spectral distribution function as

$u(\lambda) = 8\pi kT\lambda^{-4}$ eq (2.14)

Where kT is the average energy per mode of the oscillation of electromagnetic field in the cavity. This prediction (eq 2.14) is called Rayleigh-Jeans law. At very long

wavelengths the Rayleigh-Jeans law agrees with the experimentally determined spectral distribution, but at short wavelenghts this law predicts that $u(\lambda)$ becomes infinite whereas experiments show that the distribution approaches zero. This result was called ultraviolet catastrophe.

After the failure of the Rayleigh-Jeans law in explaining the energy distribution, in 1900 Max Planck announced that he could derive a function $u(\lambda)$ which agreed with the experimental data (Tipler 1999). Plank found that he could derive his emprical function by calculating the average energy $\bar{E}$ ($\bar{E} = kt$) assuming the energy to be a discrete variable. He therefore wrote the energy as

$$E_n = n\,\varepsilon = nh\nu \qquad n = 0,1,2,3..... \qquad \text{eq (2.15)}$$

Where n is an integer, ε is proportional to the frequency (ν) of the radiation and $h = 6.626*10^{-34}$ [J s] (a constant now called Plank's constant).

The fundamental importance of the quantization assumption implied by equation 2.15 was not generally appreciated until 1905. In that year Einstein applied the same ideas to explain the photoelectric effect and suggested that, quantization is the fundamental characteristic of light energy. A particle of light called a photon has energy (E) that is related to ν and the wavelength (λ) of the light wave by the Einstein equation

$$E = h\nu = hc / \lambda \qquad \text{eq (2.16)}$$

In 1916, Einstein extended his concept of light quanta by proposing that a quantum of light has linear momentum. For a photon with energy $h\nu$, the magnitude of the momentum is

$$p = h\nu / c = h / \lambda \qquad \text{eq(2.17)}$$

Further evidence of the correctness of the photon concept was furnished by Authur H. Compton in 1923 (Tipler 1999). In his experiments, he directed a monochromatic

beam of X-rays at a thin slab of low element material, such as carbon. He observed that the X-rays that

were scattered from the carbon at various angles had a longer wavelength (λ') than that of the incident wavelenght (λ_0). The amount of wavelength shift, $\Delta\lambda = \lambda'-\lambda_0$, was the same regardless of the target material, implying it is an effect involving electrons rather than an atom as a whole.

Compton invoked the photon model to explain the results from his experiments. He supported equations (2.16 and eq 2.17) for energy and momentum of the photon from Einstiens explanations.

According to relativity, energy and mass are related by $E= mc^2$. Using this relationship in the equation of energy of a photon (eq 2.16), we have

$$h\nu= mc^2 \qquad \text{eq (2.18)}$$

If the photon travels with a speed of c, their momentum is p=mc, which, from equation (2.18), becomes

$$p = h\nu / c = h / \lambda \qquad \text{eq (2.19)}$$

Following a relatevisitic explanation for photon - matter collision, the relationship between energy and momentum is

$$E^2 = (pc)^2 + (mc^2)^2 \qquad \text{eq (2.20)}$$

since the momentum of the photons is $p = E / c$, it becomes clear that the rest mass term in equation (2.20) must be zero. At the same time, it is also important to note that massless particles travel at the speed of light; otherwise, their reletevistic kinetic energy and the total energy would become zero.

2.3 Photon - matter interactions

The most common interaction of the photon with the matter initiates the transition of the outer electrons in the atom of the matter. Normally an atom is in its ground state, with its electrons at their lowest allowed energy levels, which is consistent with the exclusion principle (states that no two electrons in an atom can be in the same quantum state). The lowest energy electrons are closest to the nucleus and are tightly bound, forming a stable inner core. The one or two electrons in the highest energy states are much farther from the nuclues and are relatively easily excited to vacant higher energy states. The outer electrons are reponsible for the energy changes in the atom that result in the emission or absorption of visible light.

When an atom interacts with a photon, its outer electrons are excited to higher energy states. After a time of 10^{-8} s , these outer electrons spontaneously make transitions to lower energy states with the emission of a photon. This process, called spontaneous emission, is random; the photons emitted from two different atoms are not correlated. The emitted light is thus incoherent. By conservation of energy, the energy of an emitted photon is the energy difference $\Delta E = h\nu$. The wavelength of the emitted light is then

$$\lambda = c / \nu = hc / h\nu = hc / \Delta E \qquad \text{eq (2.21)}$$

When atoms are close together and interact strongly, as in liquids and solids, the energy levels of the individual atoms spread out into energy bands, resulting in essentially continuous bands of energy levels. When these bands overlap, as they often do, the result is a continuous emission spectrum.

2.3.1 Photon absorption

All substances contain negatively charged electrons that oscillate around the positively charged nuclei of the contributing atoms or molecules. In photon-matter interaction, the electrical component of the incident light can interact with the electronic structure of the atoms or molecules and induce a transient displacement of the electrons with repect to the nuclei. This interaction mechanism is termed as absorption. The energy absorbed by the atom or molecule will be transformed into radiation, thermal or chemical energy depending on the nature of the matter.

In atoms, the absorption of light occurs in clearly defined, narrow wavelengths that correspond to specific shell designations. In the formation of molecules, electrons are shared between atoms, forming bonds, and a great multiplicity of quantum configurations becomes possible, leading to absorption bands that are symmetrical around a maximum.

Figure 2.2 illustrates several interesting phenomena that can occur when a photon interacts with matter. In Figure 2.2c, the energy of the incident photon is just equal to the difference in energy between the ground state and the first excited state of the atom. The atom makes a transition to the first excited state and then after a short delay decays by spontaneous emission back to the ground state with the emission of a photon whose energy is equal to that of the incident photon. The phase of the emitted photon is not correlated with the phase of the incident photon. This multistep processes is called resonance absorption.

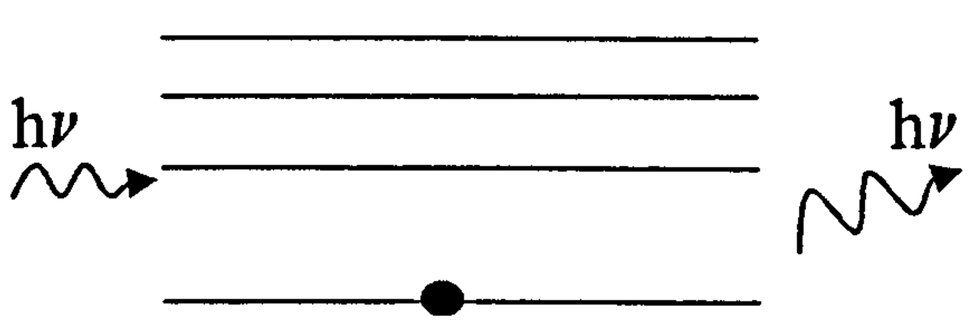

(a) Elastic scattering

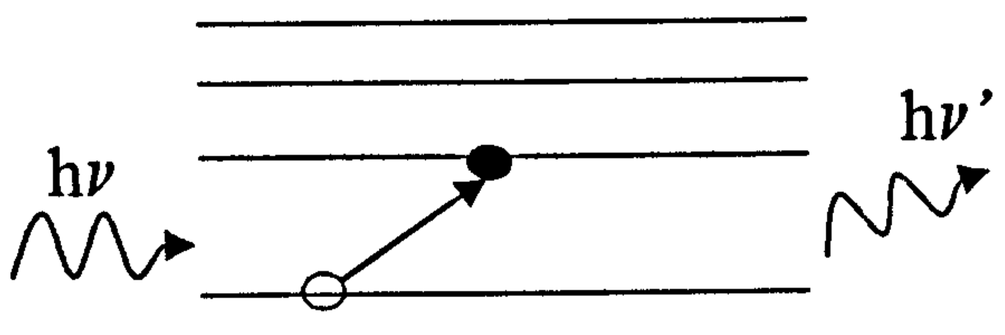

(b) Inelastic scattering

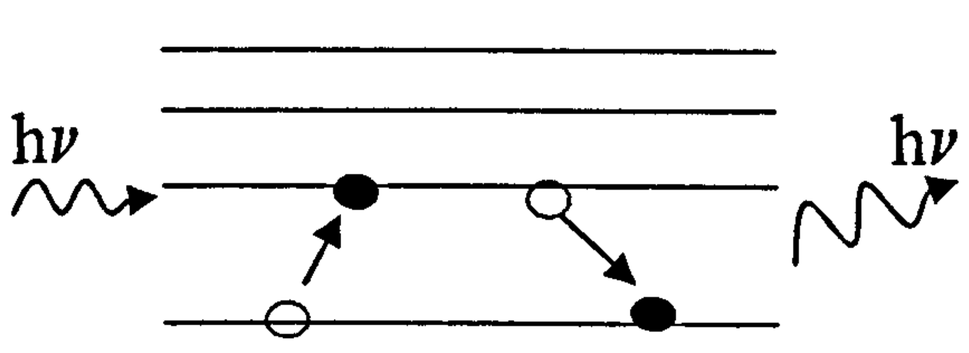

(c) Resonance absorption

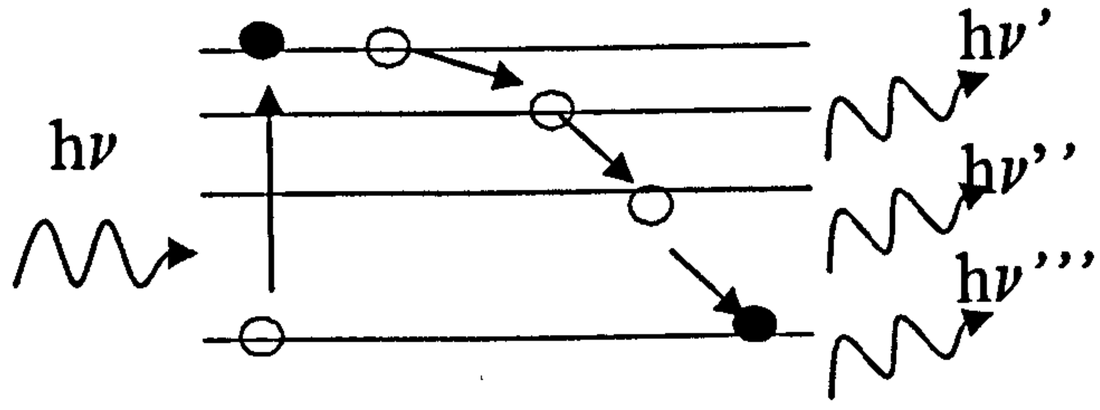

(d) Fluorescence

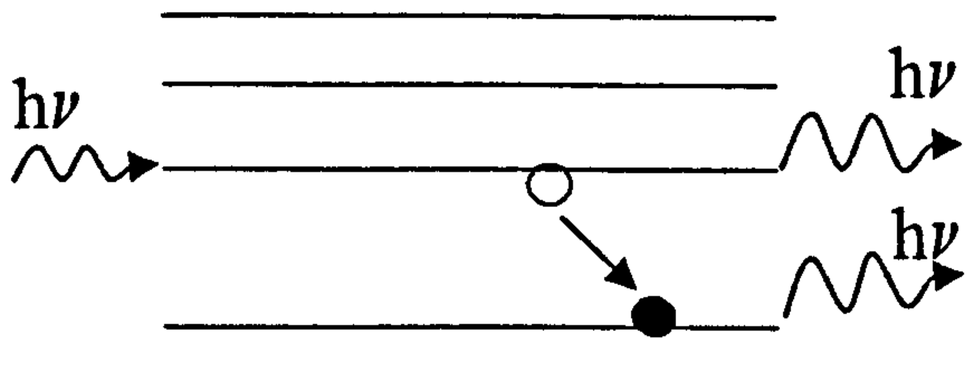

(e) Stimulated emission

Figure 2.2: Photon matter interactions

2.3.2 Photon scattering

Absorption of photon energy by atom or molecule leads to displacement of the electrons. Photons are radiated when these electrons transit back to the ground state. These resulting photons have different path directions and this process of influencing the direction of the photon propogation is called scattering.

In Figure 2.2(a), the energy of the incoming photon is too small to excite the outer electron to an excited level, so the electron remains in its ground state and the photon is said to be scattered. Since the incoming and outgoing or scattered photons have the same energy, the scattering is said to be elastic.

Figure 2.2(b) shows inelastic scattering, which occurs when the incident photon has enough energy to cause the atom to make a transition to an excited state. The energy of the scattered photon (hν') is less than that of the incident photon (hν) by ΔE, the difference between the energy of the ground state and the energy of the excited state. Inelastic scattering of light from molecules was first observed by C.V.Raman and is often refered to as Raman scattering.

2.3.3 Fluorescence and stimulated emission

In Figure 2.2(d), the energy of the incident photon is great enough to excite the atom to one of its higher excited states. The atom then loses its energy by spontaneous emission as it makes one or more transitions to the lower states. A common example occurs when the atom is excited by the ultraviolet light and emits visible light as it returns to its ground state. This processes is called fluorescence.

Figure 2.2(e) illustrates stimulated emission. This process occurs if the atom or molecule is initially in an excited state of energy E2, and the energy of the photon is equal to E2-E1, where E1 is the energy of the low state or the ground state. In this case, the oscillating electromagnetic field associated with the incident photon stimulates the excited atom or molecule which then emits a photon in the same direction as the incident photon and in phase with it. In stimulated emission, the phase of the light emitted from one atom is related to that emitted by every atom, so the resulting light is coherent.

2.4 The propagation of light

The propagation of light is governed by the wave equation derived using Maxwell's equations. But long before Maxwell's theory of electromagnetic waves, the propagation of light and other waves was described empirically by two interesting principles viz., Huygens' and Fermat's principle (Tipler, 1999).

The propagation of any wave through space can be described using a geometric method discoverd by Huygens in around 1678, which is now known as Huygens principle. According to this principle, each point on a primary wave front serves as the source of spherical secondary wavelets that advance with a speed and frequency equal to those of the primary wave. The primary wavefront at some later time is the envelope of these wavelets.

The propagation of light can also be described by Fermat's principle: the path taken by the light in travelling from one point to another is such that the time of travel is a minimum.

2.4.1 The speed of light

The first effort to measure the speed of light was made by Galileo. Astronomical and nonastronomical based measurements of the speed of light were made by Ole Romer, Fizeau, Focault, Michelson and others (Tipler, 1999). In about 1850, Foucault measured the speed of light in air and in water and showed that it is less in water(Tipler, 1999). Using essentially the same method, the American physcist A.A.Michelson made precise measurements of the speed of light during 1880 and 1930 (Tipler, 1999).

Another method of determining the speed of light involves the measurements of the electrical constants ε_0 and μ_0 to determine c (equation 2.10). The various methods involved in measuring the speed of light are all in general agreement. Today the speed of light is defined to be exactly $c = 2{,}999{,}792{,}457$ m/s and the standard unit of length, the metre, is defined in terms of this speed. A measurement of the speed of light is therefore now a measurement of the size of the metre, which is the distance light

travels in 1/2,999,792,457 s. The value $3 * 10^{8}$ m/s for the speed of light is accurate enough for nearly all calculations. The speed of radio waves and all other electromagnetic waves is the same as the speed of light.

2.4.2 Reflection and refraction

The speed of light in a transparent medium such as air, water or crystals is less than the speed $c = 3 * 10^{8}$ m/s in vacuum. Electromagnetic wave theory clearly explains this reduction of speed in a medium (for example, in a crystalized mineral) other than vaccum. According to this theory, the dipole moments induced by the incident light oscillate with the same frequency as the incident light, thereby becoming secondary sources of radiation. Because the phasing of the secondary waveform, but not the frequency is changed, the colour of the secondary light remains that of incident light. All the secondary radiators oscillate relative to each other with a fixed phase difference. The secondary electromagnetic waves, generated by each individual light sources, will interfere with each and cancel themselves out in all directions except in the direction of the incident light. The resulting wave form propagates in the direction of the incident light with a reduced velocity (which is a consequence of the phase lag in the resultant wave) . The reduction in velocity of light relative to that in vacuum is called the refractive index, which is a function of the dipole density (the number of atoms or molecules per unit volume) and the strength of the dipole. Under such conditions the angle of incident light is changed but scattering of light is not observed. This phenomenon is called refraction.

If the frequency of light exactly matches the frequency of the oscillation of the dipole of the atoms on the surface of the substance, the electromagnetic radiation cannot penetrate into the substance and is reflected. Hence, reflection is a special case of refraction. The same theory of variation in dipole density can be extended to explain the processes of refraction and reflection at the air-water interface and in water.

In water or other liquids, the density of molecules is so great that the molecules interact and gradients in thermal energy within the fluid cannot be dissipated rapidly enough to permit an isotropic distribution. Consequently, at a moment in time, two adjacent but equal volumes of the fluid will contain slightly different number of

molecules. The minute differences in molecular density lead to temporal and spatial variations in the refractive index. The fluctuations in the refractive index produce incoherences in the phases of secondary (refracted) light, which allows the waveform to propagate in different directions from the primary light source. Hence a collimated beam of light will become more increasingly incoherent (diffuse) as it passes through a liquid. The optical manifestation of this processes is light scattering, and it is a consequence of fluctuations in the refractive index.

2.4.3 Geometric optics

A transparent medium is characterised by the index of refraction, *n*, which is defined as the ratio of the speed of light in a vacuum, *c*, to the speed in the medium, v :

$$n = c / v \qquad \text{eq (2.22)}$$

For water n =1.33, the index of refraction of air is about 1.0003, so for most purposes we can assume the speed of light in air is the same as in a vacuum.

When a beam of light strikes a boundary surface separating two different media, such as an air-water interface (asuming a flat surface), part of the light energy is reflected and part enters the second medium. If the incident light is not perpendicular to the suface, then the transmitted light is not parallel to the incident light. The change in the direction of transmitted light is called refraction.

In Figure 2.3, the angle θ_1 between the incident ray and the normal is called the angle of incidence, and the plane defined by these two lines is called the plane of incidence. The reflected ray lies in the plane of incidence and makes an angle θ_1' with the normal that is equal to the angle of incidence as shown in the figure: $\theta_1' = \theta_1$. This result is known as the law of reflection.

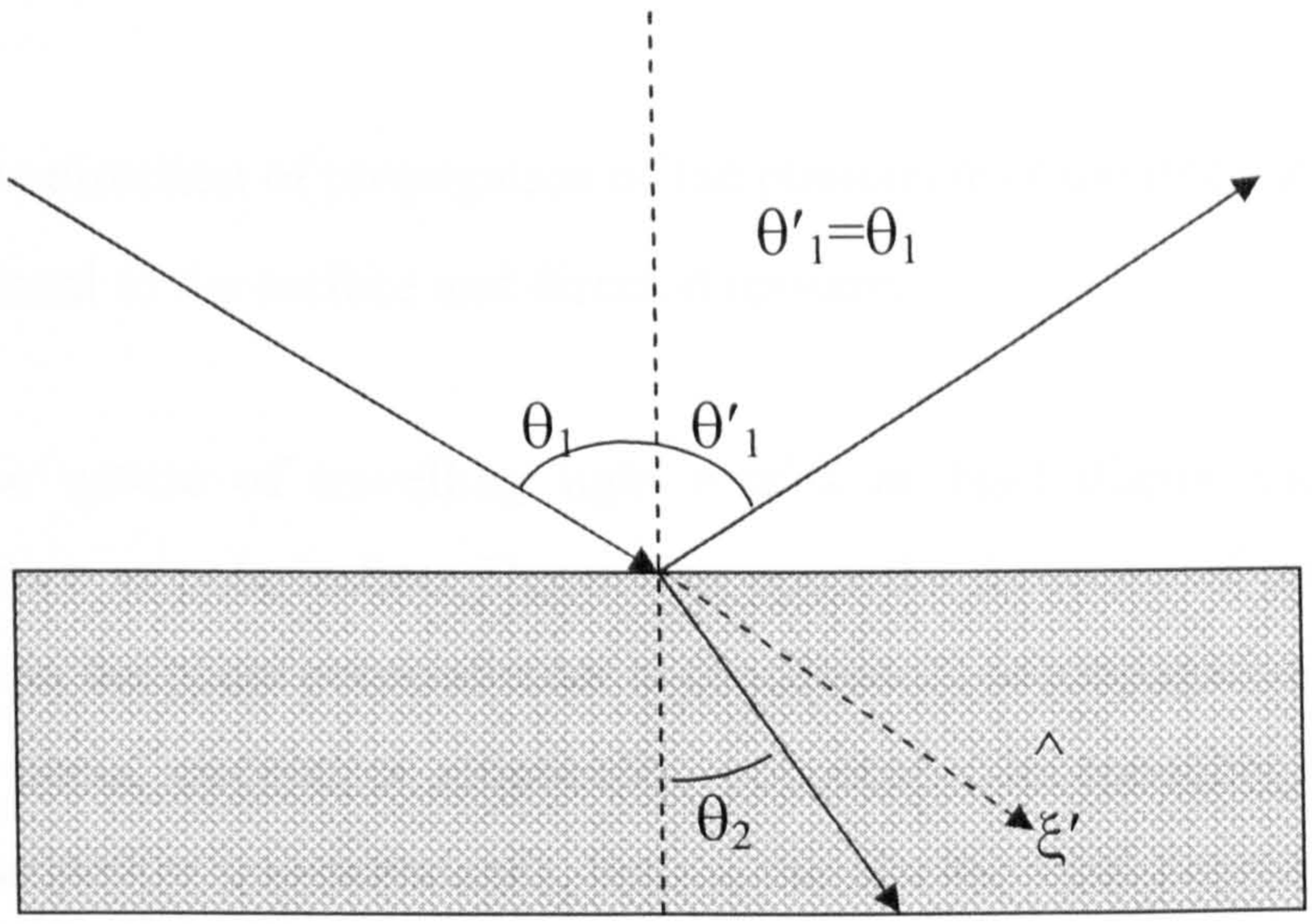

Figure 2.3: Interaction at the interface

The ray that enters the second medium in Figure 2.3 is called the refracted ray and the angle θ_2 is called the angle of refraction. The angle of refraction depends on the angle of incidence and on the relative speed of light waves in the two mediums. If v_a and v_w are the wave speeds in the incident and transmission medium respectively (for example from air to water), then the angles of incidence and refraction are related by

$$(1/v_a)\sin\theta_1 = (1/v_w)\sin\theta_2 \qquad \text{eq (2.23)}$$

In terms of the indexes of refraction of the two media n_a and n_w, Equation 2.23 is

$$n_a \sin\theta_1 = n_w \sin\theta_2 \qquad \text{eq (2.24)}$$

This result was discovered experimentally in 1621 by the Dutch scientist Willebrod Snell and is known as Snell's law or the law of refraction.

The angles of reflection and transmission are given by

$$\theta_1' = \cos^{-1}|\hat{\xi}'\hat{n}| = \theta_1 \qquad \text{eq (2.25 a)}$$

$$\theta_2 = \sin^{-1}\left[\frac{1}{n_w}\sin\theta_1\right] \qquad \text{eq (2.25 b)}$$

where $\hat{\xi}'$ is the direction of propogation of the photons near the interface and $\hat{n}$ is the unit vector normal to the surface and directed upward.

The transverse nature of travelling light results in light displaying a directional behaviour known as polarization. Depending upon the direction of the electric field density vector in the plane perpendicular to the direction of propagation, the travelling light may be plane, circular or elliptically polarized. The travelling light could be randomly polarized(or non-polarized), that is, the electric field density vector has no preffered transverse directionality. When one considers reflection of light from a surface, it is convenient to regard the polarization of incident light flux in terms of a polarization perpendicular to the plane of incidence or polarization parallel to the plane of incidence.

The Fresnel Reflectance formula computes the reflectance at the air water interface. For randomly polarized light (Bukata, 1995) :

$$\rho = \rho\perp + \rho\| \qquad \text{eq (2.26a)}$$

or

$$\rho(\theta_1) = \frac{1}{2}\left\{\left[\frac{\sin(\theta_1-\theta_2)}{\sin(\theta_1+\theta_2)}\right]^2 + \left[\frac{\tan(\theta_1-\theta_2)}{\tan(\theta_1+\theta_2)}\right]^2\right\} \qquad \text{eq (2.26 b)}$$

where $\rho\perp$ and $\rho\|$ are the reflectances for the perpendicular polarized and the parallel polarized components of the incident light, respectively.

It is seen from equation (2.26b) that the reflectance $\rho\|$ becomes zero when $\tan^2(\theta_1+\theta_2)$ becomes infinite(i.e., $\theta_1+\theta_2 = 90°$). Thus when the reflected and transmitted rays are at right angles to one another, it is impossible for light to be reflected, providing its polarizing electric field vector is parallel to the plane of incidence. The angle of incidence at which $\theta_1+\theta_2 = 90°$ is termed as the Brewster angle.

Equation (2.26b) holds if $\theta_1 \neq 0$. In the case of normal incidence, $\theta_1 = 0$ and hence $\theta_1' = \theta_2 = 0$ also. Equation (2.26b) is then indeterminate. In this special case the reflectance is given by

$$\rho(0) = \left[\frac{n_w - 1}{n_w + 1}\right]^2 \qquad \text{(eq 2.27)}$$

Fresnels reflectance lies in the interval $0 \leq \rho(\theta_1) \leq 1$ and gives the fraction of photons incident in a narrow beam along $\hat{\xi}'$ that is reflected by the air water interface.For water-incident rays, the reflectance increases rapidly for θ_1 greater than 30°, and equals one for incident angles greater than or equal to the critical angle $\theta_1 = \sin^{-1}(1/nw) \approx 48°$. This phenomenon of total internal reflection greatly influences the passage of radiant energy across the water-air interface.

2.5 Aquatic optics

Optics is generally defined as that branch of physics concerned with the interactions of light with its containment medium as light propagates through that medium. Aquatic optics generally restricts its definition of containment media to those found in naturally occuring water bodies. This section provides an introduction to radiometry and optical properties relevent to aquatic optics.

2.5.1 Radiometry

Radiometry is the science of the measurement of electromagnetic, or radiant, energy. In descriptions of light propagation in water some radiometric concepts are required. The basic radiometric quantity, the radiant flux Φ, is defined as the time rate of flow of radiant energy and is expressed in Watts [W]. Radiant intensity, I, is a measure of the radiant flux (Φ) per unit solid angle in a particular direction(θ,ϕ) (Mobley 1994), i.e.

$$I(\theta,\phi) = \frac{d\Phi(\theta,\phi)}{d\Omega} \quad [\text{J s}^{-1}\ \text{sr}^{-1} \text{ or W sr}^{-1}] \qquad \text{eq (2.28)}$$

where the solid angle element ($d\Omega$) is shown in Figure 2.4. The radiance, L, in a specified direction at a point in the radiation field is then defined as the radiant flux at that point per unit solid angle per unit area at right angles to the direction of photon propagation.

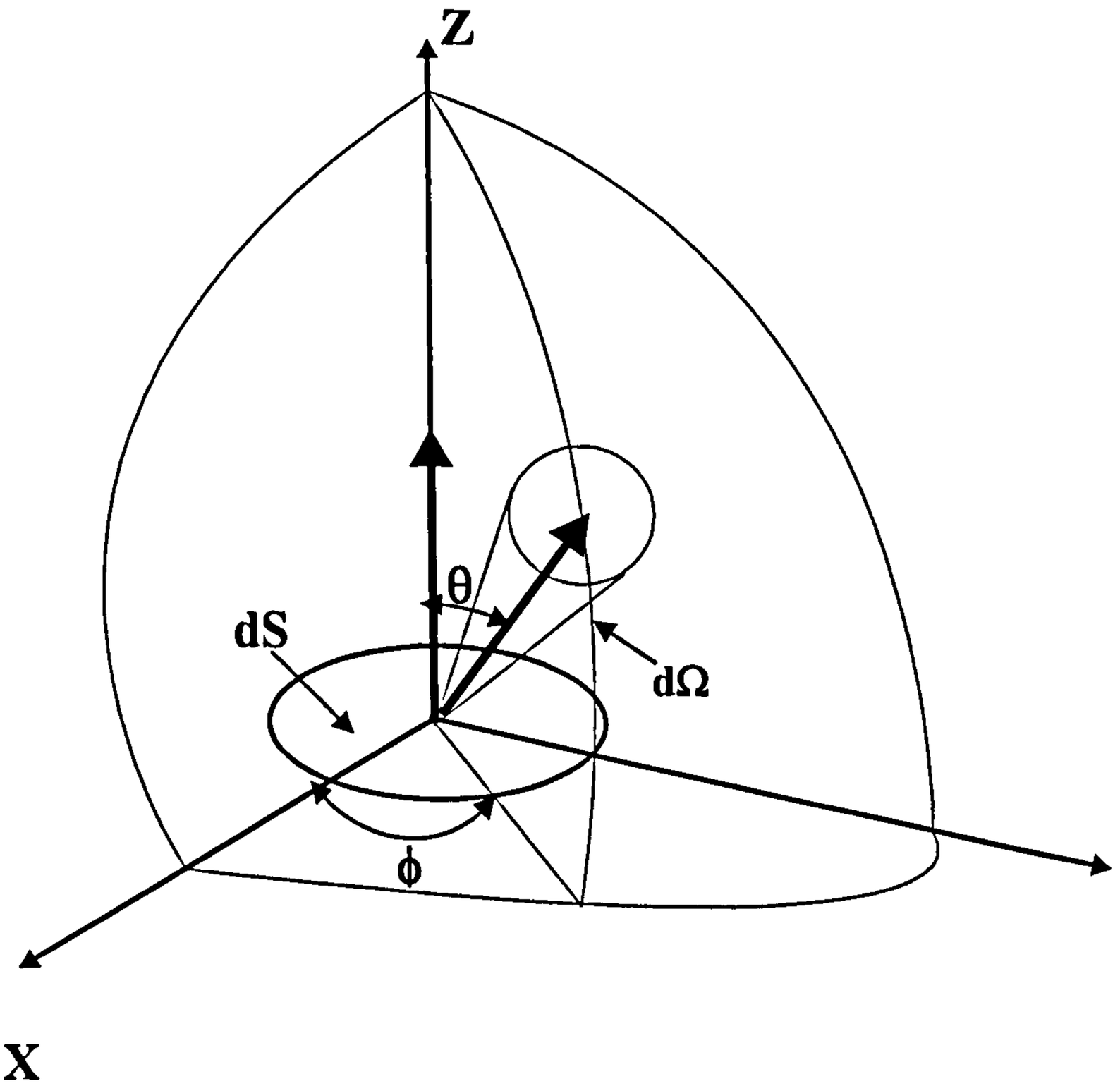

Figure 2.4 Illustration of the solid angle element $d\Omega$, the area dS and the angle θ

Thus, L describes the intensity per unit area in a plane normal to the direction of energy flow (Jerlov, 1968), i.e.

$$L(\theta,\phi) = \frac{d^2\Phi(\theta,\phi)}{dS\cos\theta\, d\Omega} \qquad [\mathrm{W\ m^{-2}\ sr^{-1}}] \qquad \text{eq (2.29)}$$

where the area dS and the angle θ are shown in figure 2.4 and dS cosθ is the projected surface area.

The term irradiance, E, refers to the radiant flux per unit area at a point within the radiative field or at a point on an extended surface. Irradiance is defined as the radiant flux impinging upon an infinitesimal surface area, dS, divided by that infinitesimal area (Kirk 1994).

$$E = \frac{d\Phi}{dS} \qquad [\mathrm{W\ m^{-2}}] \qquad \text{eq (2.30)}$$

If the radiant flux is constant on a surface, S, so we have

$$E = \frac{\Phi}{S} \qquad \text{eq (2.31)}$$

Radiance and irradiance are inter-related according to equation 2.32 (Mobley, 1994) and it considers the radiance impinging upon a point from θ and φ directions comprising the hemisphere immediately above the horizontal plane containing the point.

$$E = \int_0^{2\pi} \int_0^{\pi/2} L(\theta,\phi)\cos\theta \sin\theta \, d\theta \, d\phi \qquad \text{eq (2.32)}$$

The directional aspects attributable to radiance are not attributable to irradiance, since irradiance is comprised of all the radiant flux impinging on the selected point within the radiative field, i.e., all directions associated with the photon propagation.

Technically, however, irradiance can be treated as a directional parameter with upwelling and downwelling irradiances being considered as distinguishable entities in both atmospheric and aquatic optics.

Downwelling irradiance (E_d) is defined (Mobley, 1994) as the irradiance at a point due to the stream of downwelling light. E_d is obtained through integration over all downward directions, i.e.

$$E_d = \int_0^{2\pi} \int_0^{\frac{\pi}{2}} L(\theta,\phi)\cos\theta \sin\theta \, d\theta \, d\phi \qquad [\mathrm{W\ m^{-2}}] \qquad \text{eq (2.33)}$$

Upwelling irradiance (E_u) is defined as the irradiance at a point due to the stream of upwelling light (Mobley 1994).

$$E_u = -\int_0^{2\pi}\int_{\frac{\pi}{2}}^{\pi} L(\theta,\phi)\cos\theta\sin\theta\, d\theta\, d\phi \quad [\mathrm{W\,m^{-2}}] \qquad \text{eq (2.34)}$$

The negative sign on the right hand side of the above equation is to adjust for the fact that $\cos\theta$ is negative for $\pi/2 \leq \theta \leq \pi$.

At any point in the water column, the net downward irradiance, E_z is simply the difference between the downwelling and upwelling irradiances at that point, namely:

$$E_z = \int_0^{2\pi}\int_0^{\pi} L(\theta, \phi)\cos\theta\ \sin\theta\ \ d\theta d\phi = E_d - E_u \qquad \text{eq(2.35)}$$

Equation 2.35 integrates the product of each individual directional radiance $L(\theta,\phi)$ with the cosine of its corresponding polar angle (θ) over all the directions comprising of both the upper and lower hemispheres.

It is often appropriate to consider the total radiant intensity at a point in space, independent of its arrival directions. Such a consideration regards radiance from each direction equally. When such an equal treatment of radiances is considered in the integration, the resulting irradiance at that point is termed the scalar irradiance (E_0) and is defined as the integral of radiance distribution over all directions at that point. That is:

$$E_0 = \int_0^{2\pi}\int_0^{\pi} L(\theta, \phi)\sin\theta\ \ d\theta d\phi \qquad \text{eq (2.36)}$$

Equation (2.36) integrates $L(\theta,\phi)$ over all directions comprising the upper and lower hemispheres. Although each direction in the radiance distribution is treated equally, the directional nature of $L(\theta,\phi)$ is maintained. One can also define the downward scalar irradiance

$$E_{0d} = \int_0^{2\pi} \int_0^{\pi/2} L(\theta, \phi) \sin\theta \; d\theta d\phi \qquad \text{eq (2.37)}$$

and the upward scalar irradiance

$$E_{0u} = \int_0^{2\pi} \int_{\pi/2}^{\pi} L(\theta, \phi) \sin\theta \; d\theta d\phi \qquad \text{eq (2.38)}$$

Since the cosθ term is absent from the scalar irradiance expressions, no mathematical compensation is required to obtain E_{0u}. The terms downwelling light and upwelling light, usually, refer to downwelling and upwelling irradiance as opposed to downwelling and upwelling scalar irradiance fluxes. This thesis will adhere to the irradiance implication of these terms unless it is obvious from the context of the discussion that some other radiance distributions are being considered.

2.5.2 Inherent optical properties

Inherent optical properties (IOP) are those properties that depend only upon the medium, and therefore are independent of the ambient light field within the medium. Note that all quantities in this and the next section depend on wavelength.

2.5.2.1 Absorption, scattering and attenuation

Interactions such as absorption and scattering define the optical environment in a water body. The absorption, scattering and attenuation coefficients are useful quantities for describing the optical properties of water. They may be defined with the help of an imaginary, infinitesimally thin, plane parallel layer of medium, illuminated at right angles by a parallel beam of monochromatic light (Fig. 2.5). Some of the incident light is absorbed by the thin layer and some is scattered - that is, caused to diverge from its original path. The *absorptance* (A) is the fraction of incident power absorbed within the plane layer, i.e.

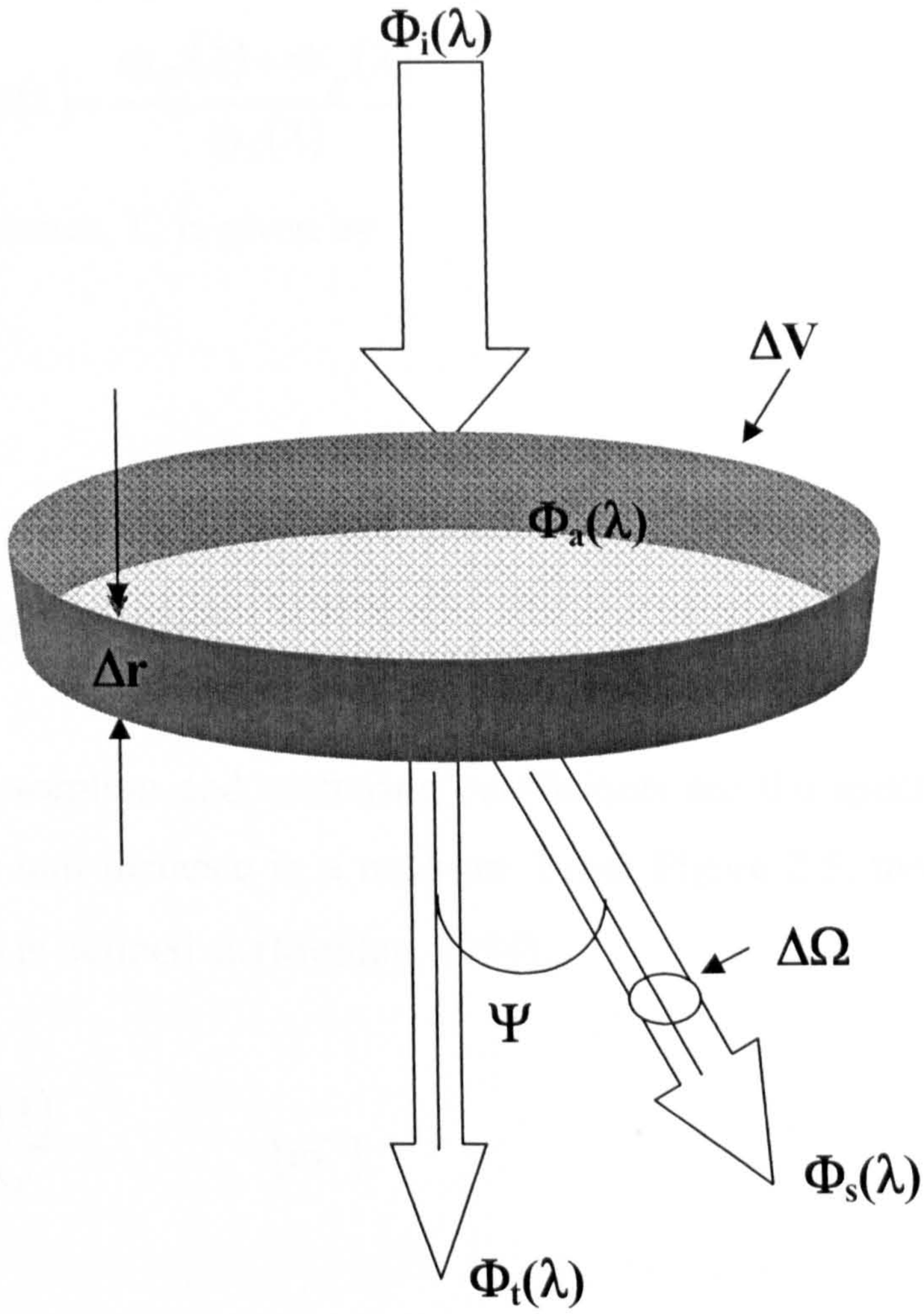

Figure 2.5: Light scattering from a thin layer

$$A(\lambda)=\frac{\Phi_a(\lambda)}{\Phi_i(\lambda)} \qquad \text{eq (2.39)}$$

where $\Phi_a(\lambda)$ is the absorbed radiant flux and $\Phi_i(\lambda)$ is the incident flux. Similarly the scatterance, $B(\lambda)$, is the fraction of the incident power that is scattered out of the beam inside the layer, i.e.

$$B(\lambda)=\frac{\Phi_s(\lambda)}{\Phi_i(\lambda)} \qquad \text{eq (2.40)}$$

where $\Phi_s(\lambda)$ is the scattered radiant flux.

The attenuance, C, is the sum of the absorptance and the scatterance, i.e.

$$C(\lambda)=A(\lambda)+B(\lambda)=\frac{\Phi_a(\lambda)+\Phi_s(\lambda)}{\Phi_i(\lambda)} \qquad \text{eq (2.41)}$$

and the transmittance, T, is given by

$$T(\lambda)=\frac{\Phi_t(\lambda)}{\Phi_i(\lambda)} \qquad \text{eq (2.42)}$$

Clearly, $A(\lambda)+B(\lambda)+T(\lambda)=1$

The spectral absorption and scattering coefficients are the spectral absorptance and scatterance per unit distance in a medium. From Figure 2.5, the spectral absorption coefficient $a(\lambda)$ is defined as (Mobley, 1994)

$$a(\lambda)=\lim_{\Delta r\to 0}\frac{A(\lambda)}{\Delta r} \qquad [m^{-1}] \qquad \text{eq (2.43)}$$

and the spectral scattering coefficient $b(\lambda)$ is defined as

$$b(\lambda)=\lim_{\Delta r\to 0}\frac{B(\lambda)}{\Delta r} \qquad [m^{-1}] \qquad \text{eq (2.44)}$$

The spectral beam attenuation coefficient is defined as

$$c(\lambda)=a(\lambda)+b(\lambda) \qquad [m^{-1}] \qquad \text{eq (2.45)}$$

As light travels through the medium, the flux decays following the relation (Beer's law)

$$\Phi(\lambda)=\Phi_i e^{-c(\lambda)z} \qquad \text{eq (2.46)}$$

The ratio $\varpi_0(\lambda)=\frac{b(\lambda)}{c(\lambda)}$ is called the spectral single-scattering albedo. This is also called the probability of photon survival.

2.5.2.2 Scattering functions

The way in which scattering affects the penetration of light into the medium depends not only on the value of the scattering coefficient, but also on the angular distributions of the scattered flux resulting from the primary scattering process. Taking into account the angular distribution of the scattered power, with $B(\Psi;\lambda)$ being the fraction of incident power scattered out of the beam through an angle Ψ into an solid angle $\Delta\Omega$ centred on Ψ (Figure 2.5). The angle Ψ is called the scattering angle; its value lies in the interval $0 \leq \psi \leq \pi$. Then the spectral volume scattering function is given as

$$\beta(\Psi;\lambda) = \lim_{\Delta V \to 0} \frac{I_s(\Psi;\lambda)}{E_i(\lambda)\Delta V} \quad [m^{-1}\ sr^{-1}] \qquad \text{eq (2.47)}$$

where, $I_s(\Psi;\lambda)$ is the spectral radiant intensity scattered into Ψ direction and $E_i(\lambda)$ is the incident irradiance on the surface.

Integrating $\beta(\Psi;\lambda)$ over all directions, we obtain the spectral scattering coefficient (Jerlov, 1968):

$$b(\lambda) = 2\pi \int_0^{\pi} \beta(\Psi;\lambda) \sin\Psi d\Psi \qquad \text{eq (2.48)}$$

The integration in the above equation 2.48 is often divided into forward scattering, $0 \leq \psi \leq \pi/2$ and backward scattering, $\pi/2 \leq \psi \leq \pi$ parts. The corresponding spectral forward and backward scattering coefficients are respectively,

$$b_f(\lambda) = 2\pi \int_0^{\pi/2} \beta(\Psi;\lambda) \sin\Psi d\Psi \qquad \text{eq (2.49a)}$$

$$b_b(\lambda) = 2\pi \int_0^{\pi} \beta(\Psi;\lambda) \sin\Psi d\Psi \qquad \text{eq (2.49b)}$$

The spectral volume scattering phase function, $\tilde{\beta}(\Psi;\lambda)$, is defined by (Mobley, 1994)

$$\tilde{\beta}(\Psi;\lambda) = \frac{\beta(\Psi;\lambda)}{b(\lambda)} \quad (sr^{-1}) \qquad \text{eq (2.50)}$$

Combining equations 2.48 and 2.50 gives the normalization condition for the phase function:

$$2\pi \int_0^{\pi} \beta(\Psi;\lambda)\sin\Psi d\Psi = 1 \qquad \text{eq (2.51)}$$

The average over all scattering directions of the cosine of the scattering angle ψ,

$$g = 2\pi \int_0^{\pi} \tilde{\beta}(\Psi;\lambda)\cos\Psi \sin\Psi \, d\Psi \qquad \text{eq (2.52)}$$

is a convenient measure of the shape of the phase function.

2.5.2.3 Bulk and specific inherent optical properties

Bulk inherent optical properties are those optical properties displayed when the water column is considered as a composite entity with no regard as to the specific component contributions to that property. Thus the bulk values are consequences of the totality of that particular optical property contributed by individual components in the medium. Specific inherent optical properties are those optical properties that can be attributed to the individual optical property centres comprising the aquatic medium under consideration. It is these specific inherent optical properties that must be determined if a water body is to be remotely sensed for estimates of the concentrations of its individual components.

The bulk inherent optical properties of a natural water column, such as $a(\lambda)$, $b(\lambda)$ and $b_b(\lambda)$ can be considered as the additive consequence of the individual specific inherent optical properties of different optically active components present in the water column (Bukata, 1995). That is

$$a(\lambda) = \sum_{i=1}^{n} x_i a_i(\lambda) \qquad [\mathrm{m}^{-1}] \qquad \text{eq (2.53)}$$

$$b(\lambda) = \sum_{i=1}^{n} x_i b_i(\lambda) \qquad [\mathrm{m}^{-1}] \qquad \text{eq (2.54)}$$

$$b_b(\lambda) = \sum_{i=1}^{n} x_i b_{bi}(\lambda) \qquad [\mathrm{m}^{-1}] \qquad \text{eq (2.55)}$$

$a_i(\lambda)$, $b_i(\lambda)$ and $b_{bi}(\lambda)$ represent the amount of absorption, scattering, and backscattering that maybe attributed to a unit concentration of a particular component of a water column.

2.5.3 Apparent optical properties

In contrast to the inherent optical properties described in Section 2.5.2, the apparent optical properties (AOP) depend both on the medium and on the directional structure of the ambient light field. Ratios of radiometric quantities and the rate of change with depth of a radiometric quantity are often insensitive to environmental changes. It is these ratios and depth derivatives that are considered most as AOP. Measurement of AOP are easy to make and therefore they form a major source of information about optical properties of natural waters.

2.5.3.1 Average cosines

One apparent optical property is the downwelling average cosine defined by (Mobley,1994)

$$\bar{\mu}_d(z;\lambda) = \frac{\int_0^{2\pi}\int_0^{\pi/2} L(z;\theta,\phi;\lambda)\cos\theta\sin\theta\, d\theta d\phi}{\int_0^{2\pi}\int_0^{\pi/2} L(z;\theta,\phi;\lambda)\sin\theta\, d\theta d\phi} = \frac{E_d(z;\lambda)}{E_{0d}(z;\lambda)} \qquad \text{eq (2.56)}$$

and another one is the upwelling average cosine given by

$$\bar{\mu}_u(z;\lambda) = \frac{E_u(z;\lambda)}{E_{0u}(z;\lambda)} \qquad \text{eq (2.57)}$$

These are measures of the directional structures of the downwelling and upwelling light fields. The average cosine can also be defined for the net downward irradiance

$$\bar{\mu}\,(z;\lambda) = \frac{E_d(z;\lambda) - E_u(z;\lambda)}{E_0(z;\lambda)} \qquad \text{eq (2.58)}$$

The quantities E_d, E_{0d}, E_u, E_{0u} and E_0 are defined in earlier sections

2.5.3.2 Reflectance

Irradiance reflectance is an apparent optical property, which is defined as the ratio of upwelling irradiance to the downwelling irradiance at a point. Within a water body this ratio is known as the subsurface volume reflectance, or simply the volume reflectance (Kirk 1994).

$$R(z,\lambda)=\frac{E_u(z,\lambda)}{E_d(z,\lambda)} \qquad \text{eq (2.59)}$$

The volume reflectance, R, is one of the singularly most important parameters in the interpretation of spectral data in terms of the compositions of natural water bodies.

In remote sensing applications another important optical property is the remote sensing reflectance, which is a ratio of water leaving radiance (Lw) to the downwelling irradiance (Ed) just above the surface

$$Rrs(\theta,\phi,\lambda)=\frac{L_w(0+;\theta,\phi;\lambda)}{E_d(0+,\lambda)} \quad [sr^{-1}] \qquad \text{eq (2.60)}$$

The sign 0+ indicates that the measurements are just above the water surface and are made in a direction (θ,ϕ).

2.5.3.3 Diffuse attenuation coefficients

The irradiance attenuation coefficient or the diffuse attenuation coefficient, $K(z,\lambda)$, is defined as the logarithmic depth derivative of the spectral irradiance at subsurface depth z (Kirk, 1994).

$$K_d(z,\lambda)=-\frac{d\ln E_d(z,\lambda)}{dz} \qquad \text{eq (2.61)}$$

The spectral diffuse attenuation coefficient for spectral downwelling plane irradiance $K_d(z,\lambda)$, in the equation (2.61) results from Beer's Law being used to describe the attenuation of spectral irradiance with depth z. That is:

$$E(z,\lambda) = E(0-,\lambda)\exp[-K(z,\lambda)*z] \qquad \text{eq (2.62)}$$

where $E(z,\lambda)$ and $E(0-,\lambda)$ are the values of the irradiance depth z and just below the air-water interface, respectively. Other diffuse attenuation coefficients, e.g. K_u, K_{0d}, K_{0u} and $K(\theta,\phi)$ are defined by equations analogous to Eqs 2.61 and 2.62.

2.5.4 Relation between apparent and inherent optical properties

A number of approximate relations among various inherent optical properties and apparent optical properties have been developed over years. These relations often are based on arguments drawn from radiative transfer theory combined with analysis of actual data. Most of these relations are developed for homogeneous open-ocean (case 1) waters.

The irradiance reflectance, R(0), just below the sea surface can be reasoned to be directly proportional to the backscattering coefficient b_b, and inversely proportional to the absorption coefficient a. This can be written as (Morel and Prieur, 1977),

$$R(0) = \alpha\frac{b_b}{a} \qquad \text{eq (2.63)}$$

where the proportionality constant α depends on the radiance distribution, i.e. the solar zenith angle, diffuse skylighting, sea state and shape of scattering phase function. From the studies of Gordon *et al.* (1975) and Morel and Prieur (1977) an approximate value of 0.33 for α was estimated

$$\Rightarrow R(0) \approx 0.33\frac{b_b}{a} \qquad \text{eq (2.64)}$$

Kirk (1974) numerically studied the dependency of α on solar angle and found

$$R(0) \approx (0.975 - 0.629\mu_{sw})\frac{b_b}{a} \qquad \text{eq (2.65)}$$

where μ_{sw} is the cosine of the nadir angle of the solar beam after refraction through a level sea surface.

More recent numerical simulations by Morel and Gentili(1991) lead to

$$R(0) \approx \begin{bmatrix} (0.6279 - 0.2227\eta_b - 0.0513{\eta_b}^2) \\ +(-0.3119 + 0.2465\eta_b)\mu_s \end{bmatrix}\frac{b_b}{a} \qquad \text{eq (2.66)}$$

Here ηb is the ratio of backscattering by water molecules to total backscattering and $\mu_s = \cos\theta_s$.

Another such relation can be rewritten from Gershun's law (Mobley 1994), which connects $\bar{\mu}$, s, K and R to the absorption coefficient a.

$$\bar{\mu} = \frac{a(1-R)}{K_d - RK_u} \qquad \text{eq (2.67)}$$

One of the oldest such approximation is (Mobley 1994)

$$K_d \approx a + \frac{b}{6} = c - \frac{5}{6}b \qquad [m^{-1}] \qquad \text{eq (2.68)}$$

This formula can be in error by 30% or more, especially near the sea surface.
Numerical simulation by Kirk(1984) gives

$$\bar{K}_d = \frac{a}{\mu_{sw}}\left[1 + (0.425\mu_{sw} - 0.19)\frac{b}{a}\right]^{\frac{1}{2}} \qquad \text{eq (2.69)}$$

where $\bar{K}_d$ is the average of $K_d(z)$ over the euphotic zone and μsw is the cosine of the refracted solar angle. Extending the analysis to other volume scattering functions gives (Kirk 1991) as given in equation 2.70.

$$\bar{K}_d = \frac{a}{\mu_{sw}}\left[1 + G(\mu_{sw}, g)\frac{b}{a}\right]^{\frac{1}{2}} \qquad \text{eq (2.70)}$$

Here g is the mean cosine of the scattering angleψ. The function $G(\mu_{sw},g)$ parameterises the influence of the shape of the scattering function on K_d .

Approximate relations presented in this section are simple enough to be convenient and accurate enough to be useful, at least in homogeneous, oceanic waters. Such formulae are just approximations and the reality can be more complicated than these equations imply.

2.3 Photon or wave?

It is clear from previous sections (2.2.1 and 2.2.2) that there exist two options to explain the light-matter interactions. Until some scientific evidence is presented applications scientists have the privilege of using both the explanations. Photon theory is useful in explaining energy absorption by matter, photo chemical reactions and energy emissions. Mie computations based on electromagnetic wave explanations are popular in predicting particulate efficiencies. This research takes advantage of this situation and employs both the theories as tools to achieve the research objectives to simulate and explain the optical signature in coastal waters.

Chapter 3 : Biogeooptics of coastal waters

3.1 Background

The coastal zone is an interface between the land and the ocean that filters, controls and thus influences the contributions from land to ocean. It is important to monitor the flux of biogeochemical components passing through this region, to have an understanding of the consequent processes in the ocean. The biogeochemical constituents can greatly influence the optical environment of the coastal waters as they move (transit) through a region. Fluctuations thus induced in the optical environment can influence the marine ecology in this coastal environment (Blough and Vecchio 2002). These reasons highlight the importance of monitoring the biogeochemistry in coastal waters.

As most biogeochemical components are optically active, they are capable of projecting signatures that can influence the colour of the water. The focus of optical investigations is to monitor optically active biogeochemical constituents along with other constituents, which are markers of optically inactive but important inputs in biogeochemical mechanisms. By taking advantage of optical and remote sensing techniques, one can monitor these critical optical processes in greater detail. So, this chapter looks into the different optically active biogeochemical components that may be present in coastal waters, their role in this environment and their influence on the optical environment.

3.2 Biogeochemistry and optical behaviour

The *in-water* constituents behaviour in coastal waters are mostly non-conservative in nature, as they are influenced both by the ocean and inputs from land. River discharges, anthropogenic activity and atmospheric deposition coupled with evaporation, dissolution and oxidation can induce alterations both in the flux and composition of the constituent material. Suspended material, phytoplankton and chromomorphic dissolved organic material (CDOM) are the major optically active components that participate in coastal processes. These components can individually influence the biogeochemical mechanisms of a region. In the following sections each

of these components are studied more closely to understand their role in the coastal environment.

3.2.1 Chromophoric dissolved organic material

Dissolved organic matter is recognised as having an important role in the biogeochemical cycles of coastal waters. Man-made chlorofluorocarbons have caused destruction of the stratospheric ozone in the polar regions, leading to increased levels of surface ultraviolet radiation. This enhanced exposure to ultraviolet (uv) radiation has exerted high levels of stress on carbon and mineral nutrient cycles in the aquatic ecosystems and on the exchange of radiatively and chemically important gasses between the hydrosphere and atmosphere (Zepp *et al.,* 1998). The ultraviolet induced photo-transients of dissolved organic material produce photochemical degradation of materials (Helz *et al.,* 1994). Such impacts are realised both in freshwater and marine ecosystems (Blough and Zepp, 1990; Williamson *et al.,* 1996; Häder *et al.,* 1998; Zepp *et al.,* 1998; Neale and Kieber, 2000).

Owing to an approximately exponential increase of absorption with decreasing wavelength, CDOM absorbs light strongly in the ultraviolet region and is usually the principal constituent within aquatic systems that controls the penetration depth of radiation potentially harmful to organisms. Thus the amount of CDOM in the surface waters can have a substantial impact on the levels of damaging radiation received by aquatic organisms. In coastal waters, light absorption by CDOM can extend well into the visible region often dominating the absorption by phytoplankton in the blue portion of the visible spectrum. In such environments the availability of photosynthetically available radiation (PAR) is greatly controlled by the presence of CDOM in the surface, thus decreasing the primary productivity and affecting ecosystem structure. CDOM can therefore play a substantial role in the biogeochemistry of natural waters merely through its influence on the aquatic light field (Blough *et al.,* 1993; Arrigo and Brown, 1996; Vodacek *et al.,* 1995, 1997; Williamson *et al.,* 1996; Conde *et al.,* 2000).

Absorption of light by chromophoric dissolved organic material also initiates the formation of a variety of photochemical intermediates and products (Blough and

Zepp, 1995; Blough 1997; Moran and Zepp, 1997; Moran *et al.*, 2000; Blough 2001; Mopper and Keiber, 2002). The photochemical reactions producing these species ultimately lead to the destruction of the CDOM and the loss or bleaching of its absorption and fluorescence (Kouassi and Zika, 1990; Kouassi *et al.*,1992; Moran *et al.*, 2000; Twardowski and Donaghay, 2001). These processes can thus feedback to alter the aquatic optical environment, potentially allowing greater penetration of damaging UV radiation. Light absorption by CDOM can have a number of additional consequences such as photooxidative degradation of organic matter, direct photochemistry altering the biological availability of some metals, photochemical production of trace gases of importance in atmosphere, such as CO_2, CO and COS, and the destruction of others such as dimethyl sulphide and the photochemical production of biologically available low-molecular-weight organic compounds and the release of available forms of nitrogen, thereby fuelling the growth of micro organisms from a biologically resistant source material, CDOM.

3.2.1.1 Origin and composition of CDOM

Dissolved organic matter concentrations in natural waters are consequences of either photosynthetic activity of phytoplankton (autochthonic) or direct inputs of terrestrially derived matter (allochthonic). The transformation of phytoplankton to dissolved organic material is a consequence of photolysis, hydrolysis and bacterial decomposition of the phytoplanktonic cellular structures. Of the total organic matter resulting from phytoplankton photosynthesis, up to 20% can be released to the aquatic environment through metabolic egestion (Bukata *et al.*, 1995). When phytoplankton cells decompose in the water column, the organic matter is chemically transformed, through microbial action on the time-scales of days to weeks, to carbon dioxide and inorganic nitrogen, sulphur, and phosphorous compounds. In addition, the decomposition process results in the creation of a variety of complex polymers generally referred to as humic substances. Other than phytoplanktonic decay, in marine waters, brown seaweeds actively excrete phenolic compounds that probably as a consequence of oxidation and polymerization, give raise to yellow-brown materials of a humic type within the water (Sieburth and Jensen, 1969).

It is likely that most of the dissolved organic material of terrestrial origin is due to soluble humic substances leached from the soils in the catchment areas, and thus indirectly from the vegetation. Organic material of humic type can also be generated by decomposition of plant matter within the water. Much of the soluble humic material in river water is precipitated when it comes into contact with sea water. Nevertheless, a fraction of the material remains in solution and most of the dissolved yellow colour in coastal sea water is due to humic substances derived from the land in river discharge (Kirk, 1994).

Degradation and other studies indicate that humic substances, the source material of CDOM, are polymers consisting of aromatic rings which are joined by long-chain alkyl structures. Humic substances vary in size from freely soluble compounds with molecular weights of a few hundred, to insoluble macromolecular aggregates with molecular weights which may extend up to millions. The precise chemical composition of these dissolved substances is difficult to ascertain (Spitzy & Ittekkot 1986, Findlay & Sinsabaugh 1999). Humic substances may be further categorized into humin, humic and fulvic acids and the later two are the major components of CDOM. In fact all three fractions are chemically very similar and differ mainly in molecular weight, humic acid molecules being larger than those of fulvic acid. They are yellow to brown in colour, hydrophilic and acidic. Fulvic acid has a higher content of oxygen containing groups such as carboxyl and hydroxyl.

While some humic material is formed by the oxidation and polymerization, directly from the existing phenolic compounds in the decomposing plant tissue, in other cases the formation may be related to the large amounts of excretion of phenolic substances by saprophytic fungi and the subsequent oxidation and polymerization that results in the generation of humic-like material. It is recognised that some of the aromatic subunits of the humic materials originate in the plant and some are generated de novo during microbial breakdown. The proportion of aromatic carbon in marine humic and fulvic acids is lower than the corresponding fresh-water substances. Marine fulvic acid appears only to contain a small proportion of aromatic residues and is predominantly aliphatic in nature (Kirk, 1994). The fulvic and humic acids in sea water may contain mainly of polymeric compounds formed by the oxidative crosslinking of polyunsaturated lipids derived from biota.

3.2.1.2 Optical behaviour of CDOM

The yellow colour of CDOM is a consequence of the temperature-dependent Maillard reaction involving amino acids, carbonates, and phenol-bearing matter (humic substances). In the presence of an alkaline medium the Maillard reaction leads to the formation of yellow and brown melanoids that are polymers (Bukata *et al.*, 1995). The presence of multiple double bonds, many of them conjugated, some in aromatic nuclei will result in the yellow hue associated with this substance. As a consequence of this yellow hue, the dissolved aquatic humus is generally referred to as yellow substance. In any sample of humic material there are numerous different chromophores, and consequently a multitude of electronic excitation levels which, because they overlap, give raise to a rather undifferentiated ultraviolet and visible absorption spectrum.

Absorption and fluorescence are the most significant optical properties of CDOM in natural waters. As well as absorbing light, dissolved humic material in natural waters also has a broad fluorescence emission band in the blue region. Fluorescence measurements of humic substances and CDOM have generally been more common than absorption measurements, due primarily to their greater sensitivity and simplicity (Donard *et al.*, 1989; Chen and Bada, 1992; Green and Blough, 1994; De Souza Sierra *et al.*, 1994, 1997). Fluorescence is far more amenable to continuous monitoring (Vodaceck *et al.*, 1995) and remote measurement (Hoge *et al.*, 1995; Vodacek *et al.*, 1995), and thus potentially allows for high resolution mapping of CDOM distributions. However, fluorescence provides only an indirect measure of CDOM absorption, and its magnitude and spectral dependence are more sensitive to factors such as pH, ionic strength and the presence of quenchers. Also steady-state fluorescence is not representative of the entire population of absorbing species within CDOM, nor of the entire population of emitting species; instead fluorescence spectra will tend to be dominated by those subpopulations exhibiting longer fluorescence lifetimes (Herbelin, 1994; Blough and Green, 1995; Lakovicz, 1983).

Absorption by CDOM is one of the factors determining the shape of the total absorption spectrum in the visible region, and thus influencing the colour of natural waters. Absorption spectra of CDOM varies markedly not only between marine and fresh waters, but also depending on the spatio-temporal situations. For example, its

concentration in coastal waters changes, with time, in accordance with rainfall events in different parts of the catchment and consequent changes in the concentration of CDOM in the inflowing waters.

The light absorption properties of dissolved aquatic humus have been studied intensively (Bricaud *et al.*, 1981; Carder *et al.*, 1989; Højerslev, 1988). Results from these studies show that, as a consequence of electronic transitions, absorption by dissolved organic matter dramatically decreases with increasing wavelength. The absorption coefficient at 440 nm can be used as a convenient parameter to indicate the concentration of CDOM. This wavelength is suitable because it corresponds approximately to the midpoint of the blue waveband peak that most classes of algae have in their photosynthesis action spectrum.

3.2.2 Suspended particulate material

Suspended particulate materials (SPM) comprises of sediments and seston that are suspended in the water column either permanently or, more usually for sediments, temporarily and in a state of exchange with the bed sediment reservoir. These suspended particles are instrumental in controlling the reactivity, transport, underwater optical environment and biological impacts of substances in aquatic environments and provide a crucial link for chemical constituents between the water column, bed sediment and food chain. In shallow coastal water bodies, wave and current action bring sediments into suspension, modifying significantly the colour of the ocean. In this section, a detailed review of the suspended particulate material origin, composition and optical behaviour is presented.

3.2.2.1 Origin and composition of suspended particulate material

Coastal suspended particles are basically derived from river discharge, continental shore erosion, *in situ* chemical and biological processes and from long and short range transport of atmospheric particulates. These particulates are diverse in composition, shape and size. Depending on the origin, particles can be classified into lithogenic, hydrogenic, biogenic and anthropogenic. It is also appropriate to discriminate these particles as sestonic and non-sestonic particles according to their characteristics. A classification of the later type is suitable in optical remote sensing investigations.

Classification by origin describes lithogenic material as that inorganic component which is derived from the weathering of crustal material and is mainly composed of quartz and other primary silicate materials such as feldspar, and secondary silicate minerals (clays). A hydrogenous component of SPM is generated *in situ* by chemical processes, and exists either as coatings on lithogenous material, or as discrete phases. Hydrogenous phases include iron and manganese oxides, carbonates, sulphides and humic aggregates. The biogenic component is generated *in situ* or externally by biological processes, and includes micro-organisms, plankton, decaying remains of organisms, faecal matter and marine and terrestrial plat debris. Anthropogenic components include sewage solids, plastics, mine tailings, coal dust and fly ash and may occur as discrete particles, or as non-aqueous phase liquids entrapped within the particle matrix (Luthy *et al.,* 1997).

Seston refers to discrete biogenic entities formed *in situ* including plankton, bacteria, invertebrate larvae and eggs, and assemblages thereof, and provides the main source of nutrition for suspension feeders. These particles may be weakly motile and have densities similar to that of water. Their abundance and distribution are largely determined by the factors that control the primary productivity and therefore have a strong seasonal component. Non-sestonic particles are a complex assemblage of mineral and biogenic materials and more exactly, can be described as suspended sediments.

The general structure of a typical coastal suspended particle is more complex than explained in the above paragraphs. Along with planktonic, humic solids and mineral

particulate material, an equally common material found in natural waters is a modified particulate mineral. These modified particulate materials basically consist of a relatively inert core comprising of primary and secondary silicates, surrounded by a more reactive coating, comprising of iron and manganese oxides, carbonates, sulphides, detrital organic matter and micro organisms (Wang *et al.* 1997). In reality, sediment composition is far more complex than this since many mineral components are porous or fractured and are heterogeneously dispersed within the assemblage or as a floc (Gustafsson & Gschwend, 1997, Droppo 2001).

[a] Suspended mineral particulate material

Suspended mineral particulate material in coastal waters, generally, is a consequence of river discharge or seabed resuspension. These are basically an assemblage of particles of different types, which reflects the rock types and weathering conditions in the source areas. Mineral particles found in suspension are those that are resistant to weathering. Quartz, feldspars, and calcite are residues, leftover after dissolution and rock break-up. Quartz is more resistant than feldspars, and potassium feldspars are more resistant than sodium feldspars. Clay minerals are weathering products of feldspars and other minerals present in rocks and soils. Mica is also a component of many igneous rock types. Kaolinite and chlorite are predominant aluminosilicates from higher latitudes. Illites and micas are the most common clay minerals and occur in a wide variety of environments; they dominate where kaolinites and chlorites are present in minor quantities. Montmorillonites are formed in wet soils at medium or low temperatures by direct weathering of rock, or by transformation of illites or chlorites. In sub marine volcanic areas montmorillonites are the most common clay mineral (Esima, 1993)

The supply and distribution of recently formed clay minerals is often mixed with a supply from erosion of older fine-grained deposits and sedimentary rocks, which have been formed under conditions that differ from those at present in that area. Many drainage areas extend over different weathering zones, which are reflected in the mineral composition of the suspended particulate matter.

Mineral particles in suspension have a limited size range. For example, Figure 3.1 (from Gibbs 1977) shows the size distributions of the principal minerals present in material transported from the Amazon into coastal waters. Feldspars are the largest and clay minerals the smallest minerals. Usually silts are mainly quartz, feldspars and micas. As suspended matter is usually flocculated, a range of grain sizes is present in flocs and the flocs themselves are mineral assemblage. There is also another component, not indicated in the figure, which contributes to this size distribution; it is the poorly crystallized and amorphous mineral material. Its amount is very much under estimated in most mineralogical analyses and its contribution is not clear. According to Adamenko *et al.*(1991) fine clay particles rarely exceed 3-4 μm in diameter, silt particles are in the range 5-40 μm, very fine grain sands are in the range 40-130 μm, and coarser grain sands are in the range 130-250 μm. From the above examples one may generalise that, quartz and aluminosilicates (with a limited size range) usually form the major part of the suspended mineral particulate material.

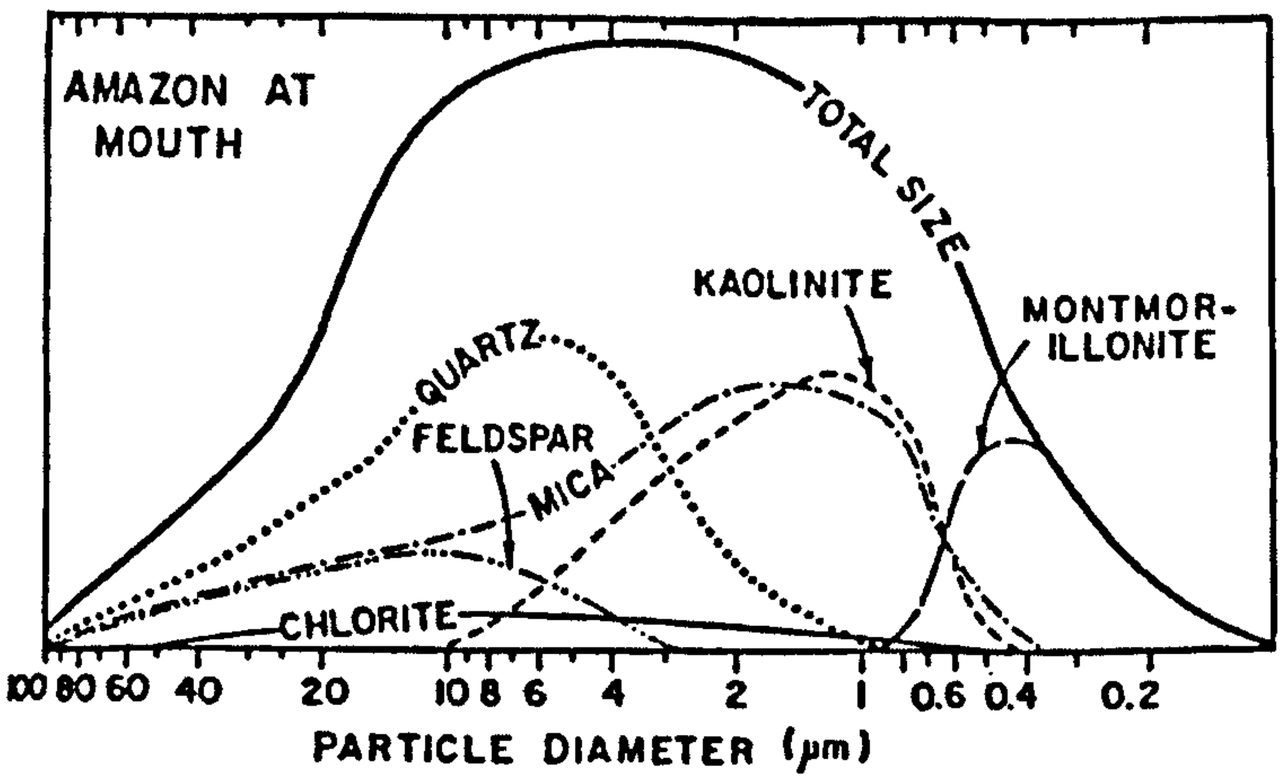

Figure 3.1: The size distribution of mineral phases transported by Amazon River (Gibbs 1977).

[b] Organic suspended particulate material

Naturally suspended organic particulate material is restricted to plankton and detritus, with plankton comprising of zooplankton, algae, bacteria and algal fungi. Detritus is composed of decayed plants and animals along with their excretions.

Zooplankton, being grazers of algae, detritus and bacteria are an integral component of the trophic status of natural waters and, as such, are in dynamic equilibrium with the other components of the aquatic food chain. Depending upon the trophic status of the coastal waters, the concentrations of zooplankton can be significant, varying in sizes from 30 μm to 2 mm. The spatial distribution of zooplankton is controlled by current patterns, thermal structure, reproductive cycles, the presence and concentrations of nutrients and the presence and populations of planktivores. This multi-dependency brings out a patchy segmentation in their population distribution, which becomes more pronounced, due to nutrient limitation, as the trophic status of the water diminishes. Zooplankton are generally considered to be ineffectual aquatic colorants, and consequently noted as insignificant contributors. This ineffectiveness is a result of their small concentrations when compared to many orders of magnitude higher concentrations of phytoplankton. Further, one can still include its contribution, by using chlorophyll concentrations, as zooplankton are grazers of phytoplankton and phytoplankton are chlorophyll-bearing biota.

Phytoplankton are free-floating microscopic plants, which are the principal primary producers of the world's oceans. These unicellular, filamentous or chain-forming species encompass a wide diversity of photosynthetic organisms. The principal taxonomic groups include diatoms, dinoflagellates, coccolithophores and silicoflagellates. In coastal and inland waters, other taxonomic groups may locally predominate, such as euglenoid flagellates, green algae, blue - green algae, and brown – coloured phytoflagellates. Phytoplankton are subdivided into four major size classes: nanoplankton (2-20 μm); microplankton (20 – 200 μm); mesoplankton (0.2-20 mm); and macroplankton (>2 cm). Most phytoplankton assemblages consist of nanoplankton (mainly diatoms, coccolithophores and silicoflagellates) and microplankton (diatoms and dinoflagellates).

The other organic particulate component, which co-exists along with planktonic material, is the humic solid substance or particulate humic substance. These humic solids are basically derived from terrestrial inputs. It contains readily detectable lingo cellulose components that have been used as indicators of the terrestrial contribution to marine organic matter. Along with the water soluble portion the particulate decayed organic plant matter find their way into streams, rivers and the coastal ocean. Their presence in coastal waters can therefore be associated with the rainfall and stream runoff. After entering the coastal water domain, they play a significant role in local biogeochemical cycles. Along with CDOM these humic solids participate in aquatic photodegradation and photochemical activity resulting in mineralization of dissolved organic carbon and trace gas exchange (Zepp *et al.,* 1998). Not much research has been done on their size and composition characteristics. It is also the complexity of their assemblage associations that make them difficult to study. These humic solids generally form complex matrices with mineral particulate assemblages thus posing difficulties in size estimation.

3.2.2.2 Optical properties of suspended particulate material

[a] Absorption by phytoplanktonic particulate material

Absorption of photon energy is the first step towards photosynthesis in phytoplankton bioactivity. The energy absorbed is transferred to special structures, called reaction centres, where the energy is used in electrical charge separation. The absorbed photon can only influence one molecule. The portion of the molecule that absorbs the light is called a *chromophore*, and four basic types of chromophores exist, namely, open tetrapyroles (found in the phycobillipigments), closed tetrapyroles and their derivatives consisting of porphyrins (e.g., chlorophyll c) and chlorines (e.g., chlorophylls a and b) and the carotenoids (e.g., zeaxanthin, fucoxanthin, β-carotene). All four types of molecules are characterized by extensive π bond systems and are all visibly coloured (Falkowski & Raven 1997).

A classification can be made based on the photosynthesising agents: chlorophylls, carotenoids and phycobilins. Chlorophylls and carotenoids are present in all algal species. Phycobilins are additionally present in blue-green algae and dinoflagellates (Bukata *et al.*, 1995). The structure of all chlorophylls and porphyrins is based on chemical condensation of a repeating element, namely the non essential amino acid, δ-aminolevulinic acid (ALA). Two molecules of ALA condense to form porphobilinogen, which is a pyrrole containing two atoms of nitrogen. The condensation of four pyrroles can lead to the formation of an open molecule with extensive conjugate double bond systems. Such linear tetrapyroles are the chromophores found in phycobillisomes of cyanobacteria and rhodophytes. Tetrapyrroles can also condense to form a closed ring system. Two basic types of closed rings are found: chlorines and porphyrins. In chlorophylls, the nitrogen atoms in the rings are coordinated to a Magnesium atom (Figure 3.2).

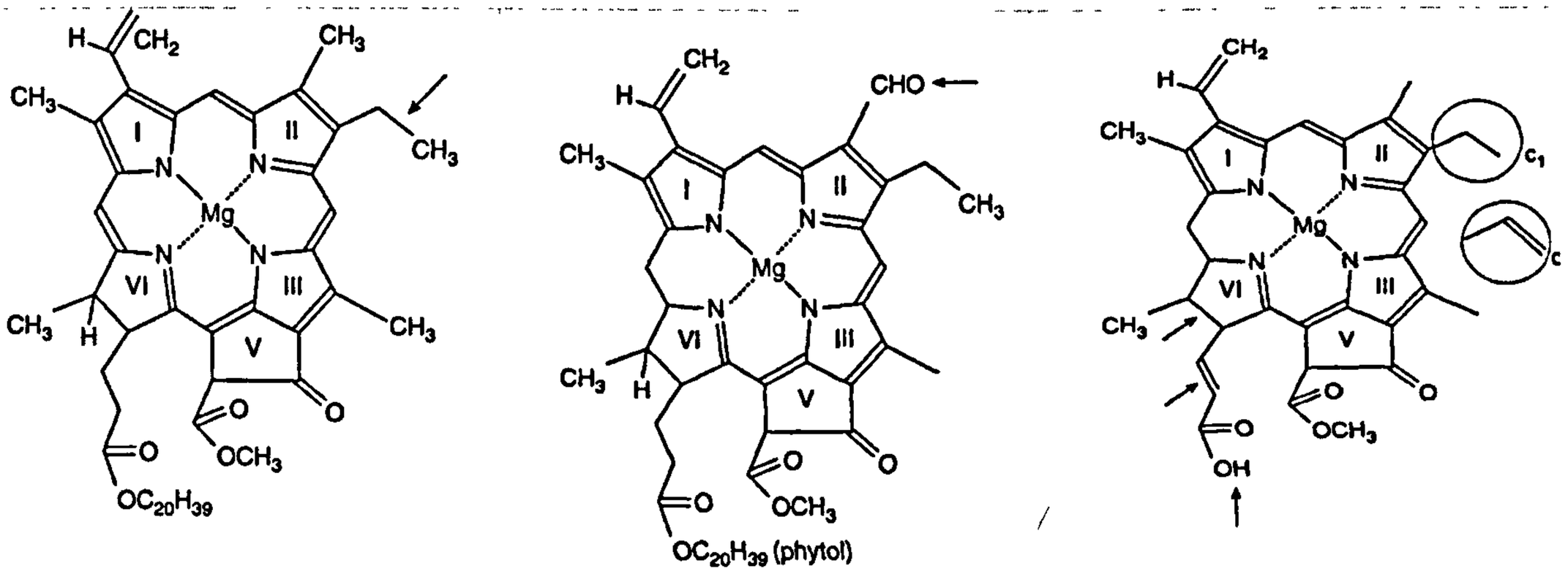

Figure 3.2: Structures of Chlorophylls a, b and c (left to right). All chlorophylls are made of four pyrroles which are nitrogen-containing five-member rings (Falkowski & Raven 1997).

Carotenoids are pigments that participate in photon harvesting. Even though there are considerably more known carotenoids than known chlorophylls, the predominant carotenoid present in aquatic algae is β-carotene. The molar ratio of carotenoids to chlorophylls maybe less than or greater than unity, and varies among plankton species (e.g., 1: 3 for green algae; 2:1 for diatoms; 3:2 for dinoflagellates; 1:2 -2:1 for brown algae; 1:1 – 2:5 for red algae) (Bukata, 1995). Together with chlorophylls and phycobilins, the carotenoids account for the phytoplankton contribution to water colour.

All chlorophylls have two major absorption bands: blue or blue-green absorption bands, often called the B bands or Soret bands and the red absorption bands called the Q bands. The Soret absorption bands reflect the population of three higher energy singlet states, which rapidly decay to the lowest singlet excited state represented by red absorption band (Figure 3.3). The Soret (blue) absorption bands reflect the population of the three higher energy singlet states, which rapidly decay to the lowest singlet excited state represented by the red absorption band. The major red absorption band in both chlorophylls a and b is a consequence of a redistribution of the electrons associated with the π-π^* transition on the ring 4, oblique to the y-axis of the molecule. Hence the name of the resulting spectral bands, Q_y (Falkowski and Raven, 1997).

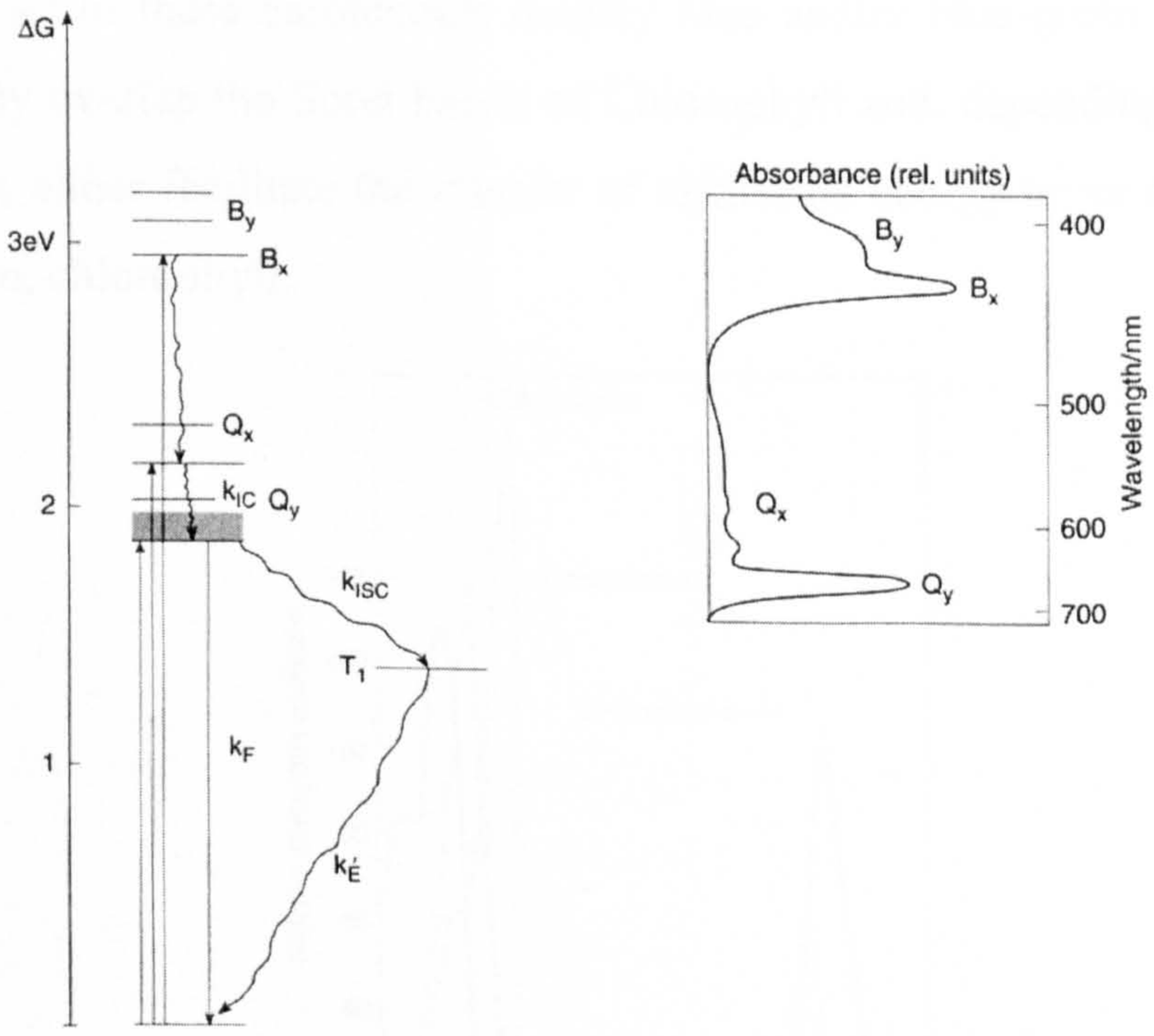

Figure 3.3: Schematic energy level diagram showing the relationships between excited states, absorption bands and fluorescence in chlorophyll a (Falkowski & Raven 1997).

All photochemical reactions in photosynthesis proceed from the de-excitation of the Q_y transition to the ground state. Thus, regardless of the energy of the absorbed photon, absorbed energy must be converted to the lowest singlet excited state (Butler, Katajima 1975). This is achieved by dissipating the extra energy in the form of heat. In chlorophyll *b* the methyl ring on ring 2 is replaced with a formyl group (CHO). This structural modification leads to the absorption of longer wavelengths ('red

shifted') in the Soret region relative to chlorophyll a but a shorter wavelength absorption ('blue shifted') in the red region. Chlorophyll *c*'s are found in diatoms and dinoflagellates and it has a fifth ring attached to ring 3 (Figure 3.2). This modification breaks the symmetry and consequently has a weak Q_y band at a shorter wavelength than that of chlorophyll *a*.

Phycobilins are linear tetrapyrroles that do not have an associated metal. Depending on the exact structure of the chromophore, these molecules absorb blue-green, green, yellow, or orange light. Carotenoids have a basic structure consisting of two unsaturated, 6-carbon rings joined by a 18 carbon, conjugated double bond ring. They often consist of natural isomers which have markedly different spectral properties. Spectrally, all of these carotenoids display blue and/or blue-green absorption bands that partially overlap the Soret bands of Chlorophyll and, depending on the nature of the overlap, either facilitate the transfer of excitation energy to, or remove excitation energy from, chlorophyll.

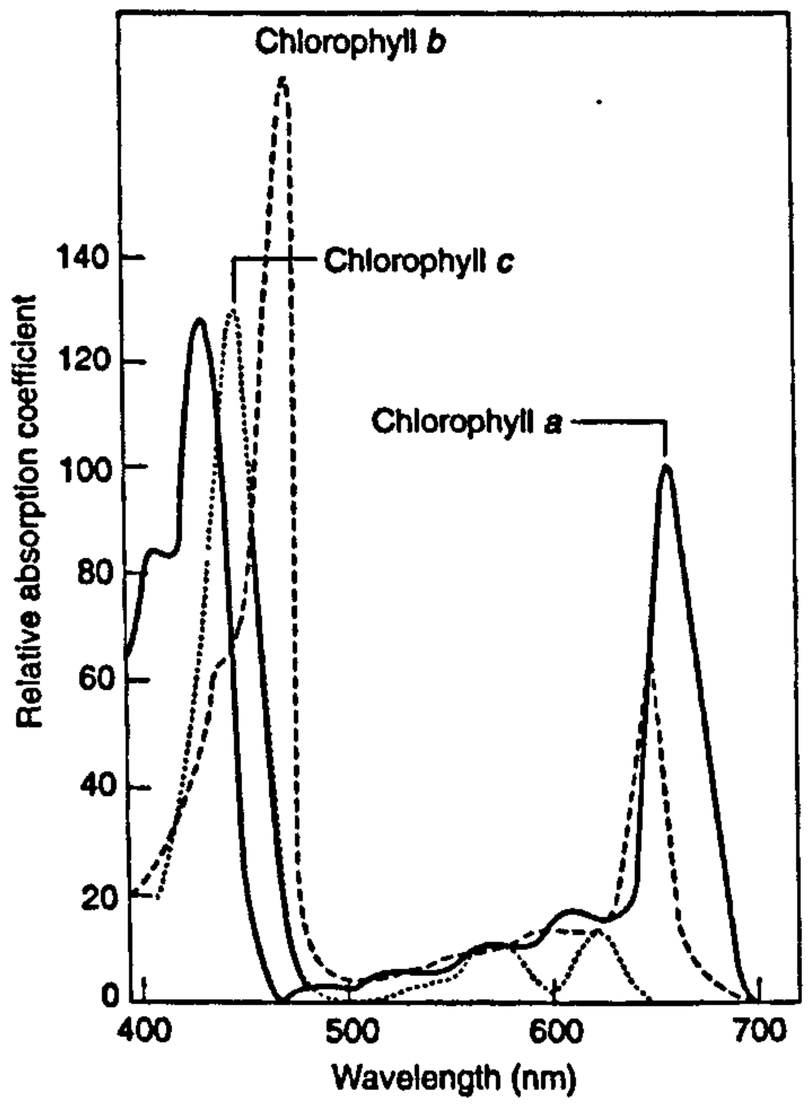

Figure 3.4: The normalized absorption spectra of chlorophylls a, b and c. Both chlorophylls a and b have relatively large absorption bands in the red region, while chlorophyll c has small absorption bands in the corresponding region (Falkowski & Raven 1997).

In summary, the principal chlorophyll absorption occurs in the short wavelength blue and the long wavelength red regions of the visible spectrum. Absorption in the blue region is more intense than red for chlorophylls *a* and *b*, and considerably more

intensive for chlorophyll *c* (Figure 3.4). Carotenoid absorption peaks occur in the blue spectral region. Phycobilins absorption (depending on the species) peaks at green, yellow and short red wavelengths. As a result, chlorophylls appear green, carotenoids appear orange and phycobilins appear either red or blue.

[b] Absorption by suspended sediments

Following electromagnetic studies, the effects of electrical permittivity ϵ, the magnetic permeability μ, and electrical conductivity σ can be summarized compactly in terms of complex index of refraction, $m=n-ik$, where $i=\sqrt{(-1)}$ (Mobley, 1994) . The real part n, of m, is usually called the 'the index of refraction and the imaginary part, k, is called the (dimensionless) electrodynamic absorption coefficient. Although n and k are collectively called the optical constants, they depend strongly on wavelength. The explicit dependency of m on ϵ, μ and σ is given by (Kerker, 1969)

$$m^2 = \mu\varepsilon c^2 - i\frac{2\mu\sigma c^2}{\nu} \qquad \text{eq (3.1)}$$

where c is the speed of light *in vacuo* and ν is the frequency of the electromagnetic wave. These equations can be used to relate n and k to the bulk electromagnetic properties. The real index of refraction $n(\lambda)$ governs scattering both at the interfaces and within the medium. The spectral absorption coefficient $a(\lambda)$ is related to $k(\lambda)$ by (Jenkins and White, 1957)

$$a(\lambda)=\frac{4\pi k(\lambda)}{\lambda} \qquad \text{eq (3.2)}$$

Here λ refers to the wavelength in vacuo corresponding to a given frequency (ν) of the electromagnetic wave. Equations 3.1 and 3.2 summarise the dependency of absorption properties of materials on their magnetic permeability, electrical conductivity and frequency of the interacting photon.

A mineral is defined as a naturally occurring crystalline solid with a definite, but not necessarily fixed, chemical composition. All minerals are composed of chemical

elements in various combinations. The first order control on the structure of a mineral is the nature of the chemical bonding that holds the elements together. The chemical bonds that hold the atoms that form minerals together can be grouped into two categories: bonds that involve valance electrons (ionic, covalent and metallic) and that do not (Van der Wals and hydrogen) (Nesse, 2000).

From equations 3.1 & 3.2, it is clear that the spectral absorption significantly depends on the electrical properties of the material. The ability of minerals to conduct electricity depends directly on the nature of the chemical bonding. Minerals with a significant degree of metallic bonding, in which electrons can migrate freely through the crystal structure, typically conduct electricity with ease. Minerals with dominantly covalent and or ionic bonds are electrical insulators because the electrons are tightly constrained to particular atoms/ions in the structure, and hence are not free to move in response to photon interactions. Because electrical conductivity depends on chemical bonding, one should anticipate that it varies with direction in nonisometric mineral particles.

[c] Scattering properties of particulate suspended material

Scattering can be explained as a deviation in the photon path. This deviation is related to the heterogeneity of the interacting system: heterogeneity on the molecular scale or on the scale of aggregations of many molecules. All scattering, at the microscopic level, can be realised as interactions between the photon and the molecules or atoms of the material. These interactions induce the electrical charges of the matter into oscillatory motion. Accelerated electrical charges radiate electromagnetic energy in all directions; it is this secondary radiation that is called the radiation scattered by the interacting material.

Physics of scattering can be explained using the electromagnetic wave theory (Tipler, 1999). An applied oscillating field induces a dipole moment in the interacting region of matter. These dipoles oscillate at the frequency of the applied field and therefore scatter secondary radiation in all directions. In a particular direction, the total scattered field is obtained by superposing the scattered wavelets, where due account is taken for their phase differences: scattering by dipoles is coherent. In general, these

phase relations change for a different scattering direction; we therefore expect the scattered field to vary with scattering direction. The phase relations among the scattered wavelets depend on the geometrical factors: scattering direction, size and shape. But the amplitude and phase of the induced dipole moment for a given frequency depend on what the material is composed of. Thus, for a complete understanding of particulate scattering it is important to understand how matter responds to oscillatory electromagnetic fields.

Scattering by an arbitrary particle can be explained (Figure 3.5) satisfactorily following the Mie mathematical solutions (Bohren and Huffman, 1983):

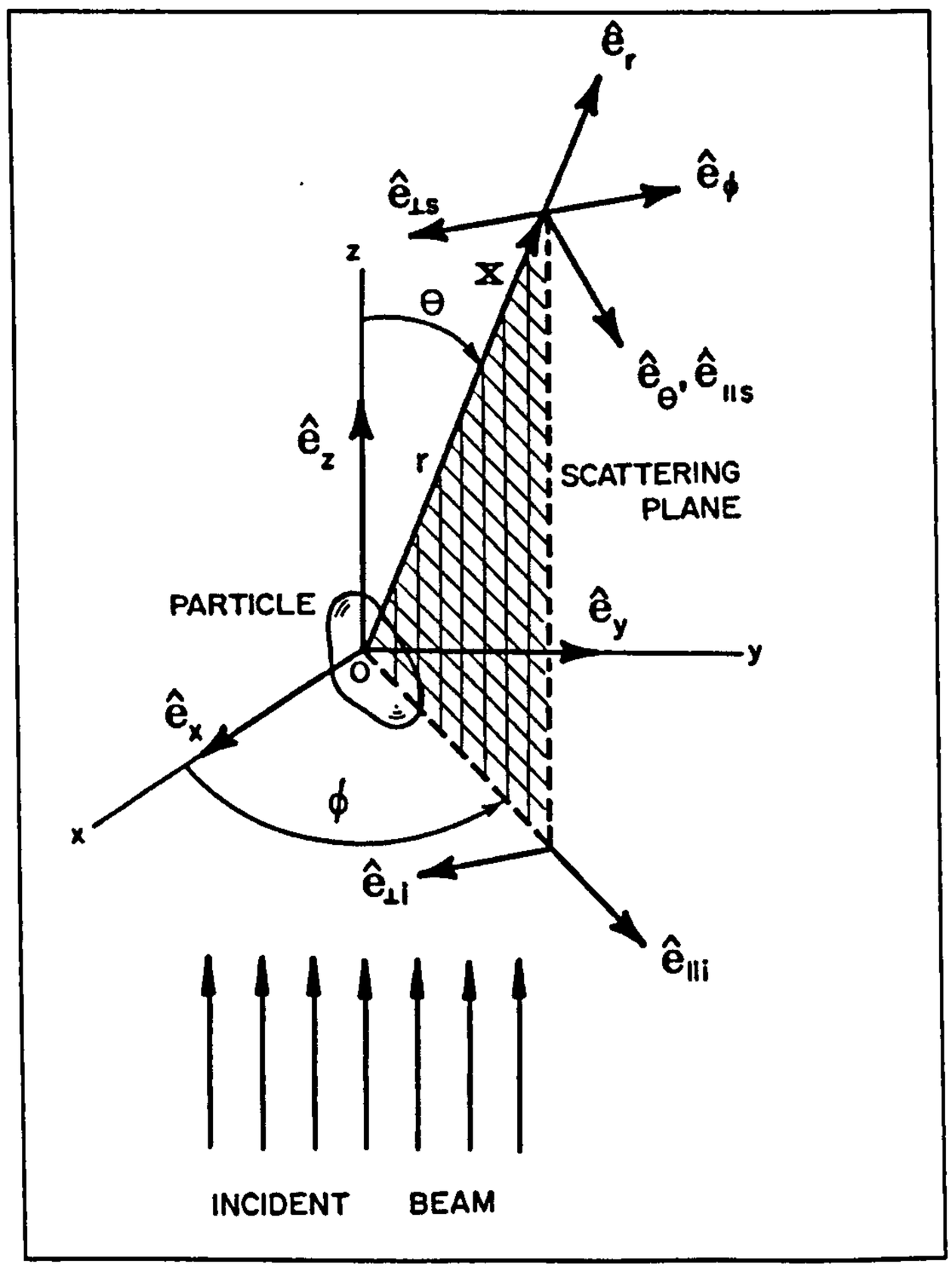

Figure 3.5: Scattering by an arbitrary particle (Bohren and Huffman, 1983).

Following the interaction of light with the arbitrary particle, the rate at which incident energy is scattered across the surface is given in equation 3.3 (Bohren and Huffman, 1983),

$$W_S = \int_A S_S . \hat{e}_r \, dA \qquad \text{eq (3.3)}$$

where S_s is the time averaged Poynting vector of scattered field, $\hat{e}_r$ is the scattering direction and A the surface of the imaginary sphere that surrounds the particle. Using equation 3.3 one can define (equation 3.4) the scattering cross section as the ratio of rate of scattering to incident irradiance (Bohren and Huffman, 1983).

$$C_{sca} = \frac{W_s}{I_i} \qquad \text{eq (3.4)}$$

Equation 3.4 can also be written as equation 3.5 (Bohren and Huffman, 1983)

$$C_{sca} = \int_0^{2\pi}\int_0^{\pi} \frac{|X|^2}{k^2} \sin\theta \, d\theta \, d\phi = \int_{4\pi} \frac{|X|^2}{k^2} d\Omega \qquad \text{eq (3.5)}$$

where X is the vector amplitude scattering, $k = 2\pi m/\lambda$ is the wave number in the medium surrounding the particle, n is the refractive index, and λ is the wavelength of the incident light *in vacuo*. The quantity $|X|^2/k^2$ is sometimes called the differential scattering cross section and denoted symbolically by $dC_{sca}/d\Omega$. Physically, $dC_{sca}/d\Omega$ specifies the angular distribution of the scattered light: the amount of light scattered into a unit solid angle about a given direction.

From equations 3.3, 3.4 and 3.5 the physical interpretation of scattering cross section becomes simple. The scattering cross section, C_{sca}, is the cross sectional area of the incident beam that has power equal to the power scattered by the sphere. The scattering cross sections are therefore related to the corresponding efficiencies by the geometrical cross section of the sphere according to equation 3.6.

$$C_{sca} = Q_{sca}\frac{\pi D^2}{4} \ [\mathrm{m}^2] \qquad \text{eq (3.6)}$$

As given in equation 3.5 and 3.6, these efficiencies and cross sections depend on the various parameters. The relevant parameter describing the material of the sphere and the surrounding medium is the relative complex index of refraction, m_r, defined by

$$m_r \equiv \left(\frac{n_s}{n_m}\right) - i\left(\frac{k_s}{n_m}\right) \equiv n_r - ik_r \qquad \text{eq (3.7)}$$

The relevant parameter describing the size of the sphere is its diameter, D, relative to the wavelength of the incident beam within the medium. The size parameter usually is written as

$$\alpha \equiv \frac{\pi D}{\lambda_m} = \frac{\pi D n_m}{\lambda_{vac}} \qquad \text{eq (3.8)}$$

Thus the difference in the size and refractive index of planktonic material and inorganic mineral particulate material induces variations in the scattering efficiency of these groups, but also within a group itself.

Because of this optical independency of the individual particles, one can simply sum up their individual contributions to scattering, b(λ)

$$b(\lambda) = \int_{all m_r} \int_{all D} C_{sca}(D; m_r; \lambda) n(D) dD dm_r \qquad \text{eq (3.9)}$$

Here n(D)dD is the number of particles per unit volume with diameters between D and D+dD. Corresponding equations can also be written for back scattering.

3.2.3 Water

Optically active particulate and dissolved material introduced in sections 3.2.1 and 3.2.2 is suspended, in natural waters. So it is important to also look into the optical behaviour of water and include its contribution to the total optical signature.

In consideration of natural water, pure water is taken to imply water that is free from the optical effects of terrestrially and/or atmospherically derived organic and inorganic matter. Thus, "pure water" would be defined as a chemically pure substance comprised of a mixture of several water isotopes, each of different molecular mass (Bukata *et al.* 1995). The absorption, the scattering, and the total attenuation coefficients used in additive optical property equations refer to such water where in, the only absorption and scattering is a consequence of water molecules.

Pope and Fry (1997) presented the spectral absorption coefficient of pure water (Figure 3.6), $a_w(\lambda)$, in the wavelength region of oceanographic interest, 380 nm $\leq\lambda\leq$ 700 nm. Absorption spectrum have been obtained with a integrating cavity technique and are in good agreement with results from a photothermal probe beam deflection technique thus providing critical evidence that the new absorption data in the blue are more reliable than previously published data (Smith and Baker, 1981). There is also evidence (Pegau and Zaneveld, 1992) that absorption by water is weakly dependent on temperature, at least in the red and near infrared and perhaps also slightly dependent on salinity.

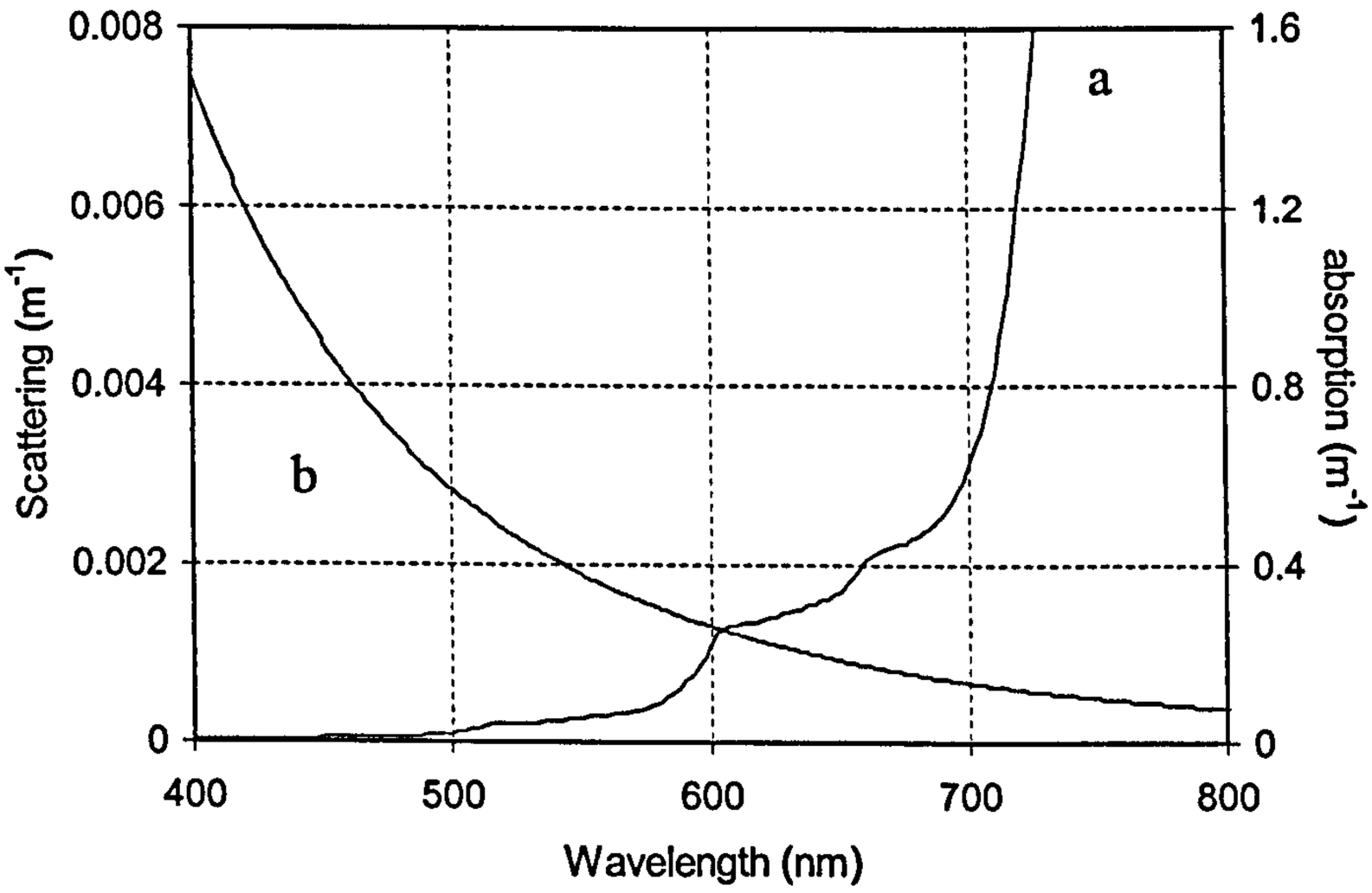

Figure 3.6: Absorption and scattering coefficients for pure water. The line [a] represents the absorption by pure water (Pope and Fry, 1997). The line [b] represents the scattering by pure water (Morel, 1974)

Raman (1922) and Shuleikin (1922) first pointed out the fundamental role played by small-scale scattering in natural waters. Morel (1974) has reviewed in detail the theory and observations pertaining to scattering by pure water and pure sea water. Random molecular motions give rise to fluctuations. In the number of molecules in a given volume, ΔV, where ΔV is small compared to the wavelength of light but large compared to atomic scales. The Einstein-Smoluchowski theory of scattering relates these fluctuations in molecule number density to associated fluctuations in the index of refraction, which give rise to scattering. In sea water the basic theory is the same, but random fluctuations in the concentrations of the various ions (Cl-, Na+, etc.) give a somewhat greater index of refraction fluctuations and hence greater scattering. For such waters the scattering is given by (Mobley 1994)

$$b_w(\lambda) = 16.06\left(\frac{\lambda_0}{\lambda}\right)^{4.32} \beta_w\left(90°;\lambda_0\right) \qquad \text{eq (3.10)}$$

Inorganic salts dissolved in natural waters affect the absorption and scattering occurring within the water column. However the most significant absorption due to dissolved salts are observable at ultraviolet, rather than visible, wavelengths since the electronic absorption bands of dissolved inorganic salts are at values of $\lambda < 300$ nm.

Visible light scattering by dissolved inorganic salts, which displays the same spectral dependence as visible light scattering by pure water, accounts for ~20-30% of the total scattering in oceanic waters of average salinity 35 kg/m^3. Molecular scattering of light by mid-oceanic pure water plus dissolved organic salts is generally insignificant when considered in relation to the total light attenuation appropriate to these waters. Spectral analyses of dissolved aquatic gases reveal that only oxygen absorbs light at the visible wavelengths (Bukata *et al.,* 1995). However, even in oxygen-rich waters, the concentrations of dissolved oxygen are insufficient to produce consequential changes to bulk absorption properties of natural waters.

3.3 Remote sensing

The optical independency of all the colour producing agents enable the addition of specific optical properties as given in equations 3.11, 3.12 and 3.13.

$$a(\lambda)=a_w(\lambda)+\sum_{i=2}^{N}a_i(\lambda) \qquad \text{eq (3.11)}$$

$$b(\lambda)=b_w(\lambda)+\sum_{2}^{N}b_i(\lambda) \qquad \text{eq (3.12)}$$

$$b_b(\lambda)=b_{bw}(\lambda)+\sum_{2}^{N}b_{bi}(\lambda) \qquad \text{eq (3.13)}$$

Where N is the number of optically active marine constituents that can contribute towards the total optical property.

Equations 3.11 and 3.13 can be considered to construct the remote sensing signal above the water surface following the suggestions of Gordon *et al.* (1988),

$$Rrs \propto \frac{b_b(\lambda)}{a(\lambda)+b_b(\lambda)} \qquad \text{eq (3.14)}$$

Chapter 4 : Measurements and methods

To understand the marine optical environment, and consequently above water remote sensing signal, it is essential that the variety and quantity of optically active constituents are understood. This chapter introduces different measurement techniques and methods to quantify biogeophysical components, which are suitable for optical monitoring investigations.

4.1 General principles, error and accuracy

Accuracy is very difficult to maintain in sea water sampling, because of high variability associated with the environment over which one has no control. This high variability is a major source of error in final estimations. In general, the term 'error' indicates the mistakes which can be avoided. During sampling procedure, the error may not be completely eliminated, but it can be minimized by applying suitable sampling techniques. The selection of a suitable sampling technique strongly relies on the understanding of the environment and purpose for which it will be used.

Error in a value can be categorised as either systematic or random error. The systematic error tends to influence the measurement and to produce results that are consistently either too low or too high (leading to bias). The systematic error may occur in the sampling procedure or by the contamination of the sampling. Bias is the most serious form of error because the error is systematic and will, therefore, appear in the results from all samples taken using a particular method. The consequence will be that the average from a number of parallel samples will have the same bias as the individual sample. Very often it is difficult to detect a systematic deviation from the true value because the true value is usually unknown in fieldwork. Hence, systematic errors during the sampling procedure are difficult to detect. In some cases, the bias in the sampling procedure may be detected by means of an obvious disagreement of a known correlation of two constituents or properties. So, it is, obvious that sampling devices and sampling techniques should be examined thoroughly before any samples may be relied upon.

The second category of errors is the random errors. They are such that the results of repeated analysis of the same sample, under identical conditions, will vary. These errors are caused by the type of instrumentation used, personal errors, and errors inherent in the method itself. In most cases it is possible to recognise these random errors and obtain a reasonable estimate of their magnitude. The magnitude of random errors can be reduced by repetition of the analysis. Random errors are always present and independent of the existence of systematic errors.

The two terms generally used for characterising results are precision and accuracy. Precision is a measurement of the uniformity of results of different independent analyses from the same sample. Accuracy is related to the deviation of the determined value from the true value. Therefore, the accuracy is influenced by the sum of all the errors. The result of an analysis is not accurate until both the systematic and the random errors are minimal. It is obvious that the precision is easier to express in numerical terms, but accuracy is more informative.

Various detailed investigations were carried out to define the protocols for measuring biogeophysical parameters. JGOFS (1994), REVAMP (Tilstone and Moore, 2002), COLORS (2001) and Ocean Optics protocols for satellite ocean colour sensor validation (Muller and Austin, 1992) are some of the international projects that have clearly defined the protocols for such investigations. In this research, all suitable methods proposed by the above publications were followed to achieve accuracy in the measurements made.

4.2 Measurement of Total Suspended Matter (TSM)

This section explains the procedure for the estimation of TSM in terms of its weight. Particles in suspension are separated from sea water by filtration using a glass fibre filter. The net weight of material collected on this filter gives TSM in mgl^{-1}.

The methodology (COLORS, 2001) for this procedure is as follows:

- GF/F filters (0.7 μm) are pre-ashed at 450°C for 1 hour.
- Filters are then pre-washed in MilliQ water to remove friable fractions that can be dislodged during filtration. Not more than 20 filters are soaked at a time together for 5 minutes in 500 ml of MilliQ water.
- Place the filters on the shiny surface of clean aluminium foil.
- Dry the filters in a hot air oven at 75°C for 1 hour.
- Pre-weigh dry filters to 5 significant figures.
- A volume of seawater should be filtered through pre-washed, pre-ashed and pre-weighed 0.7 μm filters. The volume used is dependent on the amount of particulate material present in the water.
- Multiple replicates should be taken to quantify sample variability (in this research three sub samples were used to observe the variability). A blank filter should be used for each sample, to calculate the sampling errors.
- After seawater filtration, at least 50 ml of distilled water is filtered through the apparatus to remove any salt. The outer edges of the filter are washed before gently removing the filter.
- The filters are dried in a oven at 75 °C for 24 hours, after which they are stored in a dessicator before weighing. The value thus obtained gives the mass of particulate material collected on the filter. Using the volume of the seawater filtered, it is possible to convert this mass in to the concentration of TSM (mgl^{-1}).
- These filters can further be ashed at 500 °C for 5 hours to remove the organic content and calculate the inorganic component concentration in TSM.
- *Blank filter correction*: As mentioned in the above procedure, it is recommended that blank filters are used for every TSM measurement. These blanks are used to verify the performance of the balance, oven and dessicator and to identify the introduction of possible handling errors. All TSM measurements made for this research also included blank measurements.

Blank correction:

B_L=Final weight of blank filter – Initial weight of blank filter eq (4.01)

Correction to sample weight collected on filter W_{SF}:

W_{SF}=Final weight of filter with sediment – B_L eq (4.02)

A blank correction should only be applied when B_L>0.0001 g (Linde, 1998)

Figure 4.1 is a compilation of surface TSM measurements made in 2002-2003 off Plymouth, the black line represents the difference in weight of the sample filter (WSF). This difference in weight indicates the amount of sediment collected. The grey colour line represents the difference in blank filter weights (BL). Following the protocol (Linde 1998), for all samples with BL > 0.0001 g, the blank correction was applied.

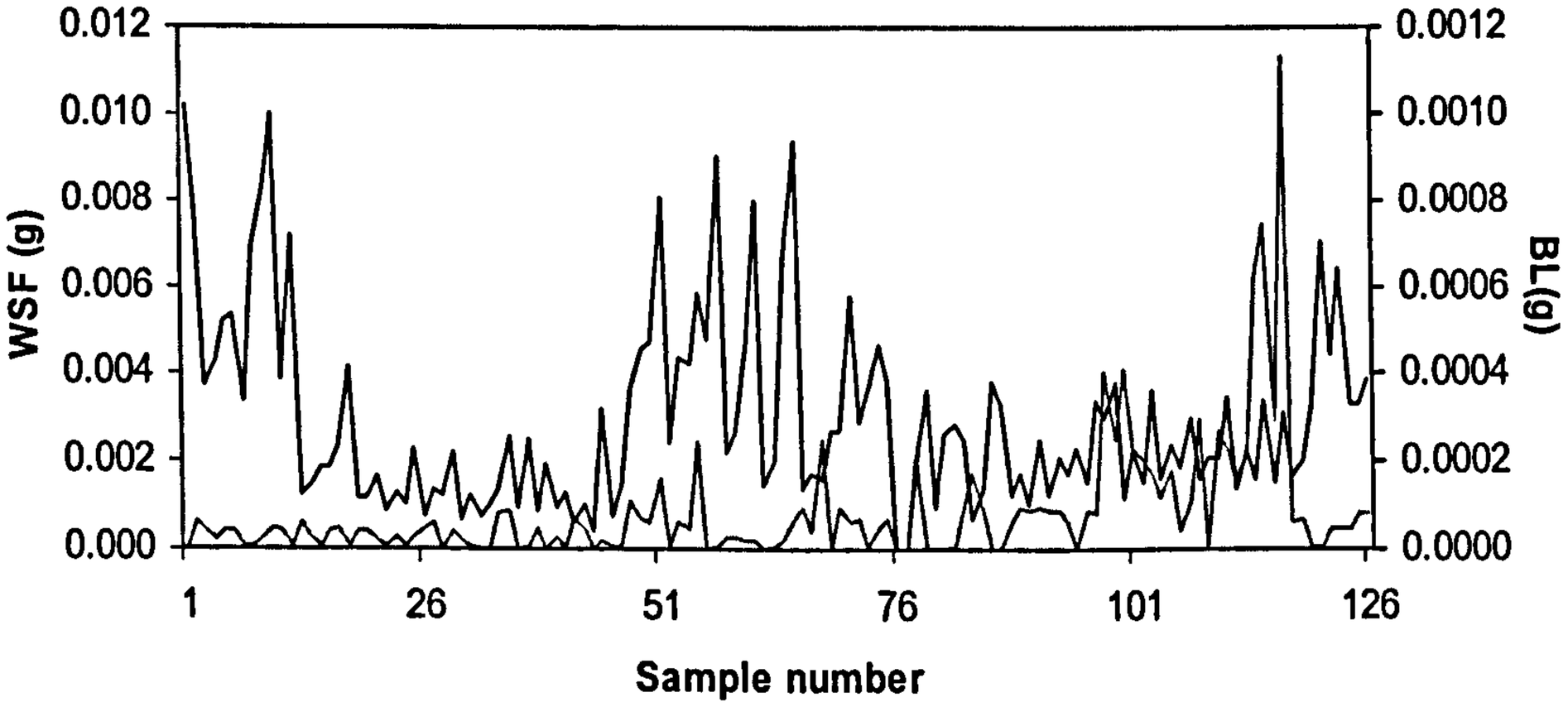

Figure 4.1: Weight of sediment and difference in blank filter weight in grams. The black line represents WSF and BL is indicated by the grey line. Data collected in Breakwater and Barn Pool (2002-03).

Calculating the blank filter difference as a percentage of the respective sample weight (%BL), values range between 0 and 38%. The mean %BL is around approximately 4% of the sample weight. Higher percentage values indicate the introduction of significant handling errors, which are excluded from further analysis.

- *Precision in measurements*: By definition, precision indicates the ability to reproduce the results from the same sample. The standard deviation of the measurements is therefore a good indicator of precision as it clearly explains the spread of the distribution curve. Figure 4.2 gives the spread of the distribution curve for the TSM measurements made in 2002-2003. The vertical bars represent the spread of the data through the use of standard deviation. It is

obvious that a narrow distribution curve indicates higher precision in the analytical procedure

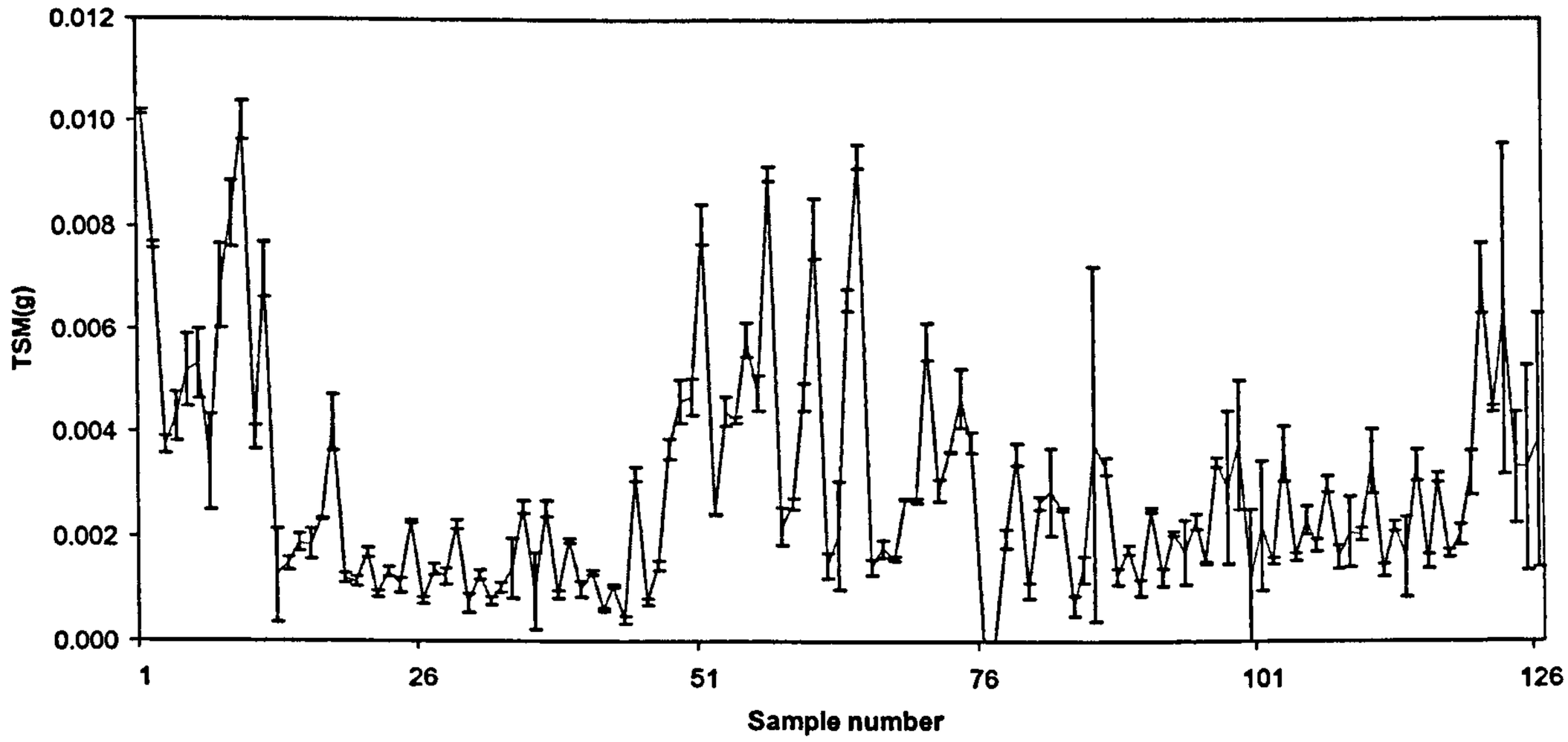

Figure 4.2: TSM measurements from Breakwater and Barn Pool (2002-03). The vertical bars indicate the standard deviation for the three replicate samples.

- Samples which are the source of large deviations as indicated in standard deviations are manually identified and removed before proceeding with further analysis.

4.3 Absorption by Chromophoric dissolved organic material

By definition, CDOM is all the chromophoric dissolved material that which passes through a 0.2 μm filter. Spectrophotometric techniques enable measurements of the light absorbing properties of CDOM. These light absorption measurements are indicators of the amount of CDOM present in seawater.

It is essential to minimize the contamination of the samples by organic materials and the samples should be protected from light to reduce sample degradation. Seawater is collected in a dark amber glass bottle (previously rinsed three times with the sample water before filling). After collection the samples are stored in a cool box for transportation to the lab (3-5 hours). The following procedure (Tilstone and Moore, 2002; COLORS, 2001) is used to measure the absorbance of CDOM.

- Only glass filtration apparatus is used.
- 0.2 μm Whatman Anodisc or polycarbonate filters are used to remove the particulate material.
- 100 ml of MilliQ water filtered through the filter and apparatus to clean the equipment.
- *Blank preparation*: 100 ml of MilliQ water filtered and the filtrate is discarded. This removes any particulate material that could be present in the receiving container. A further 100 ml of MilliQ water is used as a blank.
- *Sample preparation*: 100 ml of sample is filtered at a vacuum pressure of 120 mm Hg. The receiving flask is shaken thoroughly and the filtrate is discarded. Finally, at least 250 ml of seawater is filtered and transferred into a clean cuvette. These samples can also be stored in a refrigerator for up to 24 hours.
- When using refrigerated samples, the samples are allowed to warm up so that the sample and blank are at the same temperature before measurements are taken.
- Before transferring the sample, the cuvette is rinsed with MilliQ water and the outer surfaces are wiped with lint free wipes.
- The spectrophotometer is allowed to warm up for 30 minutes. If necessary the optical windows are cleaned with a lint free laboratory tissue.
- An air to air baseline is recorded when the spectrophotometer is ready. This baseline should be spectrally flat with <0.0005 A units.
- A MilliQ autozero is performed between 350 to 800 nm by placing the cuvette filled with MilliQ water and nothing in the reference cell. This autozero is followed by a MilliQ scan in the same setup. Such MilliQ scans are obtained between every sample to check the stability of the instrument.
- Finally, a scan is performed on the sample in the cuvette. For the next sample the same cuvette is used but after cleaning with MilliQ water. The inside of the cuvette is rinsed three times with 5 to 10 ml of MilliQ.

- The MilliQ spectra is subtracted from the sample spectra and the absorption coefficient of dissolved organic matter is calculated from the measured absorbance (A_{ys}) as follows

$$a(\lambda)=\frac{2.303A_{ys}(\lambda)}{l} \qquad \text{eq(4.03)}$$

where l in meter is the cuvette path length. In this work we have used a Perkin and Elmer Lambda 2 spectrophotometer with a 10 cm cuvette.

- *CDOM spectra correction and analysis*: From several earlier studies (Bricaud *et. al.,* 1981, Kirk 1994), the absorption behaviour of CDOM is understood to be wavelength dependent. It normally exhibits an exponential behaviour within the UV and visible region. Beyond 600 nm, all measured values are expected to be low and decreasing only slightly with increasing wavelength, but this didn't seem to be the case with most of the spectra obtained during this research. Along with the exponential behaviour the spectra showed various artefacts, with potential sources being the sample temperature difference, refractive effects (Green & Blough 1994) and presence of small (<0.2 μm) particulate material (Figure 4.3).

- In 15% of the total samples measured, a negative peak was observed at 730-735 nm, which is probably a temperature artefact (Ferrari, 2000). A simple solution was to delete data beyond 700 nm, and avoid the inclusion of the temperature artefact in further analysis. In 47% of the total samples a non-zero absorbance is observed in the infrared region, which suggests the possible presence of scattering colloidal material. This highlights the need to correct the data for scattering effects before further analysis.
- Correction procedures suggest spectra subtraction by values such as $a_g(700)*(700/\lambda)$ (Bricaud *et al.,* 1981), $a_g(650)*(650/\lambda)$ (Hojerslev *et al.,* 2001), $a_g(650)$ or $a_g(700)$ (Ferrari 2000), average $a_g(700\text{-}800)$ (Blough *et al.,* 1993) and $a_g(650\text{-}700)$ by subtraction. The objective of these corrections is to obtain an improved R^2 value for the exponential fit in the of 400-500 nm range from which $a_g(440)$ is determined. This particular 100 nm range is chosen to derive absorption at 440 nm, which is more suitable in terms of remote sensing applications (Kirk 1994). For this data set, a correction by subtracting $a_g(650\text{-}700)$ was found to be effective with improved R^2.

- Most investigators have calculated the CDOM slope through a linear least squares regression of the log-transformed absorption data (Bricaud *et al.*, 1981; Blough *et al.*, 1993; Green and Blough, 1994). However, it was pointed out (Stedmon *et al.*, 2000; Blough and Vecchio 2002) that fitting the data to a exponential form, using a nonlinear least squares fitting routine represents a better approach, owing to the relatively greater weighting given to the higher, and better measured, absorption values at short wavelengths. Following this suggestion, in this research a nonlinear approach was used to calculate the slope of CDOM absorption spectra.

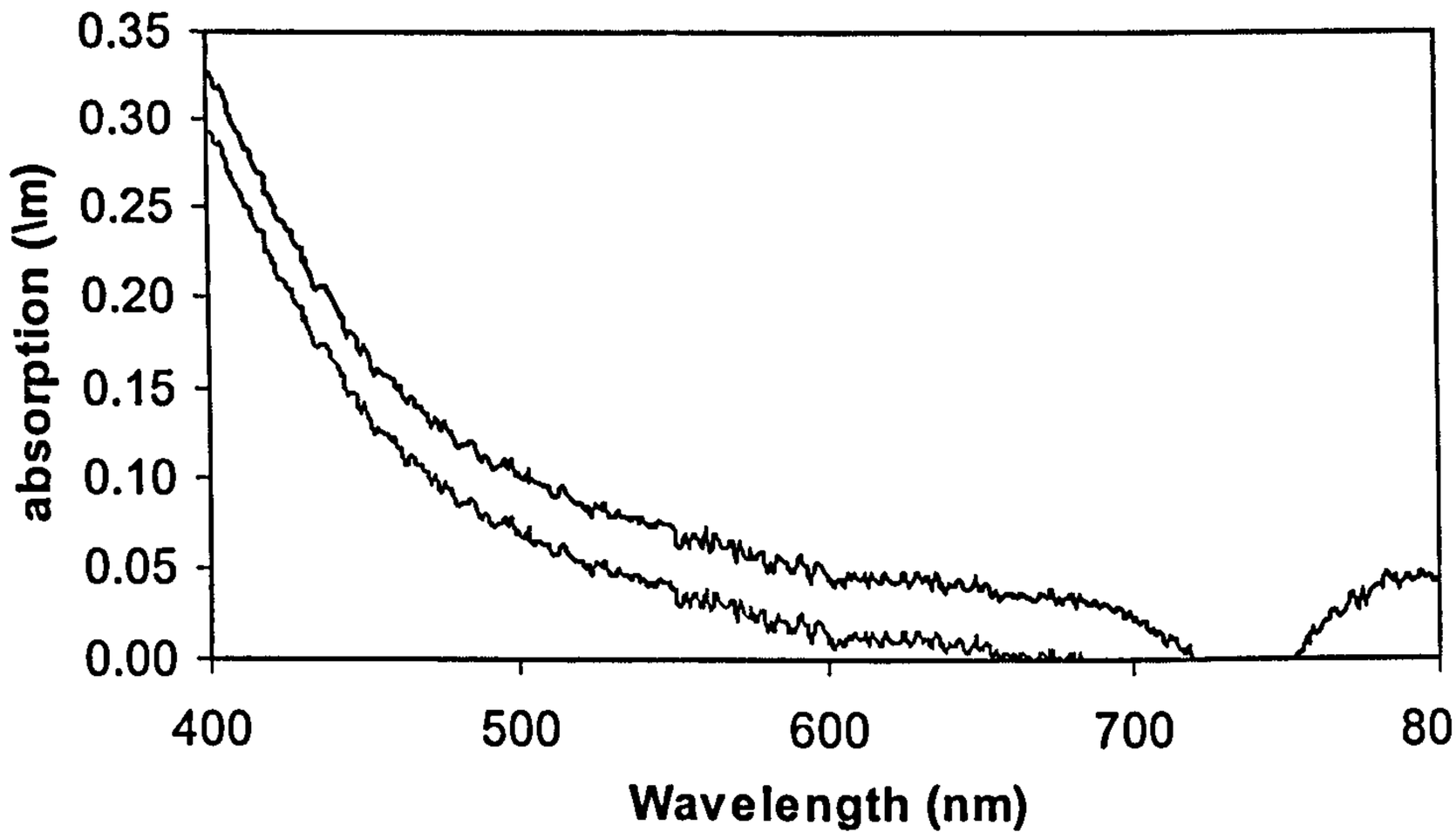

Figure 4.3: Example of CDOM absorption spectra for Barnpool (April 14, 2003). The black line is the uncorrected spectra with a negative peak at 734 nm. The grey line (bottom) represents the corrected spectra.

4.4 Measurements of absorption spectra of pigmented and non-pigmented aquatic particulate material retained on filter papers

The light transmission measurement of aquatic particles retained on filter papers is an accepted method for the determination of *in vivo* particle absorption (Tassan and Ferrari 1995). This procedure measures the absorbance by particles retained on the filter using a dual beam spectrophotometer and transformation of this quantity into a suspension equivalent absorption coefficient $a_{pm}(\lambda)$ [m^{-1}].

- *Instrument*: A dual beam spectrophotometer equipped with a 60mm diameter, barium sulphate coated integrating-sphere attachment, is used for this purpose. The ratio of apertures to sphere surface is ~7.5% (Tilstone and Moore, 2002). The correction for the difference in the beam efficiencies is automatically performed (Tassan and Ferrari, 1995). Measurements were performed here in the 400-750nm spectral range with a 1nm resolution.
- *Calibration and Quality check*: Spectra are visually and/or automatically checked, in particular for:
  - presence of a significant peak around 665 nm in $a_{dp}(\lambda)$ spectra, as a sign of incomplete bleaching of the sample.
  - abnormal if the ratio of $a_{ph}(443)/a_{ph}(665)$ is less than unity.
- *Sample preparation*: The samples were prepared in the following way,
  - Filtered through a 0.7μm pore size, 47mm, Whatman GF/F filters.
  - Proper care taken to avoid contamination, maximize the retention and collect an adequate particle concentration on the filter.
  - Filtration carried out under low vacuum pressure (below 120mmHg) to prevent particle breakage and pigment degradation.
  - Filters stored in liquid nitrogen if measurements are not carried out immediately.
- *De-pigmentation*: A bleaching solution with a concentration of 3.33% NaClO, (1% active chlorine) was used to bleach the pigments from the particulate material on the filter. Up to four drops of bleaching solution is recommended (Tassan and Ferrari 1995) and de-pigmentation takes approximately 3 minutes. About 5 ml of MilliQ water was filtered after bleaching to remove any NaClO residual. Disappearance of the peak at 675 nm in the bleached sample and evidence of a concave shape of the optical density spectrum near 440 nm can be considered as an indication of complete bleaching.
- *Measurements and processing*: The measurement methods and data processing technique explained in Tassan and Ferrari (1995; equations 11 to 14) were used to convert the measured absorbance of the filter-retained particles into the equivalent particle suspension absorption.

These absorption measurements were measured and made available through the COLORS project.

4.5 Electronic sizing and counting of particles

Particle size and number measurements for the samples collected in this research were made using a Model Z_B coulter counter.

- *Instrument*: The instrument consists of an electronic cabinet and a sampling stand. The electronic unit contains a digital counter, an oscilloscope screen, upper and lower threshold controls, aperture current and amplification switches and a zero reset switch. The sampling stand consists of an aperture tube, a mercury manometer, a control stop clock, two electrodes, a vacuum pump, and a 35× microscope for viewing the aperture.
- *Basic theory*: The Coulter Counter determines the number and size of particles suspended in an electrically conductive liquid (Figure 4.4). This is done by forcing the suspension to flow through a small aperture having an immersed electrode on either side. As a particle passes through the aperture, it changes its resistance between the electrodes. This produces a voltage pulse of short duration having a magnitude proportional to particle size. The series of pulses is then electronically scaled and counted.
- *Corrections*: By taking a series of counts at selected threshold levels, data is directly obtained for plotting cumulative frequency versus particle size. Integration of all or part of the resultant curve provides a measure of the particle content of the suspension. Before plotting, the counts are first corrected for coincident particle passages. These corrections are quite precise and if kept to a moderate level, an overall accuracy of measurement better than 1% is readily achieved. This is due in part to the large numbers of particles counted, which provide low statistical deviations.
- *Sample processing*: The sample was processed immediately. Sample is gently stirred to keep the particles in suspension, before introducing it to the counter. The background measurement was performed for every sample measured with the background electrolyte is prepared (using 0.2 μm filter) from the same sea water as the sample. Two measurements of each sample were saved and in case of major discrepancies, the sampling was repeated. Multisizing-II software provided along with the instrument was used to transfer the data from the electronic unit to the computer. Finally the data was saved as ASCII format for further analysis.

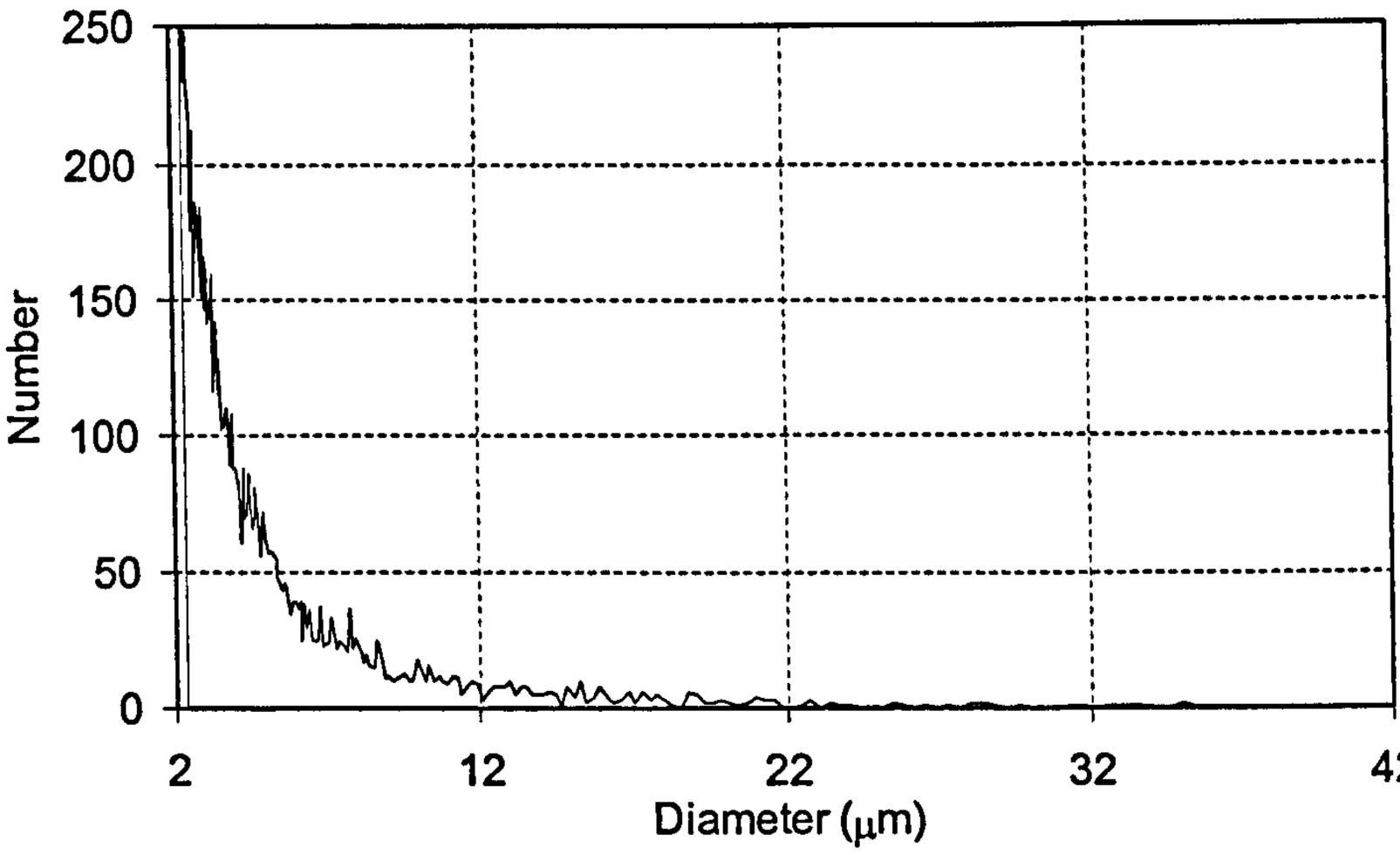

Figure 4.4: Differential particle size distribution. The dark line represents the number of particles present in 500 ul of sample (Barn Pool, 04 August, 2003).

For this research Coulter counter results are further processed to calculate the particle size distribution. A detailed explanation is presented in Section 5.2.1.

4.6 PML's CTD and Bio-optics rig

Biogeophysical measurements for this research were collected using PML's CTD & bio-optics rig (Fig 4.5). This rig is basically a collection of instruments to measure temperature, density and optics. It is constructed on a metallic vertical frame and with an extension bar. The vertical frame holds an ac-9, CTD (Conductivity, Temperature and Density), FRRF (Fast Repetition Rate Fluorimeter), data logger and a battery pack and the horizontal extension bar is used to mount Satlantic radiance and irradiance (Satlantic Profiling Multichannel Radiometer[SPMR]) units. Data was processed and made available for this research through the COLORS project database.

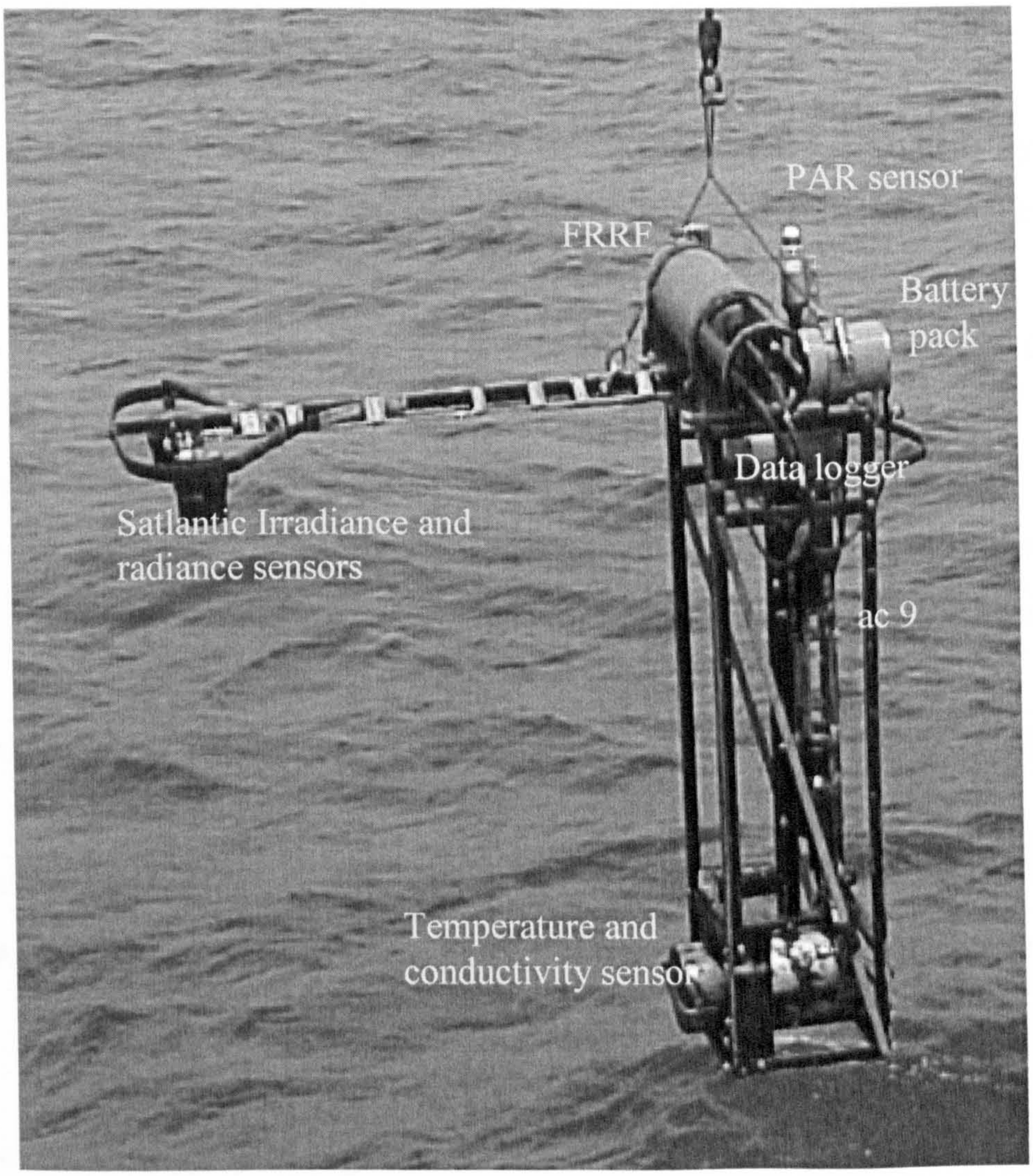

Figure 4.5: PML bio-optics rig.

4.6.1 Salinity and Temperature measurements

Salinity and temperature measurements were made using a custom made CTD (Aanderaa conductivity and temperature sensors), which was attached to the optics rig. The following general rules were maintained during deployment,

Deployment:

- The instrument was deployed from the ship/boat clear from outlets and exhausts.
- The instrument was lowered at approximately 0.1 m s^{-1} and both downward and upward profiles were recorded.
- The instrument was cleaned with fresh water after deployment.

Measurements:

- Salinity in practical salinity units (psu) was estimated by measuring conductivity and corrected with the equation of state of seawater (UNESCO 1981) for temperature and pressure effects.
- Temperature measurements were made by a platinum resistance thermometer, with thermistors being used for rapid response measurements.

Instrument calibration:

- *Temperature*: The instrument was calibrated against a transfer standard laboratory platinum resistance thermometer, which in turn has been absolutely calibrated using a water triple point cell (0.0100 deg. C).
- *Salinity*: The instrument was calibrated using a standard laboratory water bath at three salinities.

Data binning:

- Both temperature and salinity values were binned with an interval of one meter and if number of input samples Nn < 1, data value was removed and replaced by a missing value.
- If the centroid was greater than 25% away from the centre, the data was flagged.

4.6.2 Spectral beam attenuation and absorption coefficient measurements

Spectral beam attenuation (c) and absorption coefficient (a) measurements were made using a WET Labs ac-9 dual path absorption and attenuation meter. The ac-9 concurrently determines the spectral beam attenuation and absorption over nine wavelengths, has a path length of 25 cm and is equipped with a bandpass capability of 10 nm per channel.

- *Deployment*: The instrument was deployed, upright on the vertical frame by means of a winch with a lowering speed of 0.1-0.2 m s^{-1}.
- A small pump brings the water through the ac-9 flow tubes. Flow rate was maintained above 1 litre per minute, and tubing was covered with black tape to avoid direct light from entering.
- Air bubbles can affect measurements. It was assumed that putting the instrument at depth would help purge the system of bubbles, so only the up-cast profiles were used.
- Simultaneous *in situ* temperature and salinity data were collected.
- *Calibration*: Calibration is performed by passing Milli-Q water through the flow tubes and measuring the resulting offsets. The calibration can be simultaneously done for both *a* and *c* or for each successively.
- *Maintenance*: The instrument was cleaned with soap water and methanol.

Post-processing

- *Temperature and Salinity corrections*: After the data collection, the raw data must be corrected for the *in situ* temperature and salinity effects. These effects can be removed by applying, the following algorithms (Wetlabs ac-9 protocol Document, Revision B, 2000) :

$$c_{mts}(\lambda) = c_m(\lambda) - [\psi_t(\lambda) * (T - T_{cal}) + \psi_{sc}(\lambda) * (S - S_{cal})] \qquad \text{eq (4.04)}$$

$$a_{mts}(\lambda) = a_m(\lambda) - [\psi_t(\lambda) * (T - T_{cal}) + \psi_{sa}(\lambda) * (S - S_{cal})] \qquad \text{eq (4.05)}$$

Where c_{mts} and a_{mts} are corrected *a* and *c* values, T and S are the temperature and salinity of the water during measurement, T_{cal} and S_{cal} are the temperature and salinity of the water during calibration Ψ_t, Ψ_{sc} and Ψ_{sa} define the temperature and salinity dependency of *a* and *c*.

- *Scattering correction of absorption coefficient*: the portion of the scattered light not collected by the reflecting tube absorption meter causes the instrument to over estimate the absorption coefficient. This over estimation can be compensated by applying the following correction, which uses a reference wavelength at 715 nm to determine the proportion of scattering and also assumes no absorption at this wavelength (Wetlabs ac-9 protocol Document, Revision B, 2000),

$$a_{mtsb}(\lambda) = a_{mts}(\lambda) - \left(\frac{[c_{mts}(\lambda) - a_{mts}(\lambda)] * [a_{mts}(715)]}{[c_{mts}(715) - a_{mts}(715)]} \right) \qquad \text{eq (4.06)}$$

- *Quality check and data binning*: Quality checks are performed after temperature, salinity and scattering corrections. The following criteria was followed in this procedure:
  - Only data points where $c_{mtsb}(\lambda) \geq a_{mtsb}(\lambda) \geq 0$ were considered;
  - Number of points within the binning layer must be greater than 1.

4.6.3 Spectral irradiance and radiance measurements using Satlantic instrument

Surface downwelling spectral irradiance, $E_s(\lambda)$, subsurface downwelling spectral irradiance, $E_d(z,\lambda)$, and subsurface upwelling spectral radiance, $L_u(z, \lambda)$, were measured using the Satlantic unit mounted on the rig. An $E_s(\lambda)$ unit was placed on the top of the boat to minimize the influence of any shading structures. The irradiance and radiance units on the vertical frame were placed away on an extension bar to avoid any shading from the vertical frame. $L_u(z, \lambda)$ measurements were taken to derive the subsurface upwelling radiance $L_u(0^-, \lambda)$. Subsurface irradiance measurements were made to derive the diffuse attenuation coefficient $K_d(z, \lambda)$ and $K_l(0^-, \lambda)$, where 0^- indicate the values just below the surface.

- *Instrument description*: The measurement system consists of a compact seven channel analog sensor capable of 16-bit performance. The analog signal was digitized by a 16-bit analog to digital converter (DATA-100).
- *Instrument calibration*: A calibration methodology as described in the NASA SeaWiFS protocols (Muller and Austin, 1992) was followed in this project. The irradiance sensors were calibrated using a FEL 1000 W lamp traceable to NIST scale (Walker *et al.* 1987), while the radiance sensors were calibrated with an integrating sphere or with an FEL 1000W lamp and a reference 99% reflectance plaque.
- *Instrument deployment*: The optical measurements were made in stable conditions. The E_d and L_u sensors were deployed towards the sun or the brightest part of the sky and proper care was taken to avoid platform shading. Depth profiling was generally maintained at 0.3 ms^{-1} to make a minimum of 100 samples for each optical depth.
- *Processing techniques*: Primary quality checks included data screening for any rapid change in E_S and ensuring that profiles are smooth in log/linear scale. The data presented for level 1 archive was dark corrected. Records with bad tilt and roll were removed.
- *Data processing*: The profiling data was first processed with the following criteria before forwarding to binning and deriving above surface values. The data processing chain is shown in a flow chart (Figure 4.6).

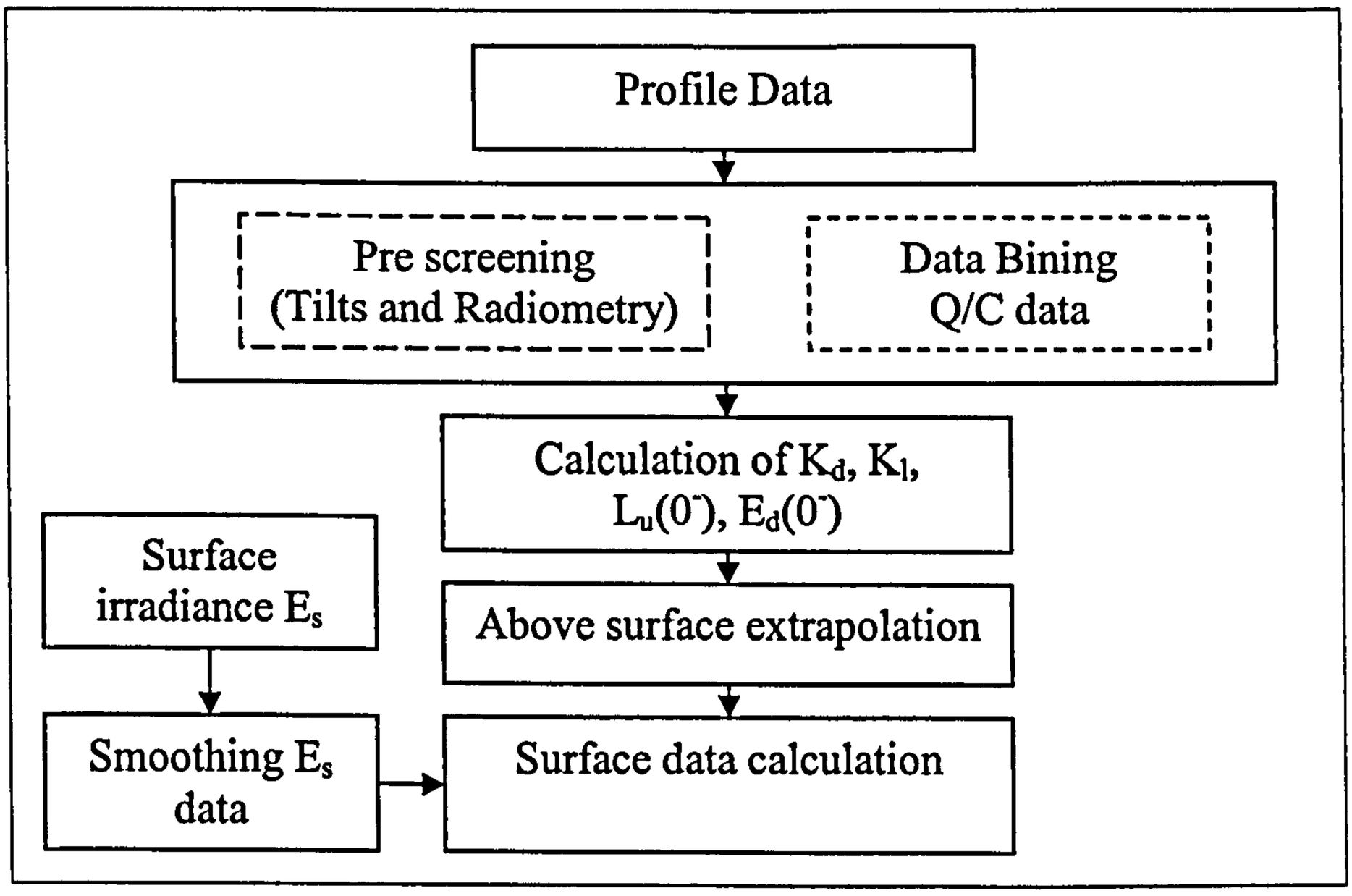

Figure 4.6: Optical data processing chain

- The preliminary data was screened for any off axis records.
- The deck cell data was smoothed according to the SeaWiFS protocols, with the width of smoothing calculated according to the time-base of the individual instruments.
- The radiance and irradiance were normalised for any variations in downwelling surface irradiance.
- The data was screened for radiometry that was out of limits, i.e. where the data is saturated due to sun glitter or at the noise level (10 counts are less).
- The first product was the depth binned bulk radiometry.
- The downwelling irradiance (Ed) and upwelling radiance (Lu) values were depth averaged in 1-metre bins.
- The actual depth accounts for the offsets of the radiometer heads relative to the pressure sensor (these values are given in the Level 1 data files according to the profiling rig geometry).
- The data in the depth bins were checked for symmetry and quality control (QC) flags were given where the centroid was more than 0.25 m away from the expected centre.
- Data was rejected at the depth just below where saturation occurs and just above where the minimum irradiance or radiance occurs.

- Extrapolation of radiance to the surface was done by automatic depth selection, where the data was processed from the surface to the 5% downwelling light level, taking into account the radiometric criteria above. This criterion was suitable where the water column was well mixed and there was no significant bottom reflectance.
- The downwelling irradiance (K_d) and upwelling radiance (K_l) attenuation coefficients were calculated using log linear regression with relative weighting.
- The values of the attenuation coefficients for pure water (K_w) are known and these were used to provide QC flags the data for the K_l and K_d values. Any values of K_d or K_l (except the 685 nm band which is affected by natural chlorophyll fluorescence) with values of less that K_w are flagged. The regression also returns the expected value of radiance and irradiance just below the surface, $L_u(0^-,\lambda)$ and $E_d(0^-,\lambda)$.
- Water leaving radiance was then determined as

$$L_w(\lambda) = R_0 L_u\left(0^-,\lambda\right) \qquad \text{eq (4.07)}$$

where $R_0 \cong 0.529$ is the upward radiance transmittance of the sea surface for normal incidence from below (Ocean optics, 2000).

- Remote sensing reflectance is then calculated as

$$R_{rs}(\lambda) = \frac{L_w(\lambda)}{\left(E_s(\lambda) or\, E_d(0+)\right)} \qquad \text{eq (4.08)}$$

where $E_s(\lambda)$ is downwelling incident irradiance measured above the sea surface and is equivalent to $E_d(0+,\lambda)$.

Chapter 5 : Dynamics of coastal marine optical environment

The dynamics of the coastal marine optical environment is a reflection of changes occurring in the concentrations of the constituent materials. Unlike open ocean waters, the changes in the constituent materials and their concentrations are independent of planktonic material (IOCCG 2000). Variability in concentrations is mostly predictable but occasionally unpredictable, as they are influenced both by seasonal and random events. Even the nonlinearity of the concentration distribution is controlled by complex boundary conditions imposed by the climatology.

Remote sensing is an efficient tool to monitor such complex optical environments in coastal regions. The first step in utilising this tool is to understand how the remotely detected signal is generated. The optical remote sensing signal at the sea surface level is a contribution from all the optically active substances present in the coastal marine environment. By understanding the biogeooptical relationships, it is possible to simulate the above water remotely detected signal. This forms the basic objective of the research conducted for this thesis. This forward approach (Figure 5.1) can be utilised to validate atmospherically corrected remote sensing data as detected by sensors onboard space platforms and aircraft.

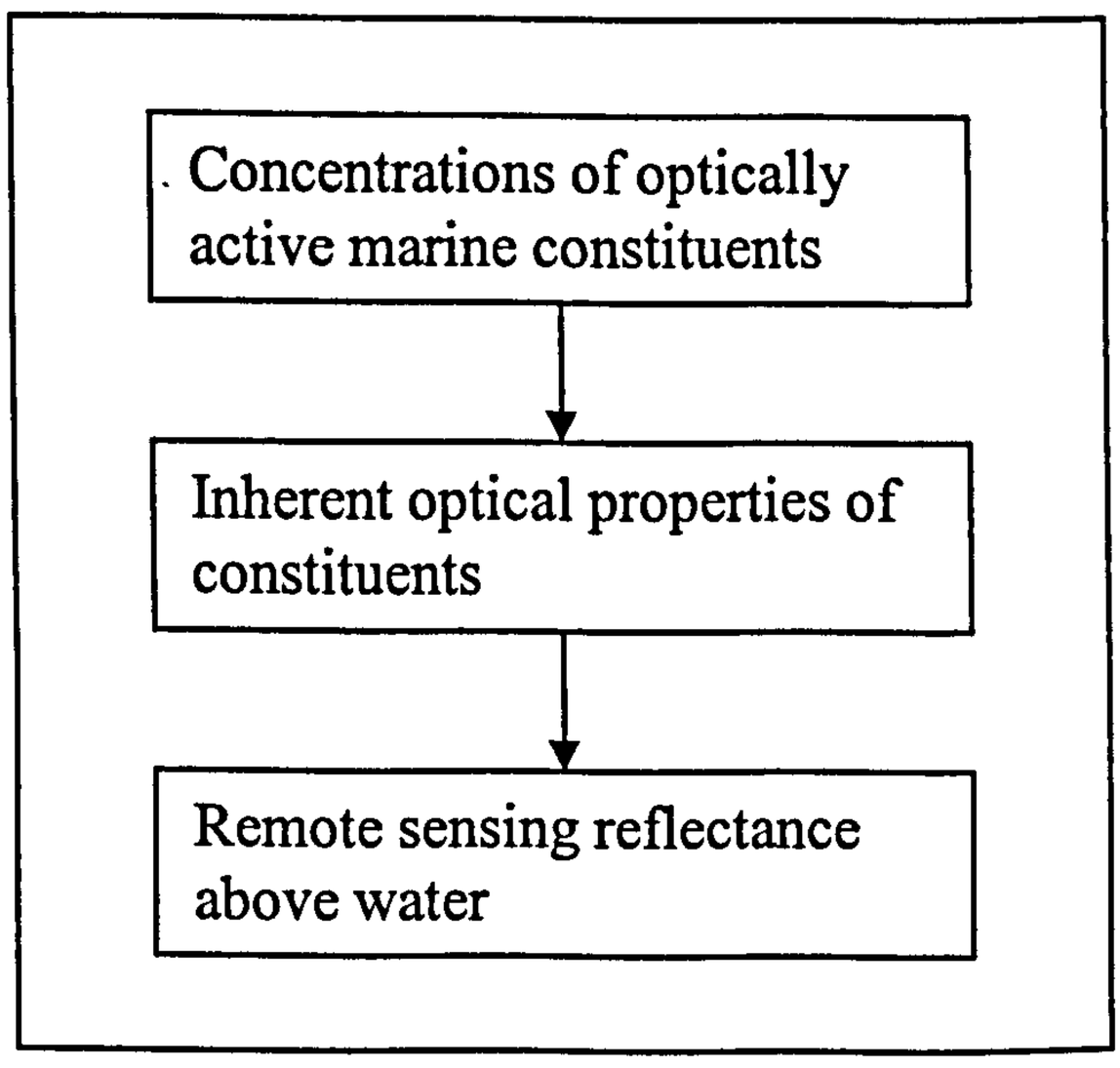

Figure 5.1: Basic scheme explaining forward approach to estimate above water remote sensing signal.

In this research work an inherent optical property based forward model was developed. The model is used to explain the remote sensing signal in coastal waters where non-planktonic material dominates the optical environment. Figure 5.1 presents the basic scheme of this forward approach, with each module of this scheme described in detail.

Chapter 5 is arranged into 3 sections:

- Section I introduces the *in situ* measurements made in coastal waters. These *in situ* measurements define the boundaries of the forward model.
- Section II explains the modelling of particulate optical behaviour and the reconstruction of the remote sensing signal.
- Section III explains various biogeooptical inter-relationships and the development of a semi-analytical approach based forward reflectance model.

Section I: Biogeophysical variations in coastal waters

In this section the variations observed from different biogeophysical measurements in the study area are presented. The objective of this section is to introduce the dynamics of biogeophysical components in coastal waters such as Plymouth Sound. The observations presented in this section are utilised to define the boundaries of various input parameters used in the modelling component of this research. No attempt will be made to explain any oceanographic process, as the data presentation is aimed only at defining the boundaries for the optics model. An explanation of biogeochemical cycles and oceanographic process is beyond the scope of this thesis.

5.1.1 Study area and data set

Data was collected in the coastal waters off Plymouth; sampling stations were located at Breakwater and Barn Pool (Figure 5.2). Barn Pool is near the mouth of the river Tamar and Breakwater is further south (3.5 km from Barn Pool). The coordinates of Barn Pool are 50.356 °N and 04.169 °W and Breakwater is located at 50.557 °N and 04.151°W. Barn Pool and Breakwater stations were chosen as sampling sites as they represent typical coastal waters with high SPM and CDOM concentrations.

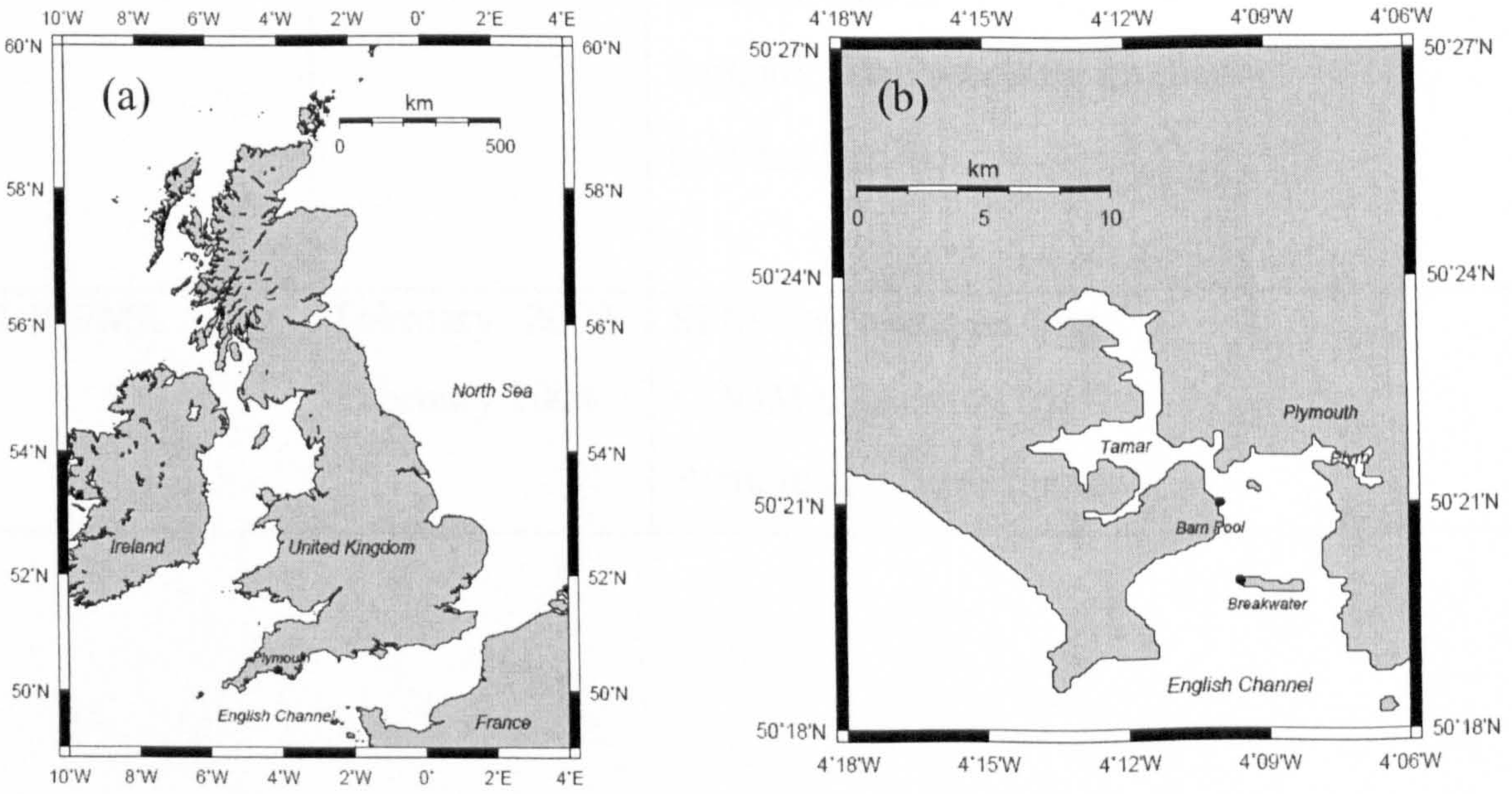

Figure 5.2: Data collection sites in coastal waters of Plymouth: (a) Plymouth on the south-west coast of United Kingdom; (b) sampling sites Barn Pool and Breakwater in Plymouth Sound.

The data set used for this research was compiled from data collected in two research campaigns. The first part of the database was compiled using data collected within the COLORS project. The main objective of COLORS was to establish a European network for long-term measurements for ocean colour remote sensing. Plymouth was chosen as a sampling site to represent the coastal waters of the English Channel. Over a three year period, COLORS provided a series of optical and biogeochemical measurements. The second part of the data set was collected for research (UoP-PML) supporting this thesis (Table 5.1).

Table 5.1: Database compiled for this research.

Project	Year	Measurements
COLORS	October 1998 – September 2000	SPM concentration (mgl^{-1}) CDOM absorption (m^{-1}) non-algal particulate matter absorption (m^{-1}) Salinity (psu) Temperature (°C) ac-9 – absorption (m^{-1}) ac-9 – attenuation (m^{-1}) Satlantic - Upwelling radiance ($\mu Wcm^{-2}nm^{-1}sr^{-1}$) Satlantic-Downwelling irradiance ($\mu Wcm^{-2}nm^{-1}$)
UoP-PML	February 2002-February 2004	SPM concentration ($mg\ l^{-1}$) CDOM absorption (m^{-1}) Particle size measurements

5.1.2 Salinity and temperature

Figure 5.3 presents the temperature and salinity measurements made during the 1998-2000 COLORS data campaign. The solid line represents the data collected in Barn Pool and the dotted line represents the data from Breakwater in both the plots. The temperature variations were similar at both the data collection points. The annual variations in temperature at these stations were in the range of 8.7-19.1 °C. The salinity value fluctuates in the range of 30.304-36.62 psu. The variations in the seawater temperature clearly reflected the influence of the seasonal cycle. The value of salinity was usually around 35.0 psu, but sometimes (at both the sampling stations) there were much lower values that could be influenced by freshwater runoff from the rivers (Tamar and Plym) triggered by heavy rain fall.

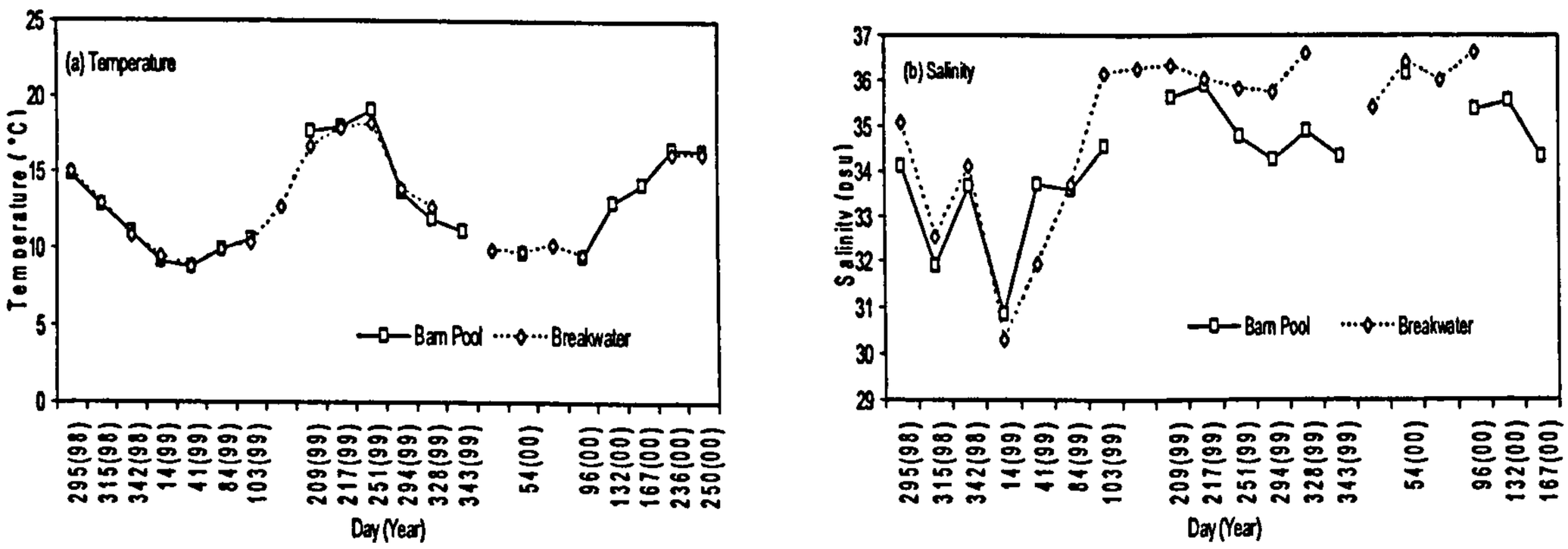

Figure 5.3: Variation of (a) Temperature (°C) and (b) Salinity (psu) in Plymouth Sound. Data collected during COLORS campaign (1998-2000).

5.1.3 Suspended particulate material

The variation in SPM concentrations observed over a period of 5 years are presented in Figure 5.4. The SPM concentrations were observed to range between 0.5-11.0 mgl^{-1}.

The concentrations were observed to be greater in the non-summer seasons at both the sampling stations, which could be the influence of rainfall and high runoff from the rivers.

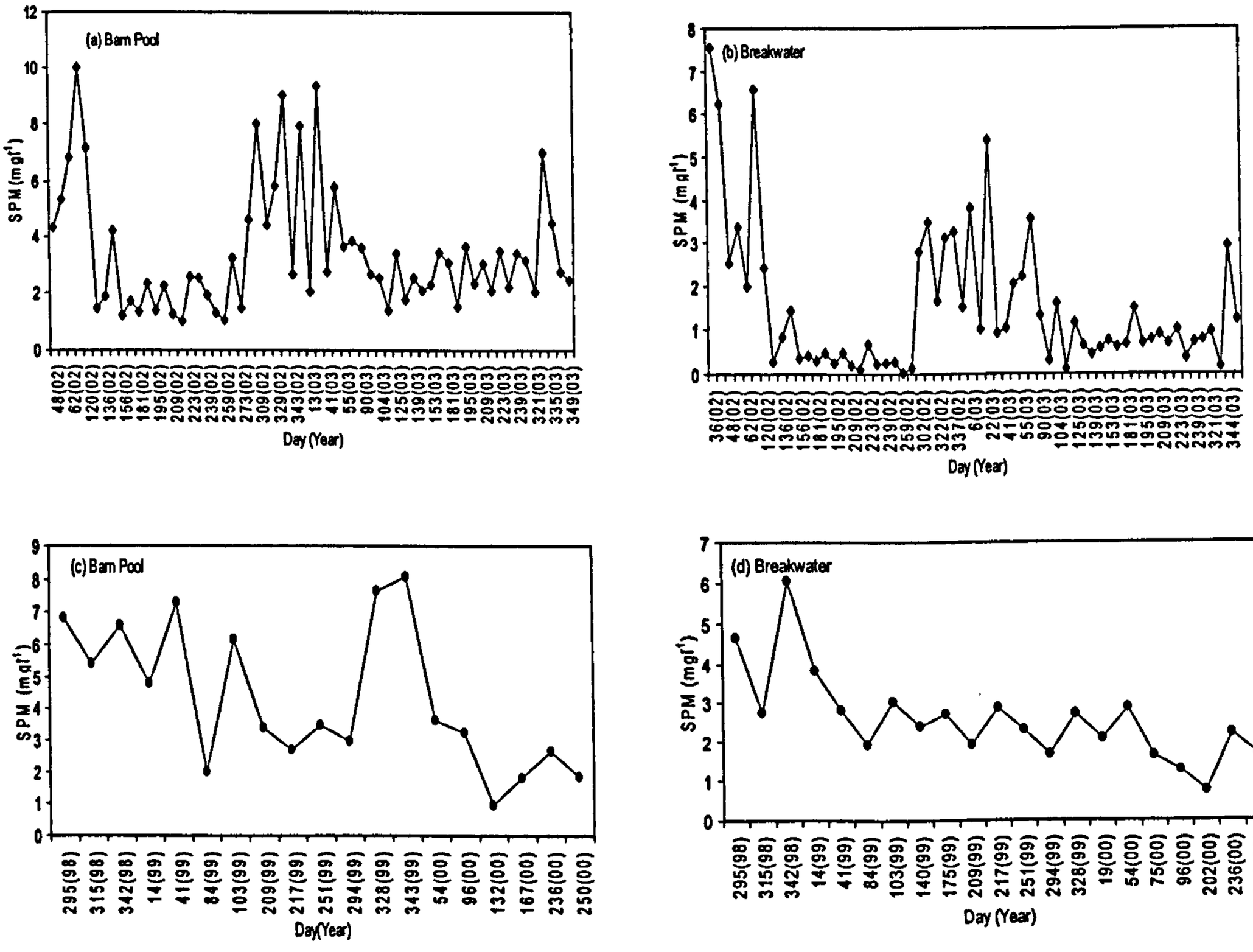

Figure 5.4: Variations of suspended particulate material in Plymouth Sound, from weekly data collection in 2002-2003 (UoP-PML) at (a) Barn Pool and (b) Breakwater and monthly sampling during 1998-2000 (COLORS) at (c) Barn Pool and (d) Breakwater.

Suspended particulate inorganic material (SPIM) and suspended particulate organic material (SPOM) concentration measurements were made following the procedure explained in Chapter 4, Section 4.2. Figure 5.5 presents the observed variations in SPIM and SPOM concentrations and their distributions in Breakwater and Barn Pool. In general 73% of the total SPM collected at these two sites was dominated by suspended particulate inorganic material. The range of SPM, SPIM and SPOM concentrations are given in Table 5.2.

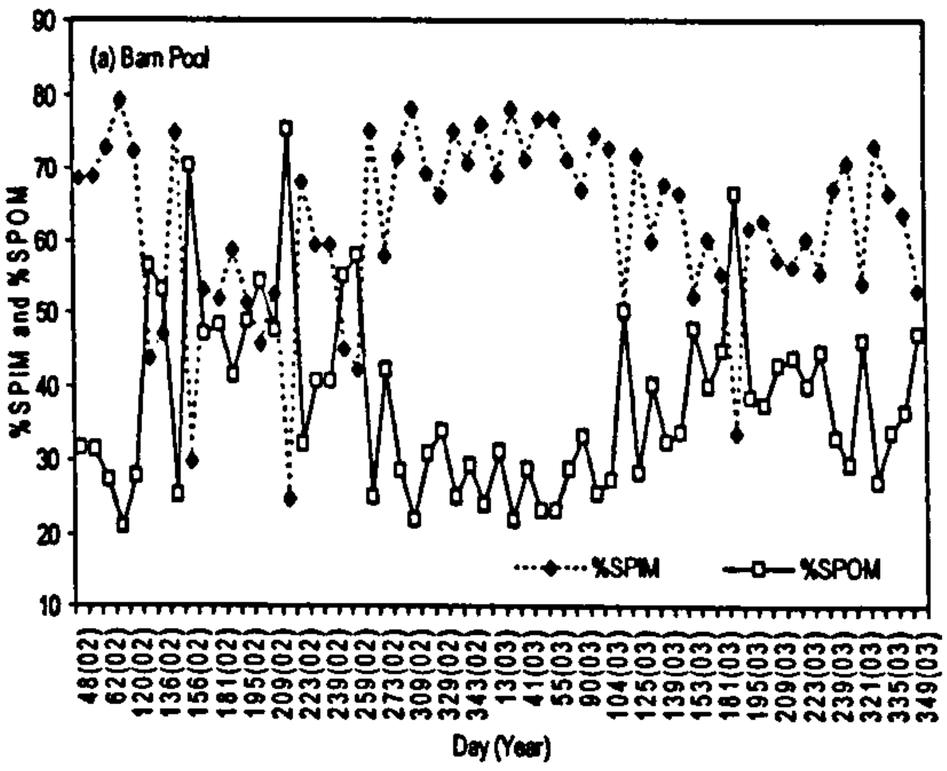

Figure 5.5: Percentage suspended sediment proportions in Plymouth Sound (2002-2003). Monthly and weekly data sampled at (a) Barn Pool and (b) Breakwater.

Table 5.2: SPM concentration at Breakwater and Barn Pool (1998-2003).

1998-2003	SPM (mg l^{-1})		SPIM (mg l^{-1})		SPOM (mg l^{-1})	
	Min	Max	Min	Max	Min	Max
Barn Pool	0.92	10.01	0.25	7.91	0.32	2.23
Breakwater	0.50	10.18	0.12	7.54	0.29	3.06

Both at Barn Pool and Breakwater, the percentage of SPIM was high in all seasons other than summer. A growth with time in the percentage of SPOM was observed at both the sites, which could be due to the availability of adequate sunlight during the summer season and hence phytoplankton growth. During autumn-winter, the rainfall and subsequent river flow inputs a large flux of minerogenic river sediments. However, there was still a small quantity of organic material, which could be organic humic solid or planktonic material.

5.1.4 Particle size distributions

Figure 5.6 presents the differential slope parameter (ξ) values calculated using Coulter counter Multisizer-II measurements made during 2002-2003. Calculation of ξ is explained in Section 5.2.1. The calculated slope range is presented in Table 5.3. A similar range of ξ in coastal waters was observed by Boss *et al.* (2001) in the Coastal Mixing and Optics experiment (1996-1997).

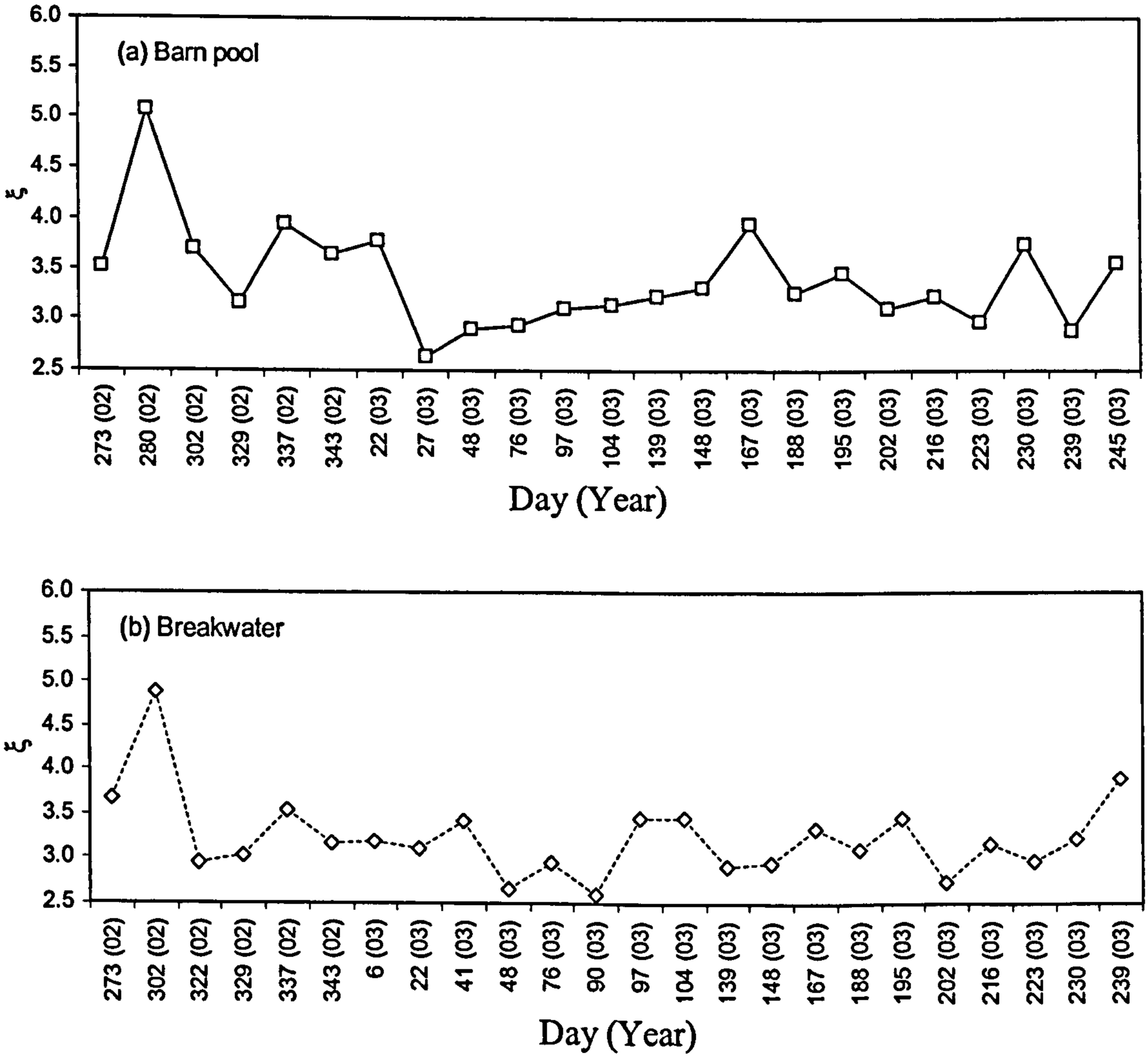

Figure 5.6: Particle differential slope measurements made at (a) Barn Pool and (b) Breakwater during 2002-03.

Table 5.3: Range of ξ values calculated using coulter counter measurements from Breakwater and Barn Pool.

2002-2003	ξ	
	Min	**Max**
Barn Pool	2.63	5.07
Breakwater	2.59	4.89

5.1.5 CDOM

Variations in absorption at 440 nm due to CDOM and the spectral slope of absorption from spectrophotometric measurements are presented in Figure 5.7 and Table 5.4. Samples were collected during 1998-2000 and 2003; all the samples and calculations were made following the protocols explained in Section 4.3. The absorption values at 440 nm are high in Barn Pool compared to Breakwater, which is probably the influence of river discharge into Plymouth Sound. The range of both the slope and $a_g(440)$ due to CDOM is similar to published observations of Kirk (1994).

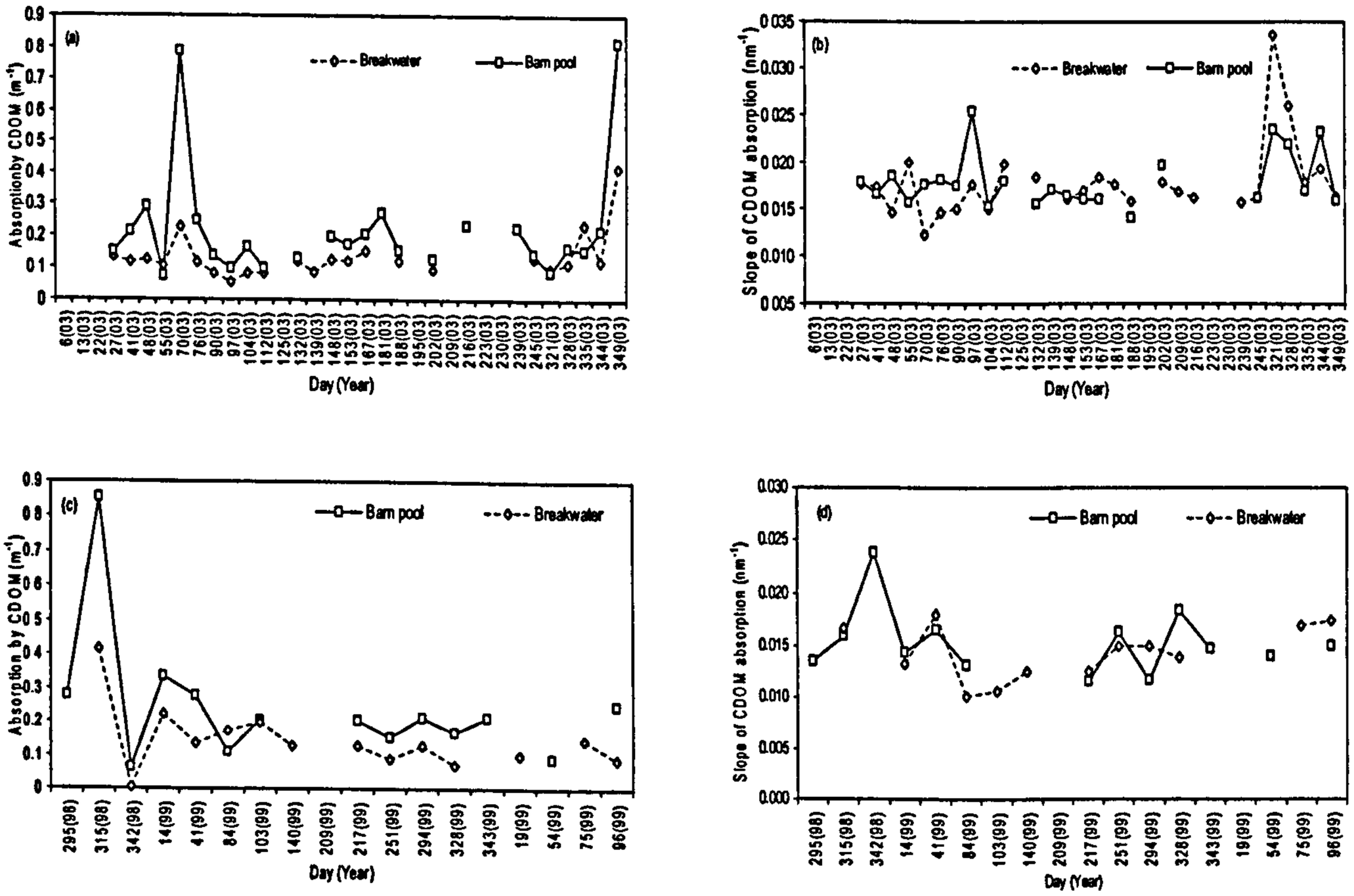

Figure 5.7: Variations of CDOM absorption and slope in Plymouth Sound. Data collected in at Breakwater and Barn Pool during (a) & (b) UoP-PML (2003) and (c) & (d) COLORS research (1998-2000).

Table 5.4: Range of $a_g(440)$ and slope of spectral absorption from spectrophotometric measurements made in 1998-2000 and 2003.

	$a_g(440)$ (m^{-1})		Slope(nm^{-1})	
1998-2000	**Min**	**Max**	**Min**	**Max**
Barn Pool	0.062	0.85	0.0115	0.0238
Breakwater	0.0023	0.41	0.0101	0.0180
2003				
Barn Pool	0.076	0.81	0.0121	0.0259
Breakwater	0.056	0.41	0.0141	0.0253

5.1.6 Mineralogical analysis of suspended particulate material

Suspended particulate material collected on the filter paper was analysed further for its composition, in particular the dominating inorganic component. This information was provided by Camborne School of Mines(CSM) and School of Earth Ocean and Environmental sciences (SEOES, UoP). X-ray diffraction analysis (XRD), Scanning Electron Microscopy (SEM) and Inductively Coupled Plasma Atomic Emission Spectrometer (ICPAES) were used towards this analysis.

The objective of these analyses was to identify the presence of dominating minerals. It is important to identify the minerals of the particulate material as they provide an estimation of relevant relative refractive index for Mie computations.

The XRD analysis provided information on abundance of minerals and elemental analysis by ICPAES confirmed their presence. A mean relative refractive index (*rri*) was calculated using the identified minerals (Table 5.5) along with organic matter (1.03-1.05), which approximates to 1.15. This value is used as the input bulk refractive index while computing scattering and backscattering following Mie computations.

Table 5.5: Minerals found in abundance from samples collected in Plymouth Sound

Mineral	**Chemical Formula**	***rri***
Quartz (Frame work silicate)	SiO_2	1.16
Muscovite (Sheet silicate)	$KAl_2(AlSi_3O10)(OH)_2$	1.19
Chlorite (Clay mineral)	$(Al,Mg,Fe)_3(OH)_2[(AlSi)_4O_{10}]Mg_3$ (OH)	1.21
Orthoclase (Feldspar)	$KAlSi_3O_8$	1.14
Albite (Feldspar)	$NAlSi_3O_8$	1.15
Kaolinite (Clay mineral)	$Al_4(OH)_8$ $[Si_4O_{10}]$	1.16

XRD analysis was cross checked with elemental analysis by ICPAES (Figure 5.8). The presence of Aluminum and Silicon confirm the abundance of alumino-silicates reported by XRD. ICPAES analysis was performed to identify the mineral forming elements.

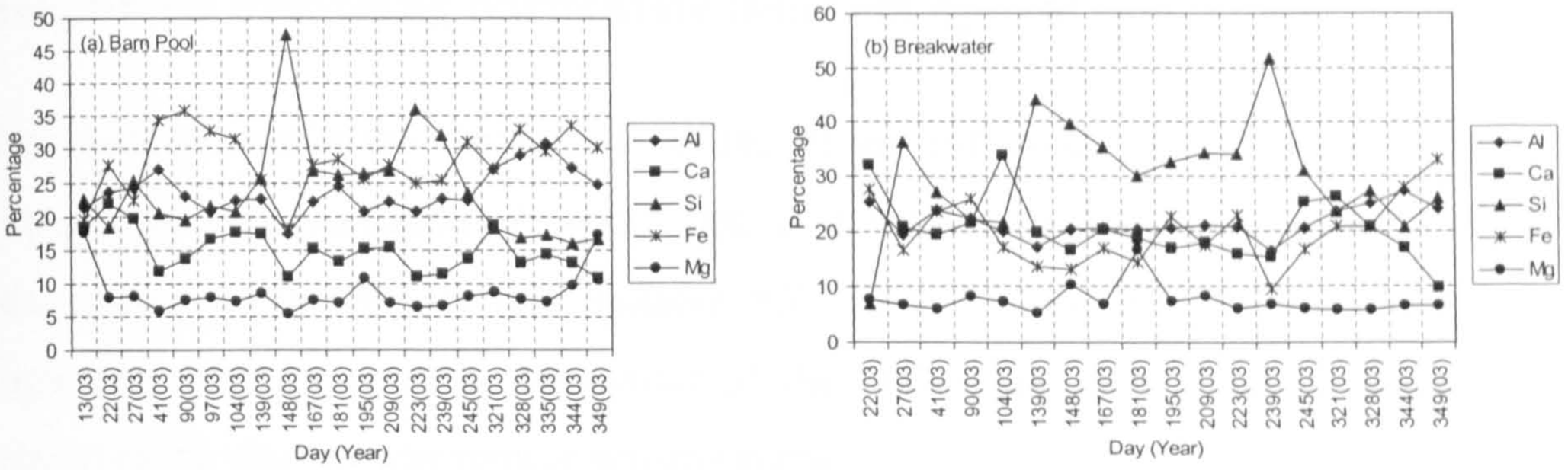

Figure 5.8: Elemental analysis results for SPM samples collected in Plymouth Sound for (a) Barn Pool and (b) Breakwater.

SEM pictures were analysed to visually observe the presence of inorganic material. Figure 5.9 presents some examples of the SEM pictures. These pictures highlight the presence of sheet silicates and aluminosilicates that have a cubical structure. Figure 5.9 (d) is a typical example of flocculation of sheet silicates and organic matter which dominates the SPM in coastal waters (Turner and Millward, 2002).

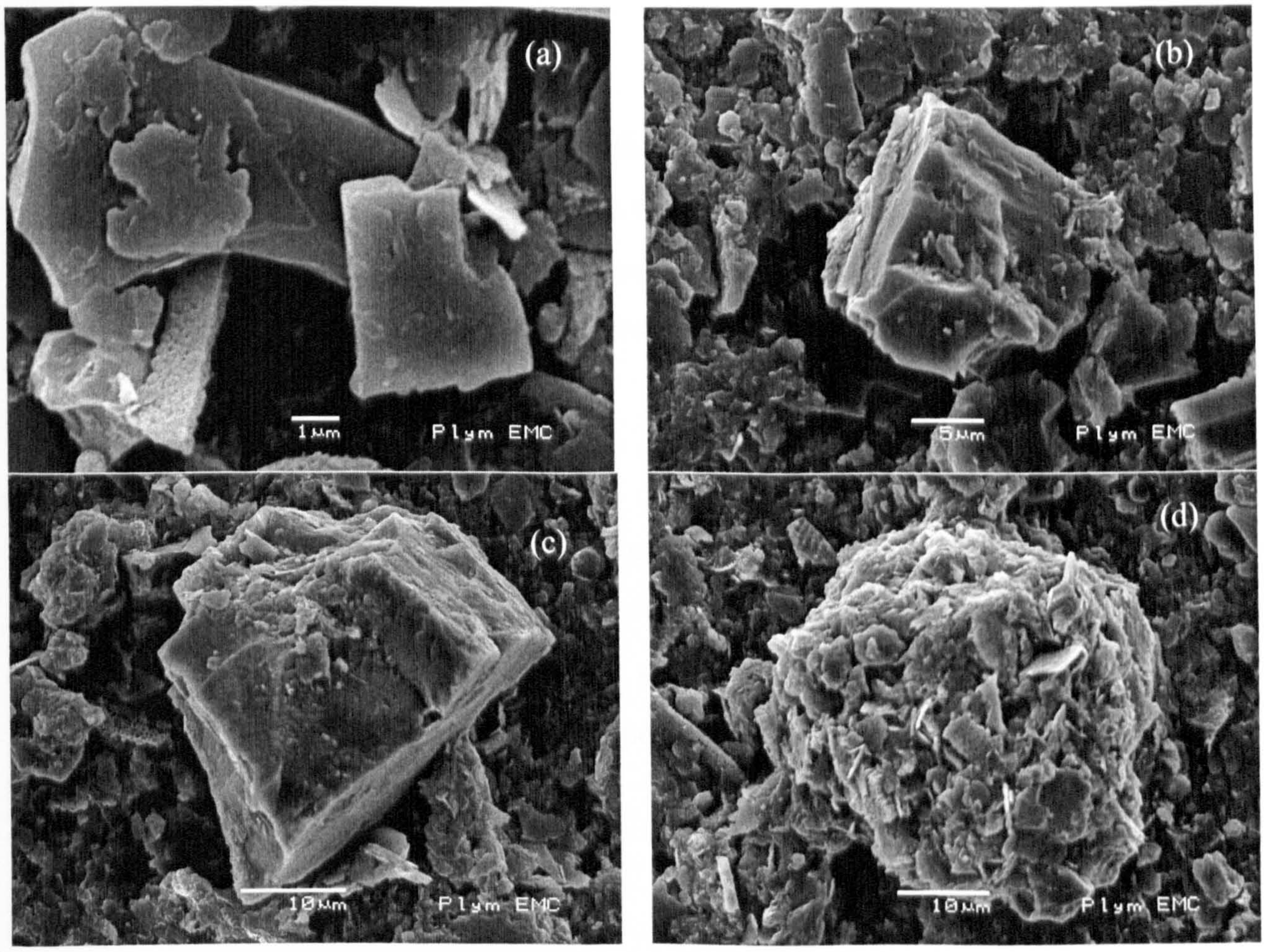

Figure 5.9: SEM pictures showing the presence of dominating inorganic material at different scales.

Section II: Modelling particulate inherent optical behaviour

This section details the theoretical outline of the particulate interaction behaviour, explanation and derivation of various optical constants and their usage to convert *in situ* optical measurements into suitable IOP values. Thus, derived information is exploited to understand the behaviour of the underwater optical environment and construct the above water remote sensing signal.

5.2.1 Particulate size distribution

Knowledge of particle size distributions is essential to understand the underwater optical environment. The size of the particle is an important controlling factor that defines the particle-photon interaction behaviour. The distribution of particle size is often described by a differential power law function (Boss *et al.*, 2001 and Mobley, 1994)

$$N(D) = N_0 \left(\frac{D}{D_0} \right)^{-\xi} \text{ [number per m}^4\text{]} \qquad \text{eq (5.1)}$$

where N(D) is the number of particles with diameters between D and D+dD divided by dD. D_0 is the reference diameter for which the number concentration is N_0 and ξ is the differential slope parameter. The applicability of such an approach has been shown in studies by Boss *et al.* (2001) and Twardowski *et al.* (2001).

5.2.2 Spectral attenuation slope

Following the predictions by the theory of anomalous dispersion (*van de* Hulst, 1981), it is possible to explain the compensations of absorption peaks to scattering inverse peaks. The resulting particulate attenuation spectra, $c_p(\lambda)$, decrease monotonically with increasing wavelength according to a hyperbolic model, given by equation 5.2

$$c_p(\lambda) = A_c \lambda^{-\gamma} \text{ [m}^{-1}\text{]} \qquad \text{eq(5.2)}$$

where γ is the hyperbolic slope of the spectrum and A_c is the corresponding amplitude.

Figure 5.10, is an example explaining the variation of spectral c_p in marine waters. Spectral attenuation values were collected using an ac-9 instrument and corrected for the dissolved matter absorption to derive particulate attenuation. The solid line represents the hyperbolic fit (equation 5.2) to the data. This fit provides a γ value of 0.538 with a good coefficient of determination (R^2=0.97). This behaviour is similar to the results presented by Boss *et. al.* (2001) based on Mie theory.

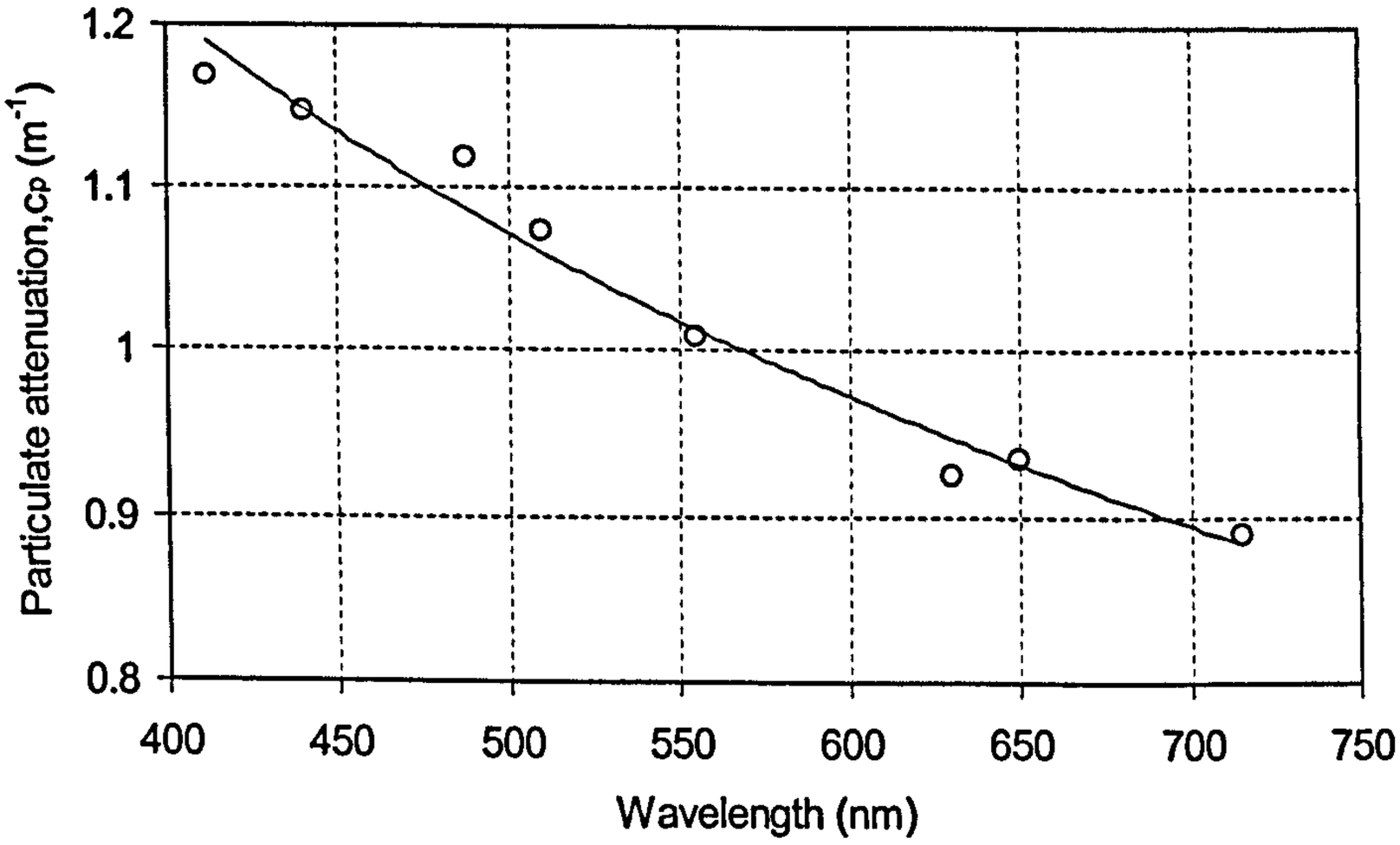

Figure 5.10: Spectral particulate attenuation distribution from data collected in Barnpool (09 March, 1999) using ac-9. This attenuation decreases with increasing wavelength.

5.2.3 Calculation of γ from ac-9 measurements

Attenuation measurements made by ac-9 have contributions from scattering due to particulate material (b_p) and absorption by particulate (a_p) and dissolved material (a_g). To derive c_p, a_g should be subtracted from the total attenuation (c_{pg}) measured by the ac-9. For this research, a_g values were obtained from spectrophotometric measurements.

Figures 5.11, was prepared from data collected from Barnpool (November 24, 1999), where solid lines represent the hyperbolic fit. The attenuation spectrum slope, γ_{pg} (-0.5971, R^2=0.9003) is presented in Figure 5.11a. In Figure 5.11b, γ (-0.4797, R^2=0.8789) represents the data fit, after subtracting a_g (Figure 5.11b). The γ_{pg} values are greater than γ because of the contribution of the CDOM shape to the shape of c_{pg}.

While CDOM makes only a small contribution to the magnitude of the total attenuation coefficient at any specific visible wavelength, it makes a significant contribution to its spectral shape as typically it has an exponentially decreasing absorption as a function of wavelength. For example, in Figure 5.11a and b the percentage difference between γ and γ_{pg} is 25.5%, which is a significant difference. It thus is important to determine CDOM absorption accurately and remove it from the total absorption.

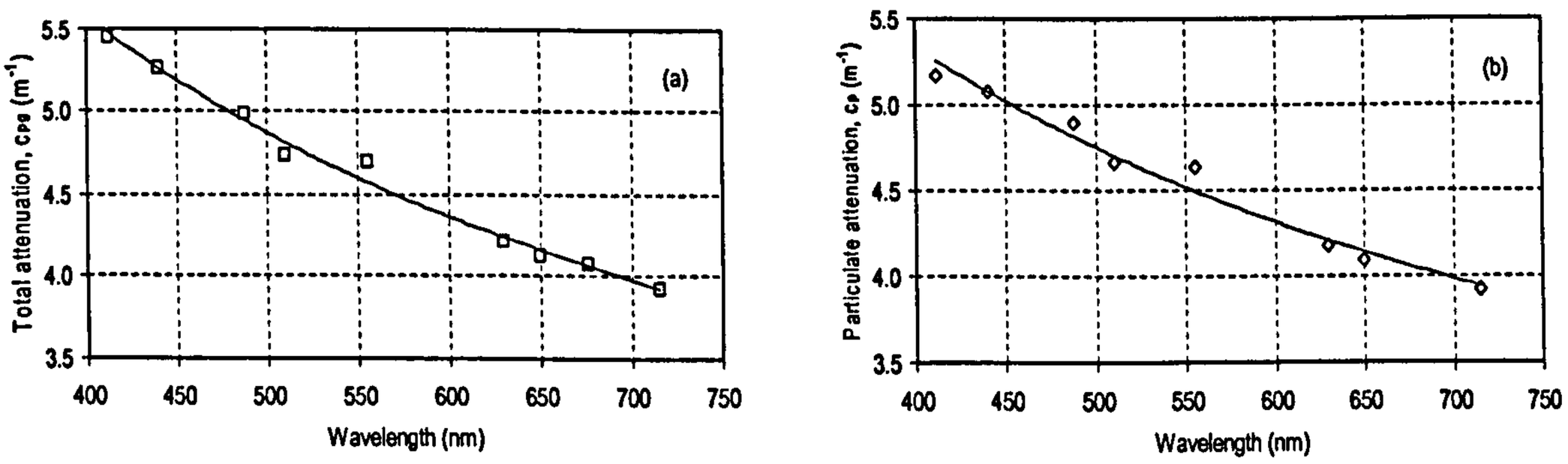

Figure 5.11 : (a) Total spectral attenuation (c_{pg}) as measured by the ac-9. c_{pg} has contributions from both particulate and dissolved material absorption. (b) Spectral particulate attenuation (c_p) measured by the ac-9. c_p is calculated by subtracting absorption due to dissolved matter (a_g).

In the data set used for this research, only a few a_g values (70 samples) were available synchronous with ac-9 measurements at different depths. This makes it difficult to make γ measurements for all the profiles acquired using ac-9, but these 70 samples were sufficient to understand the general relationship between γ and γ_{pg}. Figure 5.12 shows the relationship between these two slopes. The linear fit ($\gamma=0.7227*\gamma_{pg}+0.0186$, $R^2=0.8247$) provides a conversion from γ_{pg} to γ for all the ac-9 data.

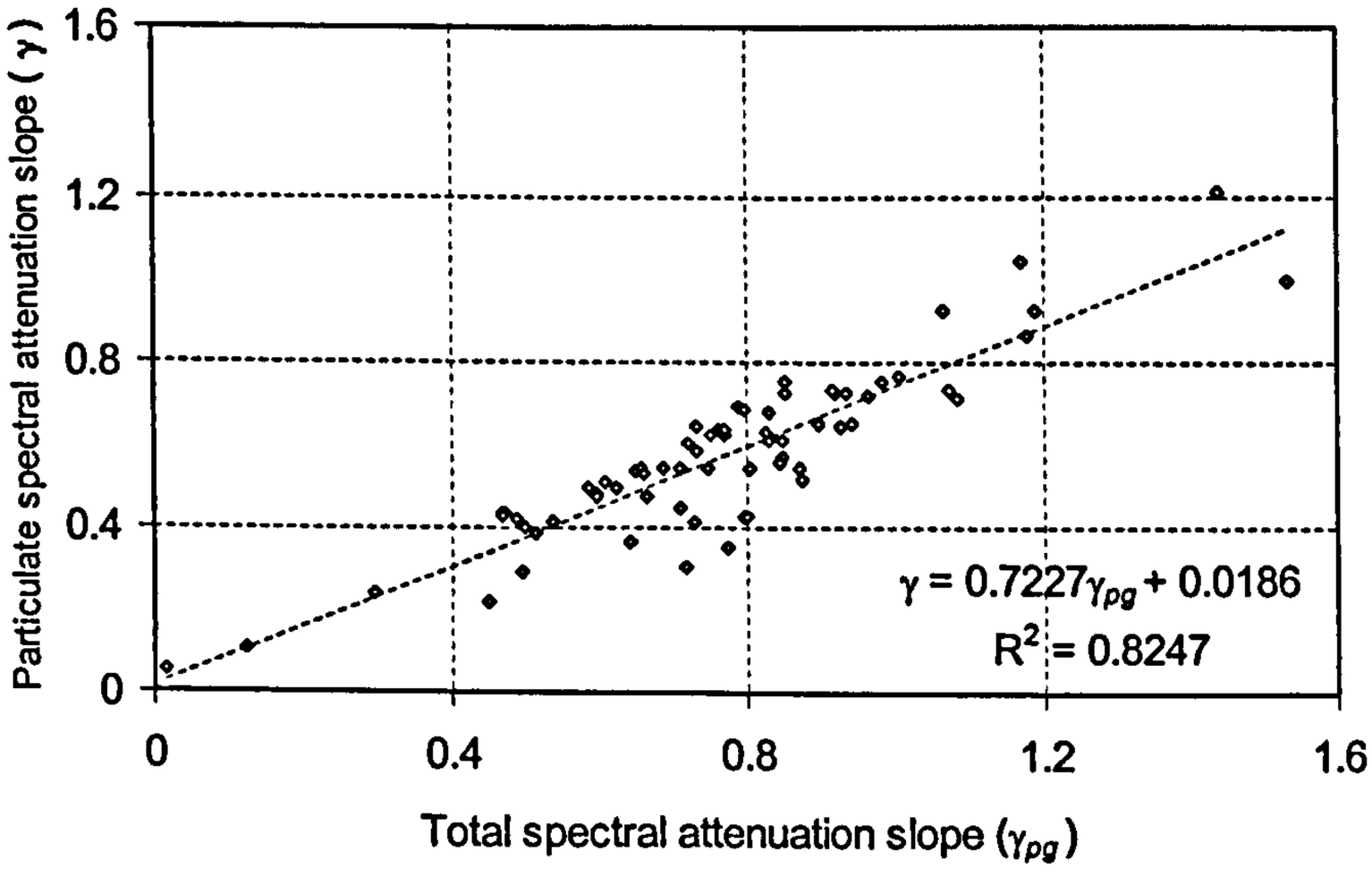

Figure 5.12: Relationship between total spectral attenuation slope (γ_{pg}) and particulate spectral attenuation slope (γ). The influence of CDOM absorption on spectral attenuation slope is clear. The dotted line is the linear fit between γ_{pg} and γ.

5.2.4 Link between ξ and γ

The relationship between shape parameter of c_p spectrum, γ and ξ is given as in equation 5.3. This has long been recognized and investigated theoretically (Volz 1954, Morel 1973, *van de* Hulst, 1981) and observed empirically (Kitchen *et al.* 1982, Boss *et al.* 2001, Twardowski *et al.* 2001).

$$\xi = \gamma + 3 \qquad \text{eq (5.3)}$$

A nonlinear fit to the dependence of ξ and γ was proposed by Boss *et al.* (2001), which is given in equation 5.4

$$\xi = \gamma + 3 - 0.5 * \exp(-6\gamma) \qquad \text{eq (5.4)}$$

The relationship (equation 5.4) was developed by employing Mie theory to compute the optical behaviour of particles, with two main assumptions: that the particles are homogeneous and spherical. Boss *et al.* (2001) assumed indices of refraction in the range of 1.02 and 1.20, and modelled populations with slopes $5 \leq \xi \leq 2.5$. They also explained the ineffectiveness of variations in the index of refraction and shape of

particles (maximum deviation of 0.2% [rms = 0.0002%] of the attenuation spectrum from the hyperbolic model) on the relationship proposed in equation 5.4.

Figure 5.13 shows the relationships as explained by equations 5.3 and 5.4. The particle size distribution measurements made in the study area show a slope value (ξ) in the range of 2.59 to 5.07 (Figure 5.6 and Table 5.3). Equation 5.4 can explain these values more accurately than equation 5.3. So, equation 5.4 was selected to convert the attenuation spectral slope derived from IOP measurements.

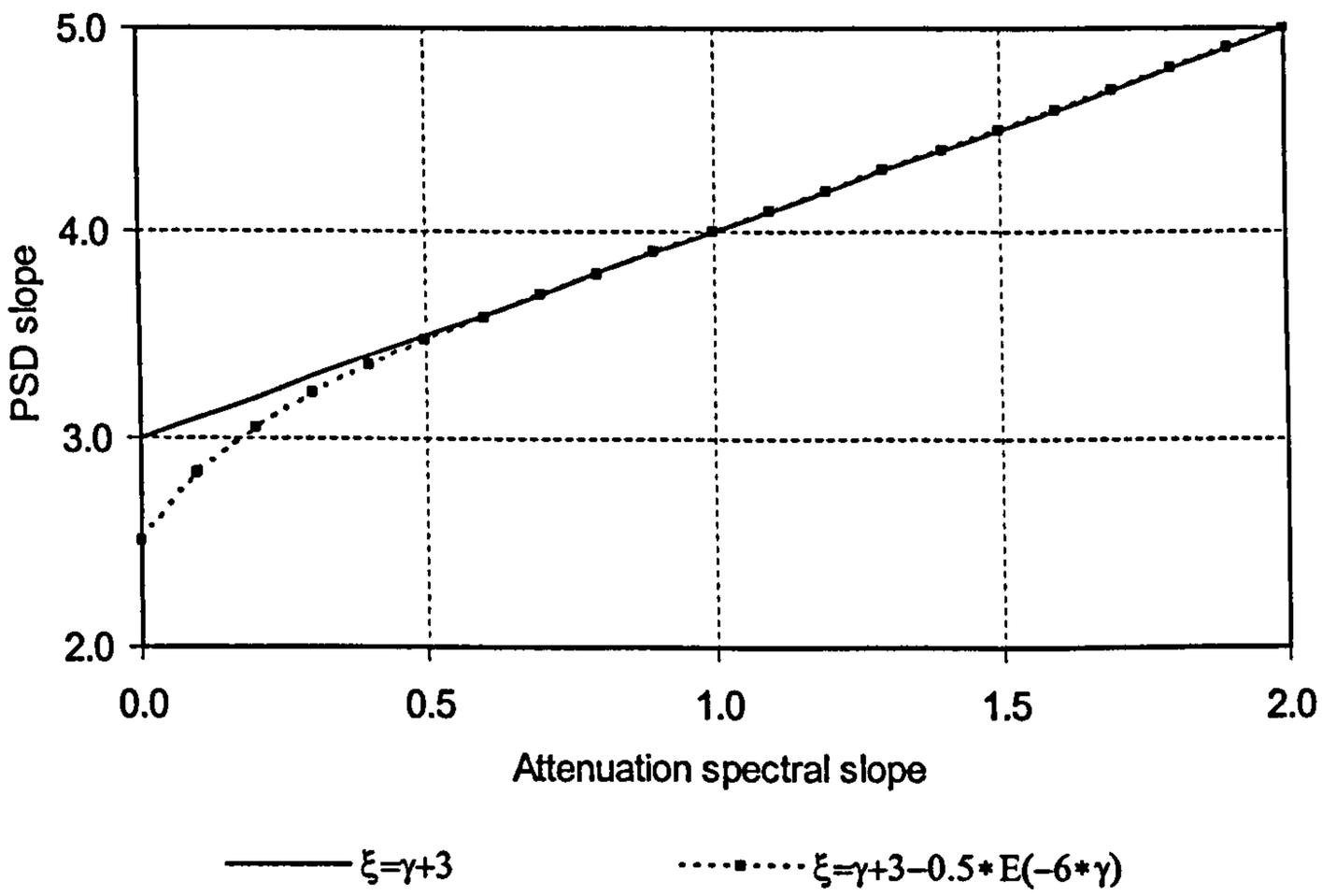

Figure 5.13: Particle size distribution slope (ξ) as a function of attenuation spectrum (γ).

5.2.5 Modelling particulate backscattering probability in coastal waters

Particulate backscattering probability or backscattering ratio is defined as the ratio of backscattering to total particulate scattering, which is given by equation 5.5.

$$\tilde{b_b} = \frac{b_b}{b} \qquad \text{eq (5.5)}$$

Backscattering and scattering for particulate material is given by equations 5.6 and 5.7 (Stramski *et al.* 1991).

$$b = \int_{D\min}^{D\max} Qb(\lambda, D, rri)\left(\frac{\pi * D^2}{4}\right)N(D)dD \qquad \text{eq (5.6)}$$

$$b_b = \int_{D\min}^{D\max} Qb_b(\lambda, D, rri)\left(\frac{\pi * D^2}{4}\right)N(D)dD \qquad \text{eq (5.7)}$$

where D is the diameter of the particle, N(D) is the number of particles as given in equation 5.1 and *rri* is the relative refractive index of the particulate material.

Q_b and Q_{bb} are the scattering and backscattering efficiencies that can be calculated using Mie computations (Bohren and Hauffman, 1983). These efficiency values are dependent on the size parameter of the particle, which is given as $\pi D/\lambda$ (Mobley, 1994), relative refractive index of the particulate material and the wavelength of the interacting photon. Respective cross section areas can be calculated (equation 3.6).

The efficiencies modelled for different particle diameters are presented in Figures 5.14 a and b. A relative refractive index of 1.05 and 1.15 was used for the computations of scattering and backscattering efficiencies of low-index organic and high-index minerogenic particles respectively. The minerogenic value was calculated from *in situ* climatological values (see Section 5.1.6). All the computations for efficiency values are computed using an IDL program (Flatau, 1996), which implements the approach developed by Bohren and Hauffman (1983) based on Mie

computations. Appendix 2 presents the IDL code developed for this research, which calculates the scattering and backscattering efficiencies and coefficients.

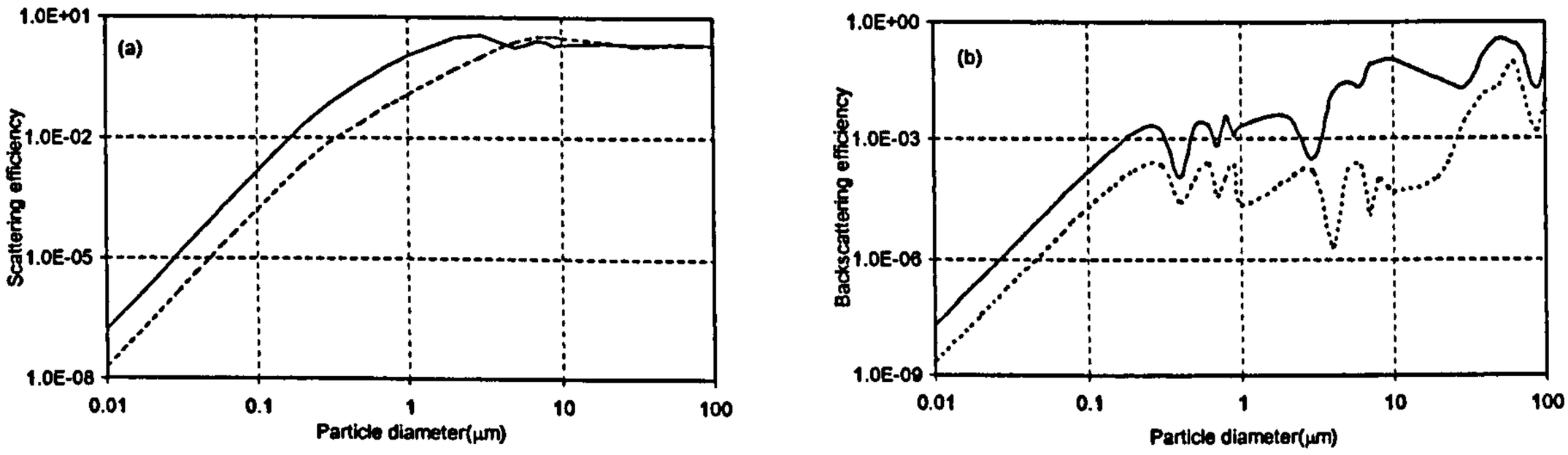

Figure 5.14 : A logarithmic plot of the efficiency factor for (a) scattering Q_b and (b) backscattering Q_{bb} at 555 nm wavelength as a function of particle diameter. The solid lines represent high-index particles and the dotted lines indicate low-index particles.

Coulter counter measurements were made in the study area during 2002-03 (Figure 5.6 and Table 5.3). Particles were measured using a 100 μm orifice that can measure particles as small as 2 μm. From these measurements ξ and N(D) were calculated (equation 5.1, Figure 5.6). N(D) values were extrapolated up to 0.01μm to include all possible small particles that may contribute to scattering. A relative refractive index of 1.15 was chosen as the bulk refractive index as the study area was mostly dominated mainly by a high percentage of minerogenic particulate concentrations (Figure 5.5 and Table 5.2). Finally, following equations 5.6 and 5.7 the product of scattering and backscattering cross-sections and particle numbers were integrated over the range of available particles [D minimum(0.01 μm) – D maximum (as measured by coulter counter)] to derive the total scattering and backscattering coefficients.

5.2.6 Relationship between ξ and $\tilde{b}_b$

From all the particle size measurements made, the differential slope parameter and backscattering to scattering ratio were calculated following equations 5.1 and 5.5. Equations 5.8, 5.9, 5.10 and 5.11 represent the dotted lines in Figure 5.15 which are the best fit between ξ and $\tilde{b}_b(\lambda)$. These results were developed using *in situ* particle size measurements and they are similar to the results presented by Twardowski *et al.*(2001) based on theoretical modelling and particle distributions.

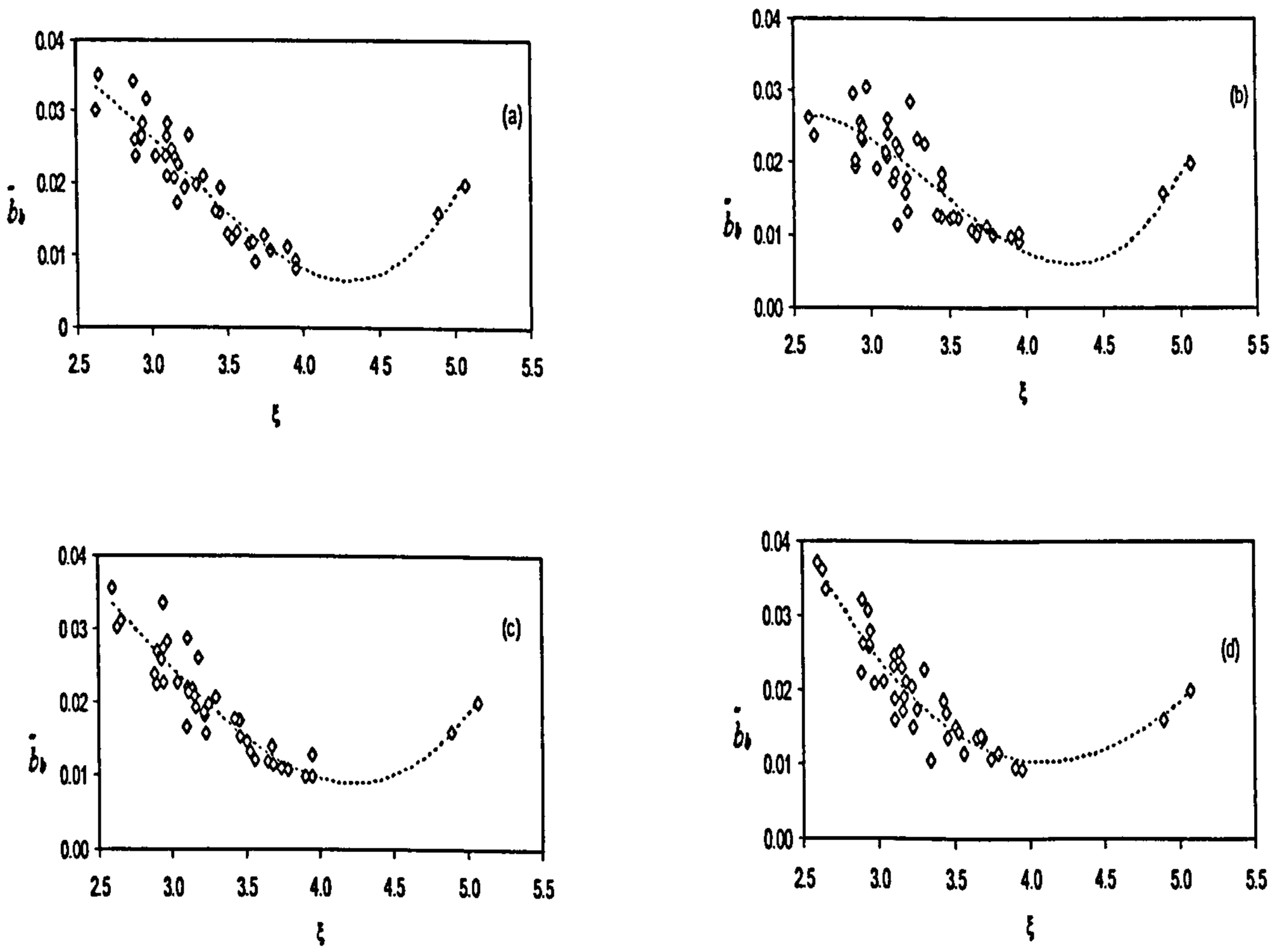

Figure 5.15: Mie theory results of the backscattering ratio as a function of the hyperbolic slope of the differential particle size distribution. Computations are represented for (a) blue (440 nm), (b) blue (488 nm), (c) green (555 nm) and (d) red (650 nm).

$$\tilde{b}_b(440) = 0.0059\xi^3 - 0.0561\xi^2 + 0.1578\xi - 0.1002 \quad (R^2 = 0.8611) \qquad \text{eq (5.8)}$$

$$\tilde{b}_b(488) = 0.0075\xi^3 - 0.0766\xi^2 + 0.2446\xi - 0.2231 \quad (R^2 = 0.6629) \qquad \text{eq (5.9)}$$

$$\tilde{b}_b(555) = 0.0028\xi^3 - 0.0215\xi^2 + 0.0331\xi + 0.0438 \quad (R^2 = 0.8459) \qquad \text{eq (5.10)}$$

$$\tilde{b}_b(650) = -0.0008\xi^3 + 0.0206\xi^2 - 0.1279\xi + 0.2441 \quad (R^2 = 0.8505) \qquad \text{eq (5.11)}$$

The shape of the relationship between ξ and $\tilde{b}_b$ is similar for different wavelengths (Figure 5.15). The amplitude of the backscattering ratio varies only by a small percentage over blue, green and red regions (Figure 5.16). The spectral behaviour of backscattering ratio realised in this research is similar to that previously published (Whitlock *et al.* 1981 and Risović, 2002).

To be accurate, the small percentage differences in amplitude were included by using wavelength specific equations and applying them only to adjacent ac-9 wavelength channels (such as $\tilde{b}_b(440)$ for both 412 and 440 nm, $\tilde{b}_b(488)$ for both 488 and 510, $\tilde{b}_b(650)$ for 630, 650, 676, 715 nm channels).

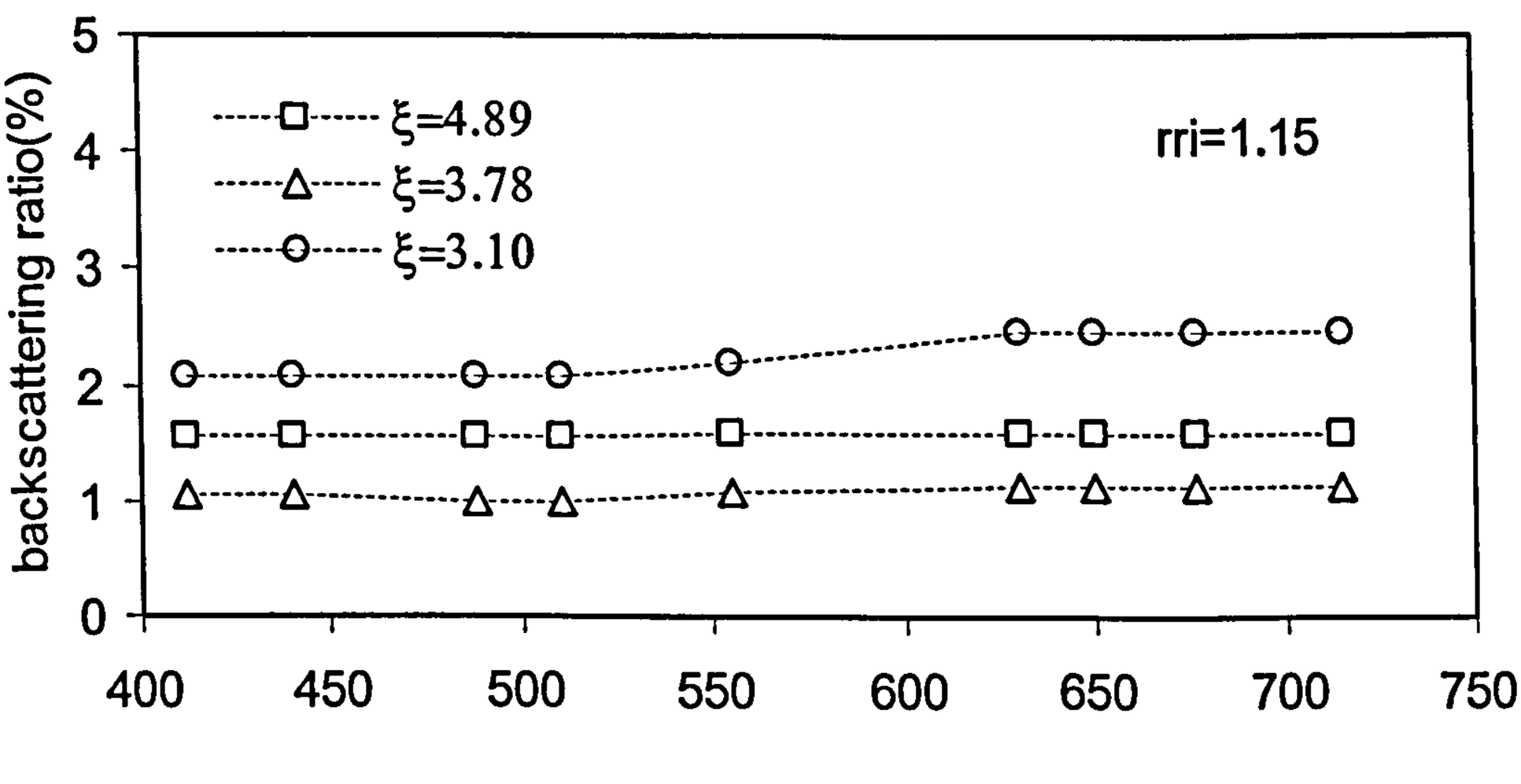

Figure 5.16: The particulate backscattering ratio as a function of wavelength for particles with a Junge-type size distribution and a diameter range $0.01 \leq D \leq$ D[maximum] (observed).

Equation 5.12 was used to transform ac-9 measured scattering to backscattering

$b_b(\lambda) = \tilde{b}_b(\lambda) * b(\lambda)$ eq (5.12)

Finally, the procedure for calculating backscattering from ac-9 measurements can be summarised as shown in Figure 5.17

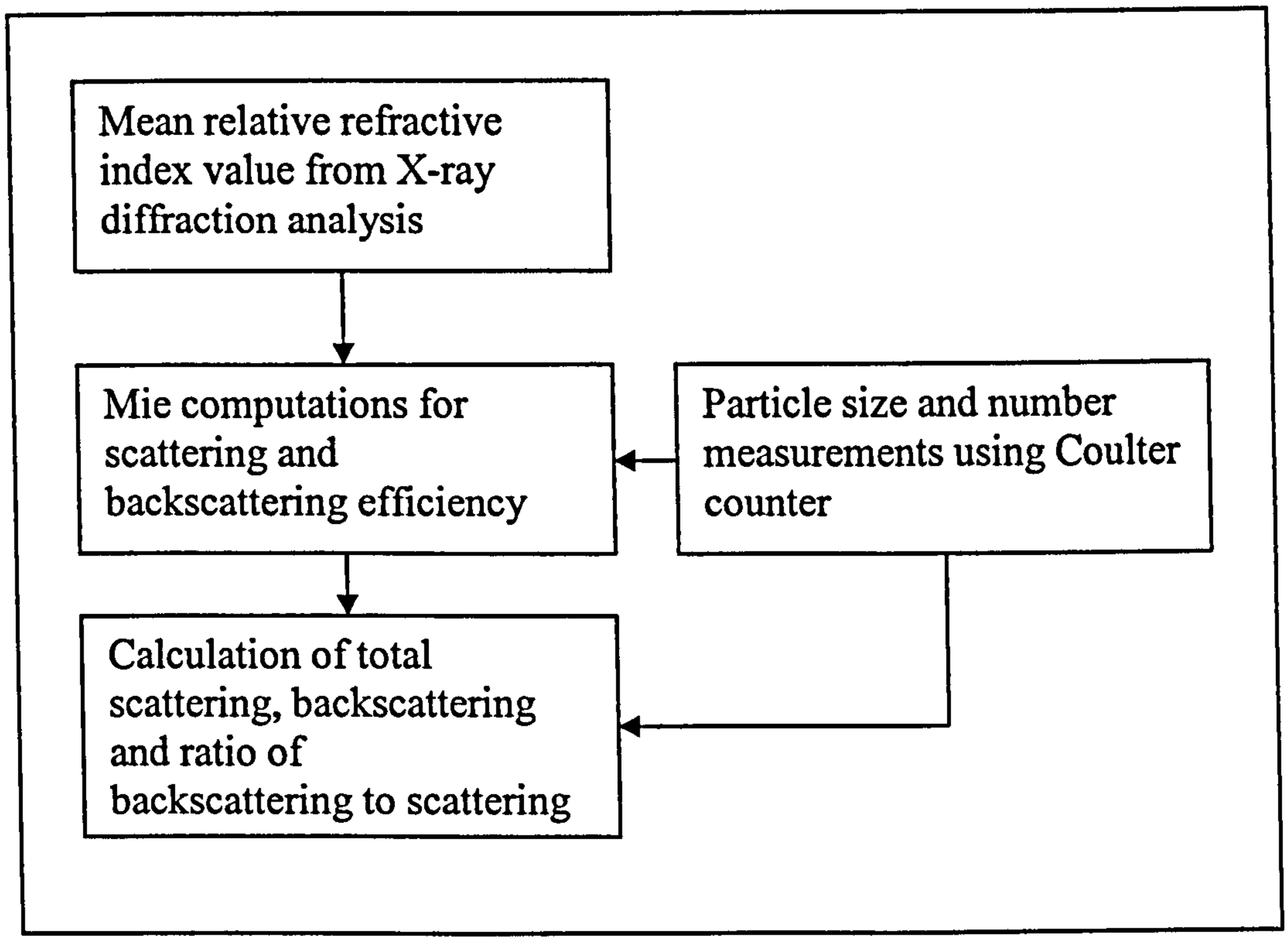

Figure 5.17: Schematic procedure explaining the calculation of probability of backscattering (backscattering to scattering ratio).

5.2.7 Comparison of Petzold and Modelled b_b/b values

An alternative approach to convert ac-9 values to backscattering is to use the constant values proposed by Petzold (1972). Four probability values are suggested for pure seawater, clear ocean, coastal ocean and turbid water. For the range of scattering values measured in Plymouth Sound a probability value of 0.020 is suggested. Figure 5.18a presents backscattering values at 510 nm, calculated using Petzold (Diamonds) and Mie (circles) backscattering probability constants. These results show a positive slope in both the cases. But the backscattering values calculated using Mie constant seem to represent a more realistic distribution. This scatter distribution is likely to be the result of different particle size distributions and concentrations.

Further, Figure 5.18b presents a comparison of results from both the approaches. From these results it appears that backscattering values calculated using Petzolds constant estimate a lower value when compared to values generated using Mie constant. This would be reflected in the reflectance calculations if implemented in the model. As the results from the Mie model appear to be describing a realistic distribution, it was decided to implement this approach in the forward model. But still,

it is clearly acknowledged that there is a need to validate this approach with *in situ* backscattering measurements in future.

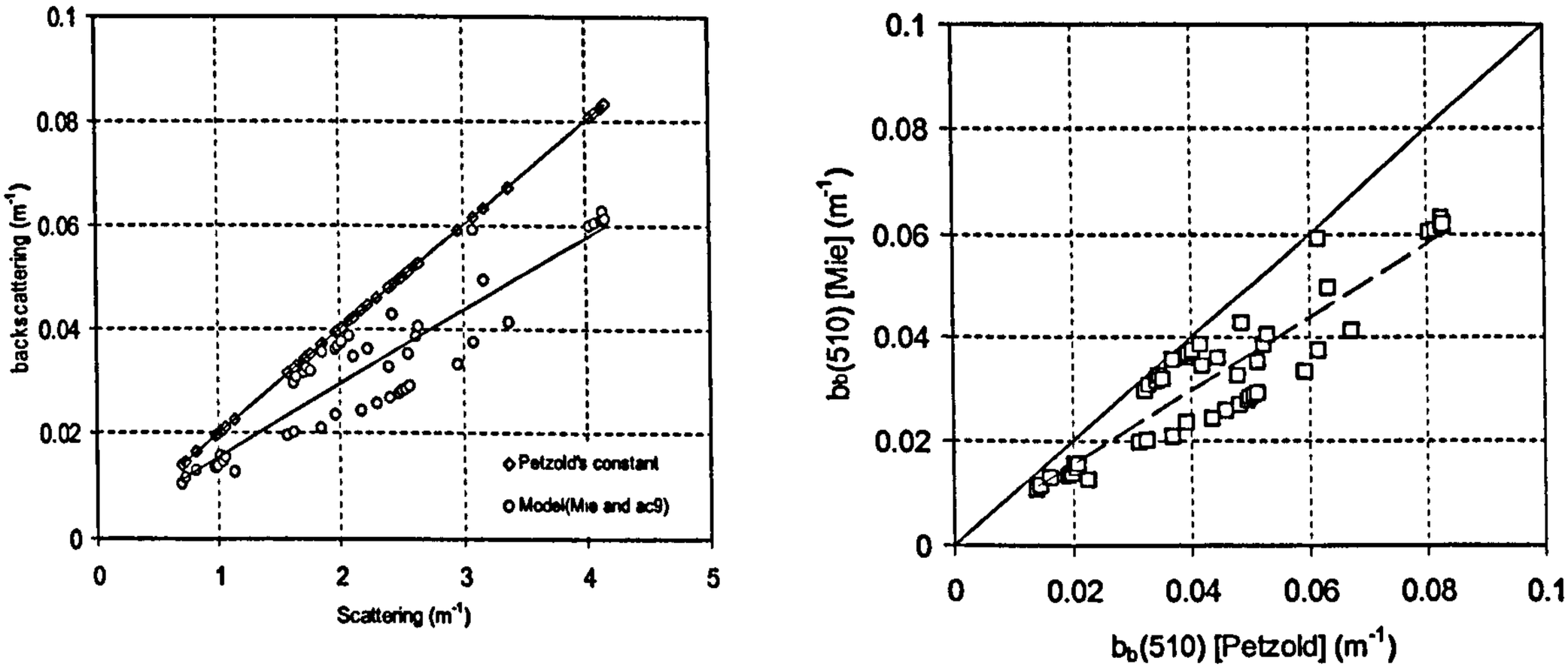

Figure 5.18: (a) Backscattering values calculated using Petzold's constant and Mie modelled probability. (b) Scatter plot of backscattering values at 510 nm.

5.2.8 Calculation of reflectance

The relationship between irradiance reflectance and IOPs underwater is presented in numerous publications (Morel and Prieur 1977, Gordon 1988, Kirk, 1994 and Mobley, 1994). By definition the underwater irradiance reflectance is the ratio of upwelling irradiance to downwelling irradiance and is given as

$$R=E_u/E_d \qquad \text{eq (5.13)}$$

This irradiance reflectance is related to IOPs as

$$R = f * \frac{b_b}{a + b_b} \qquad \text{eq (5.14)}$$

where a is the total absorption, b_b is the backscattering of the water body and *f* is a function of the ratio of molecular backscattering to total backscattering and the cosine of the sun zenith angle (Morel and Gentili, 1991).

Equation 5.14 can be re written as

$$\frac{Eu}{Ed} = f * \frac{b_b}{a + b_b} \qquad \text{eq (5.15)}$$

$$\frac{Lu}{Ed} = \frac{f}{Q} * \frac{b_b}{a + b_b} \qquad \text{eq (5.16)}$$

The quantity on both sides of equation 5.16 is called radiance reflectance. The *f*/Q values used in equation 5.16 were derived from look-up tables developed using Hydrolight©. These look-up tables were developed using the approach published in Moore *et al.* (1999). Absorption and scattering from ac-9 measurements, sun zenith angle θ_s, view angle θ_v and azimuth difference $\Delta\phi$ are inputs for the lookup table search. A majority of the optical data collection was in overcast sky conditions, so a sun zenith angle of 45° is used along with θ_v=0° and $\Delta\phi$=0° as input for the lookup table search.

5.2.9 Radiance reflectance

In equation 5.16 the quantity on the left hand side can be calculated using apparent optical measurements made by Satlantic SPMR (Satlantic Profiling Multichannel Radiometer) optical heads (Figure 4.5). The product on the right hand side is calculated using ac-9 measurements. Figure 5.19 gives examples of radiance reflectance values calculated using ac-9 and SPMR measurements.

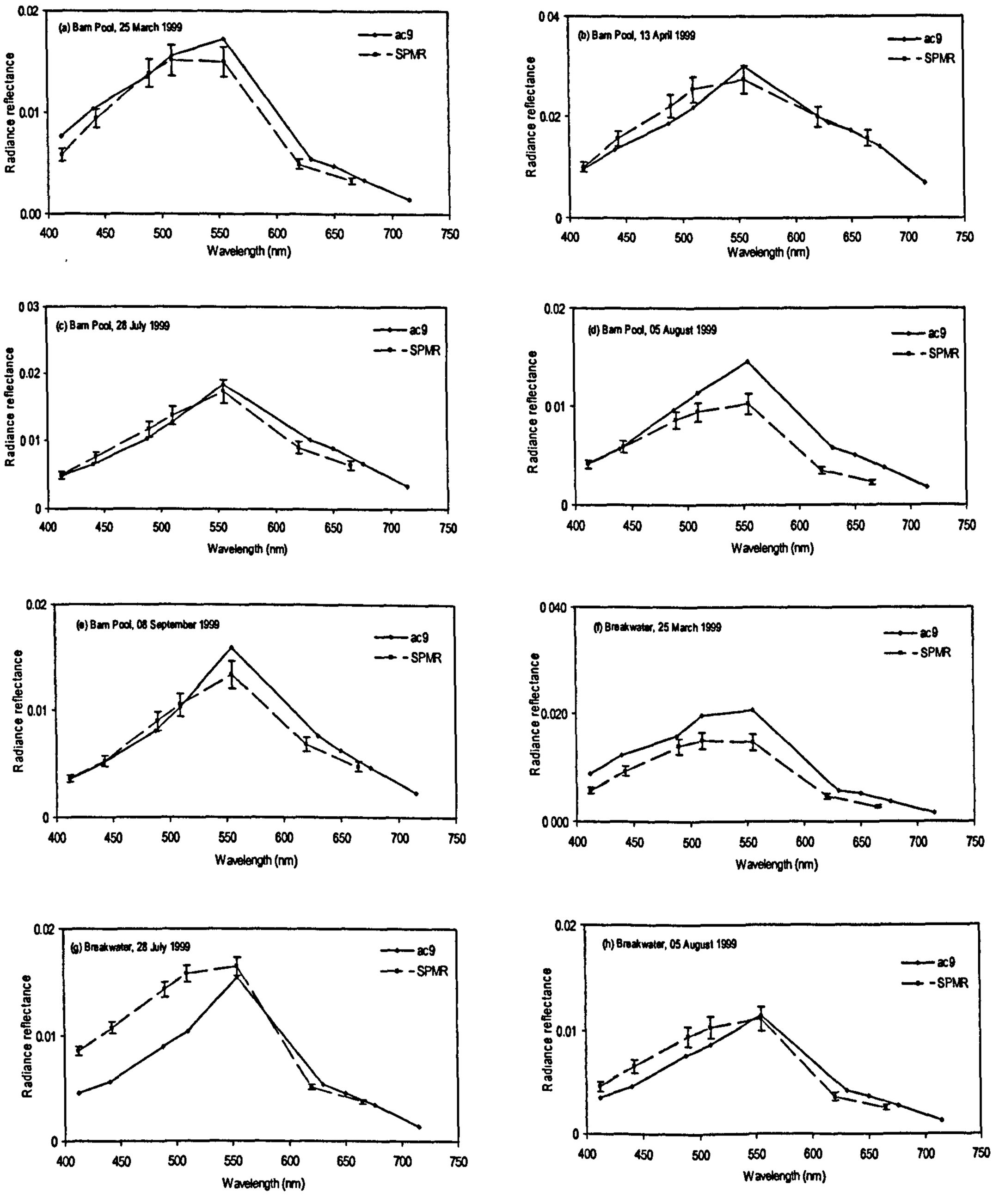

Figure 5.19: Example radiance reflectance calculated using ac-9 and SPMR measurements. A total of 53 spectral samples were compared in the coastal waters of Plymouth. Plots (a) to (e) are calculations for Barn Pool and (f) to (h) represent calculations for Breakwater in different months.

In Figure 5.19, the dashed lines represent the radiance reflectance calculated using SPMR measurements. The solid lines are plotted using ac-9 reflectance values as given on the right hand side of equation 5.16. The accuracy of radiance reflectance derived from SPMR data is expected to be 10% or less (Fargion and Mueller, 2000). Instrument shelf shading and radiometric accuracy are the major contributors towards this uncertainty. In Figure 5.19 an error bar of 10% is used to indicate the accuracy of radiance reflectance values made using SPMR.

A total of 53 spectral samples of SPMR and ac-9 are compared at radiance reflectance level. The spectral plots in Figure 5.19 are average values of binned data over the first 1 metre depth. Binned data is preferred over extrapolation to the subsurface as inaccuracies are minimized with the averaging over the bin. The comparison produces a good reproduction of the spectral shape within the discussed error limitations. The ac-9 derived radiance reflectance could exhibit the same shape as SPMR which is expected in coastal waters with high CDOM and SPIM content (Pierson and Strömbeck, 2001).

Figure 5.20 is a scatter plot of radiance reflectance calculated using measurements of ac-9 and SPMR. The scatter plot presents a comparison of 150 samples in the blue and green channels of the SPMR and ac-9 (412:412, 440:443, 488:490, 510:510, 555:555). These channels are presented as they are the common bands in these two sensors.

Even though the measurements do not strictly follow the 1:1 line, they are scattered around the 1:1 line. Measurements are plotted for the top three depths and they seem to satisfy equation 5.16 at all three depths, which suggests the applicability of equation 5.16 below the surface. Non alignment of data points along the 1:1 line could be due to the difference in the channel widths and central wavelengths of the two sensors. There will also be a significant contribution from errors as previously discussed for Figure 5.19.

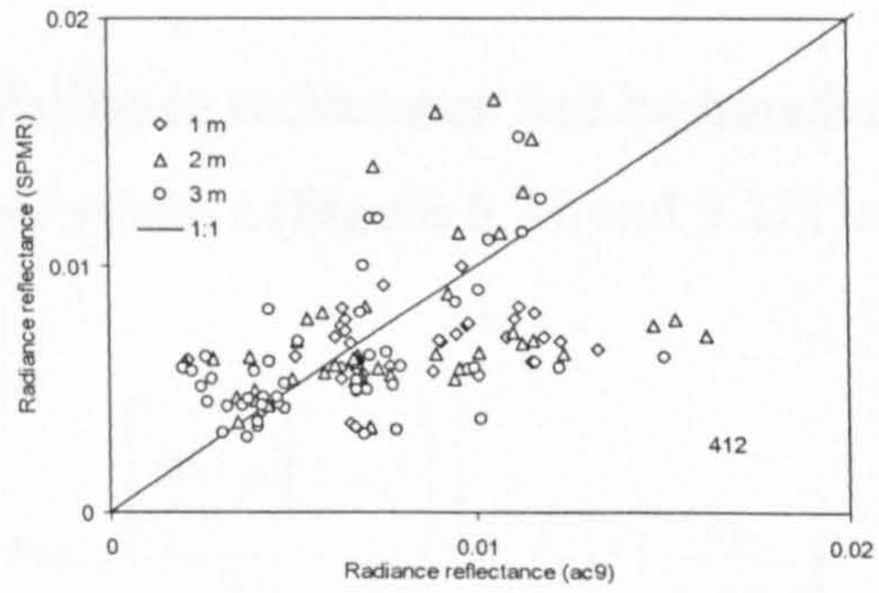

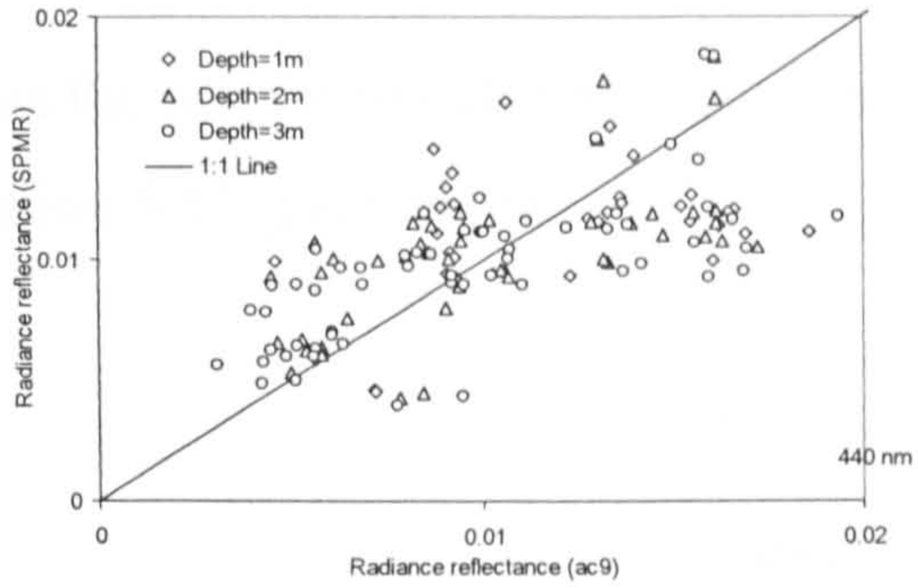

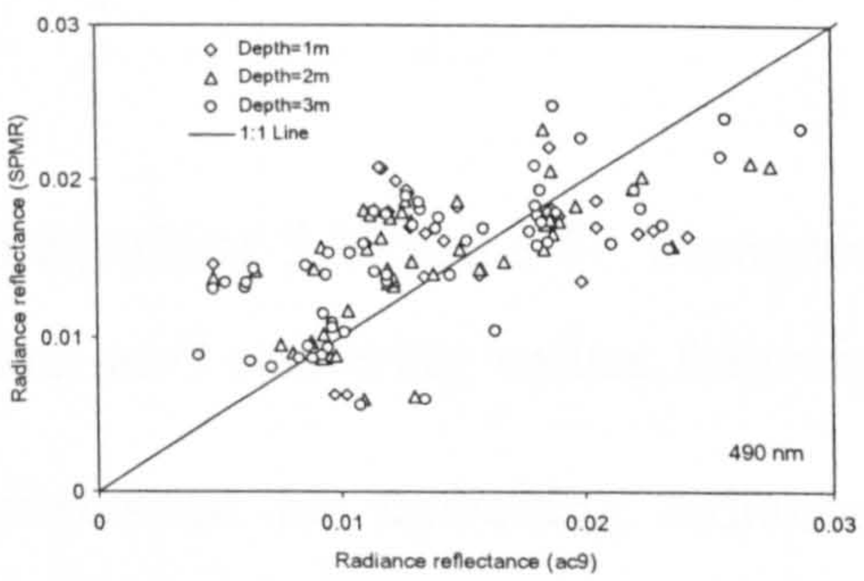

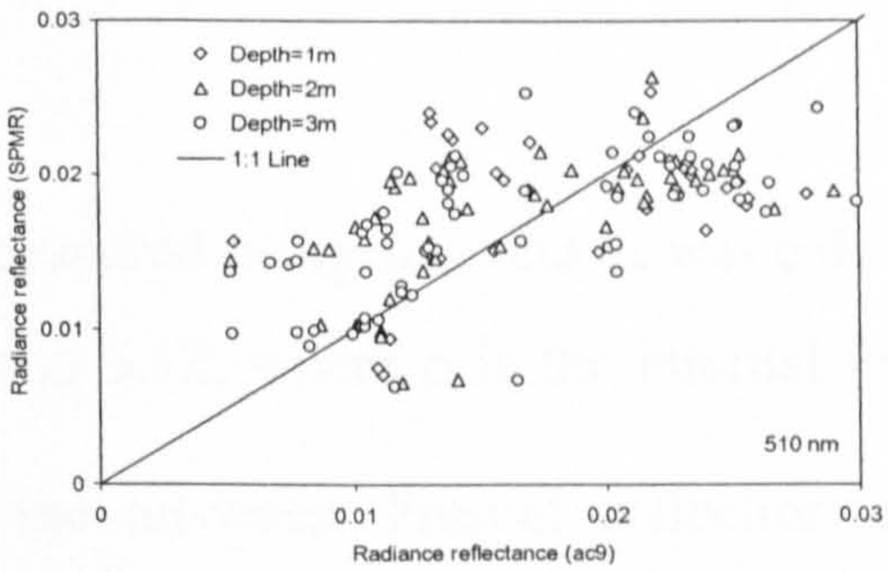

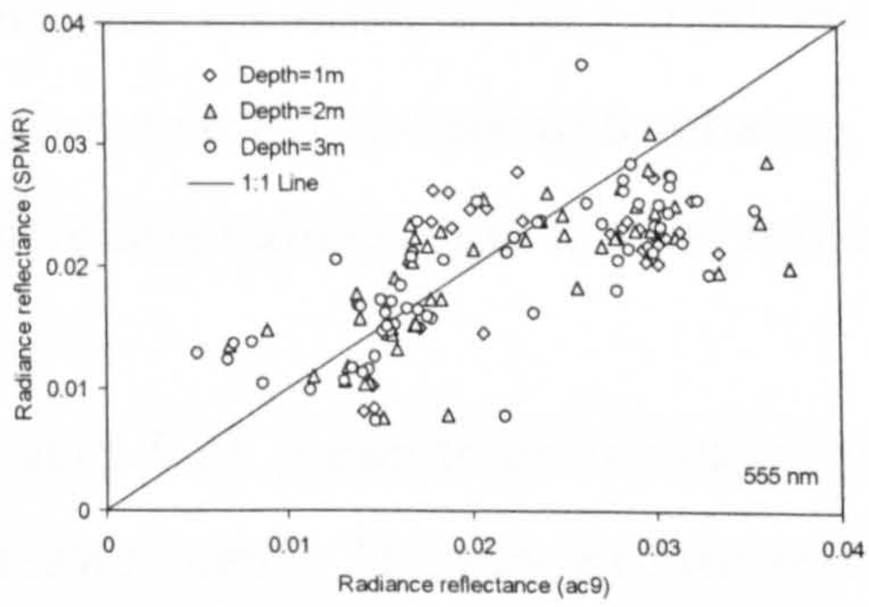

Figure 5.20: Spectral scatter plots of radiance reflectance. Depth averaged binned date was used from both ac-9 and SPMR. Comparisons made at matching channels (412:412, 440:443, 488:490, 510:510, 555:555) of ac-9 and SPMR. A total number of 150 samples are used in the scatter plot comparisons.

5.2.10 Remote sensing reflectance

Radiance reflectance can be transferred across the surface to calculate remote sensing reflectance (Figure 5.21 and 5.22) using equation 5.17 given below

$$Rrs = \left[\frac{(1-\rho)\left(1-\bar{\rho}\right)}{n^2(1-rR)}\right] * \left[\frac{f}{Q}\right] * \left[\frac{b_b}{a+b_b}\right] \qquad \text{eq (5.17)}$$

In equations 5.16 and 5.17, absorption was measured using ac-9 and b_b was calculated from ac-9 scattering values following equation 5.12, where ρ is the internal Fresnel reflectance for upwelling radiance $\bar{\rho}$ is the air-water Fresnel reflection at the interface for downwelling irradiance above the surface, $\bar{r}$ is the water-air Fresnel reflectance for upwelling irradiance, the Q factor is a ratio of upwelling irradiance to upwelling radiance and n is the refractive index of the water.

Figure 5.21 presents examples of remote sensing reflectance calculations from ac-9 measurements. The shape of the reflectance curve reflects SPM concentrations both in Barn Pool and Breakwater and in different seasons. The magnitude of the reflectance is influenced by varying SPM and CDOM concentrations (Figure 5.4 and 5.7).

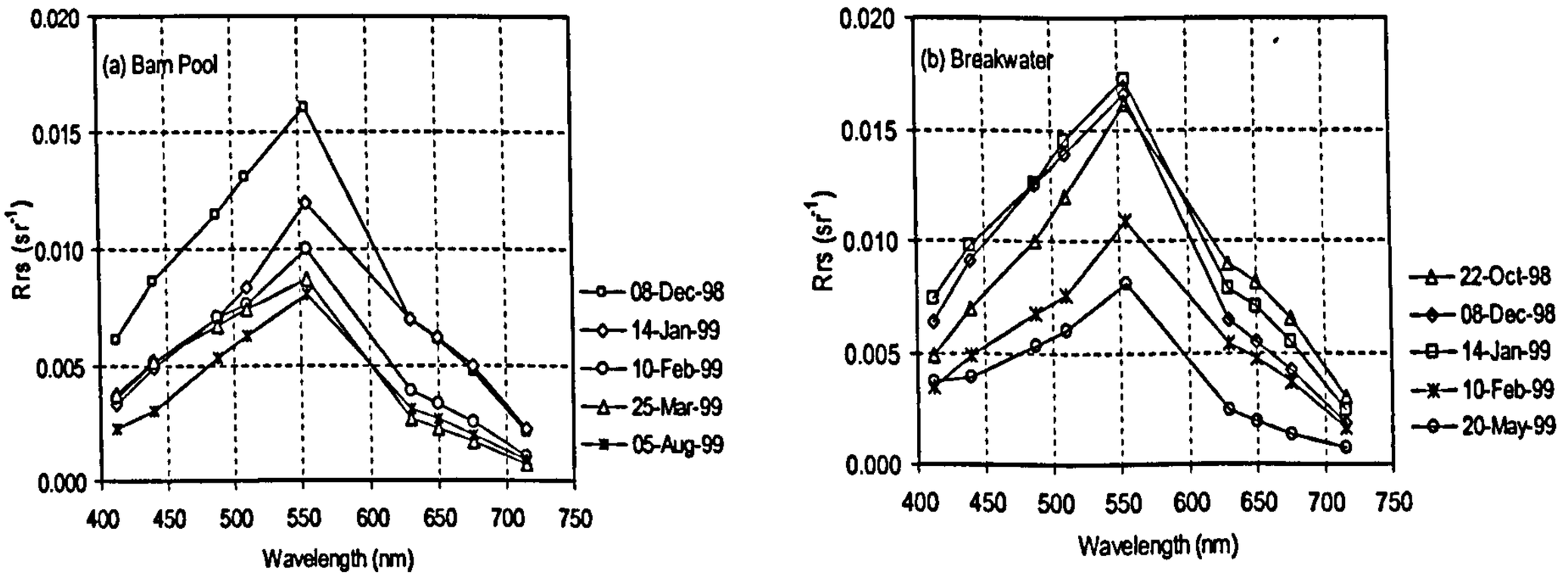

Figure 5.21 : Spectral remote sensing reflectance plots from (a) Barn Pool and (b) Breakwater.

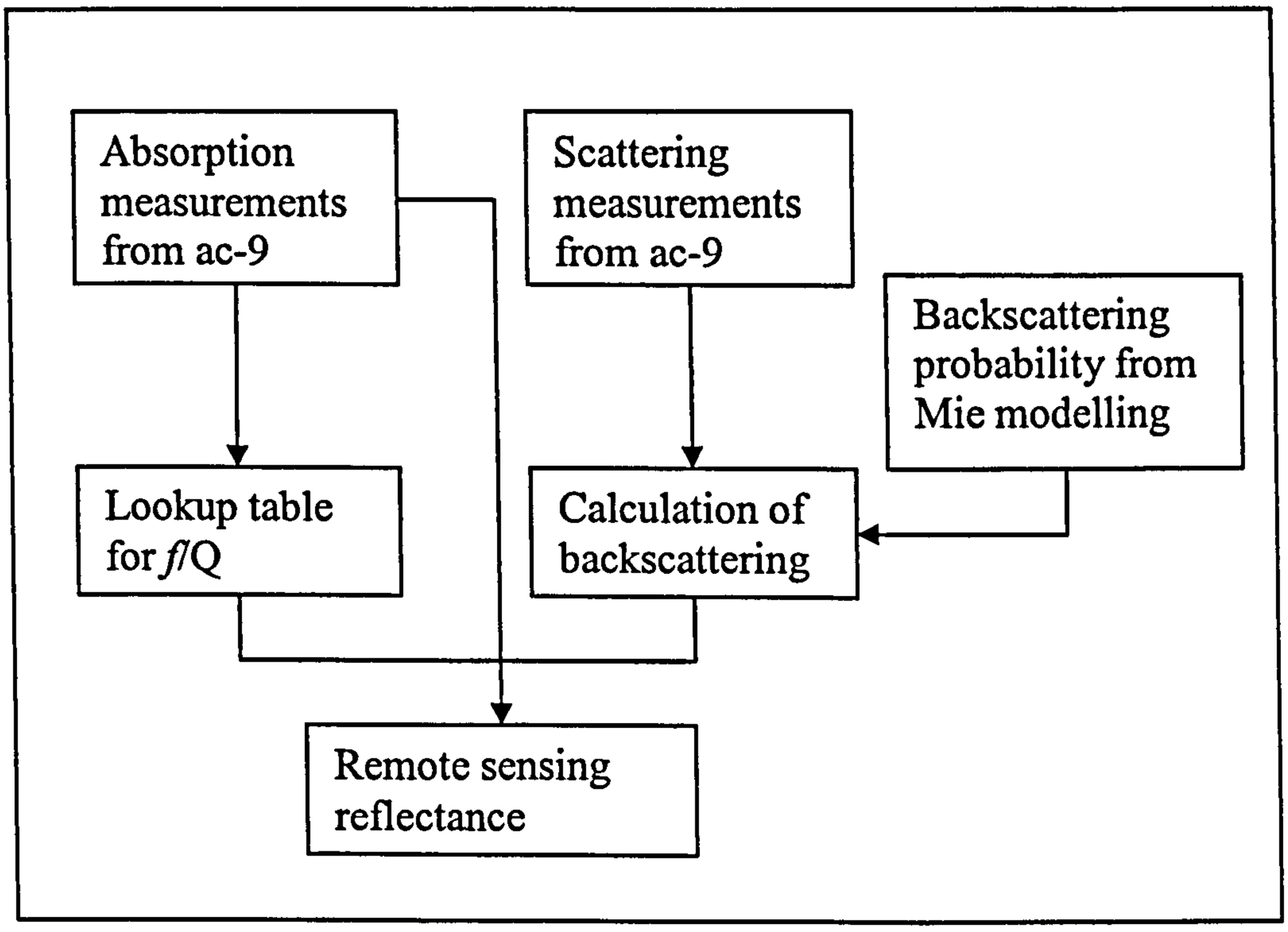

Figure 5.22: Basic scheme explaining the procedure for calculation of remote sensing reflectance from *in situ* inherent optical property measurements.

Section III: Simulating spectral reflectance

5.3.1 Spectral backscattering and Suspended particulate material

Relationships between SPM and b_b at different wavelengths are presented in Figure 5.23. The backscattering values are calculated using the approach explained in Section II (Mie computations). The backscattering at all wavelengths increases with increasing concentration of SPM. The dark line passing through the data points represents the linear fit between particulate suspended material and backscattering. A total of 80 backscattering and SPM concentration values were used to develop the biogeophysical relationship.

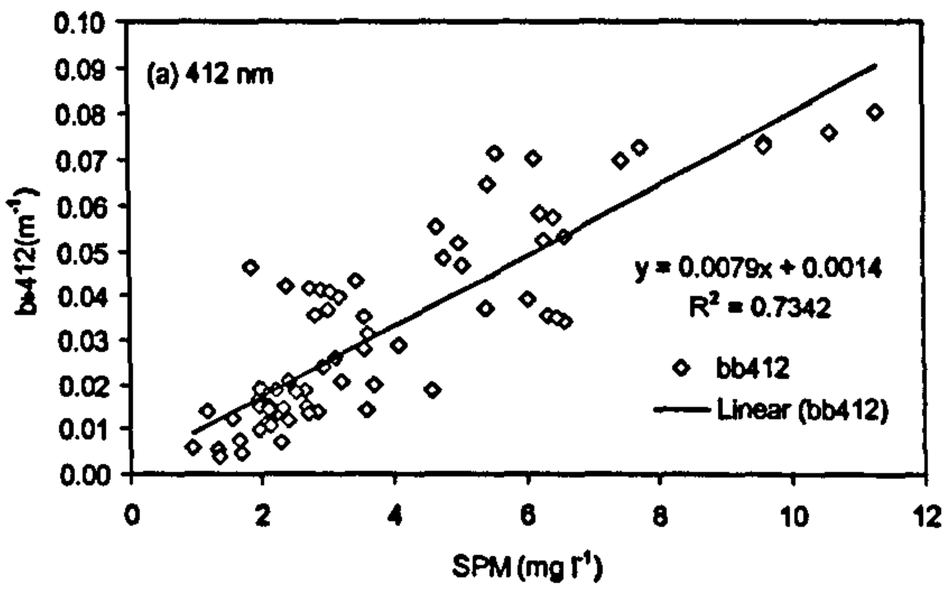

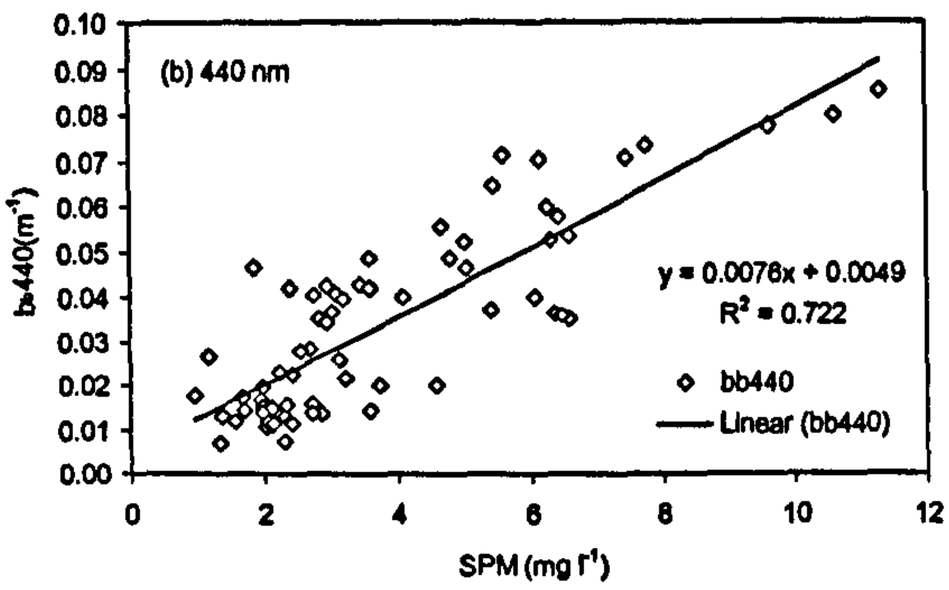

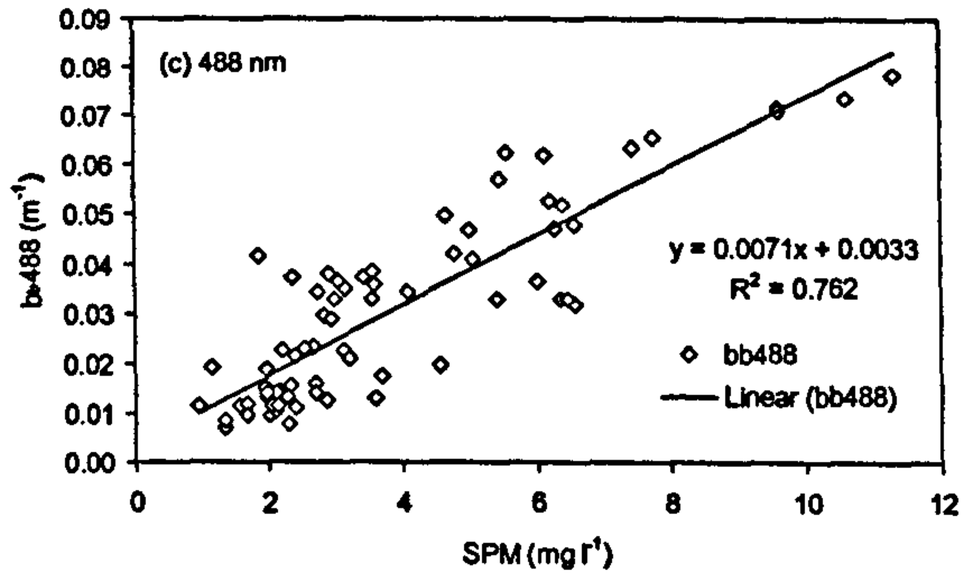

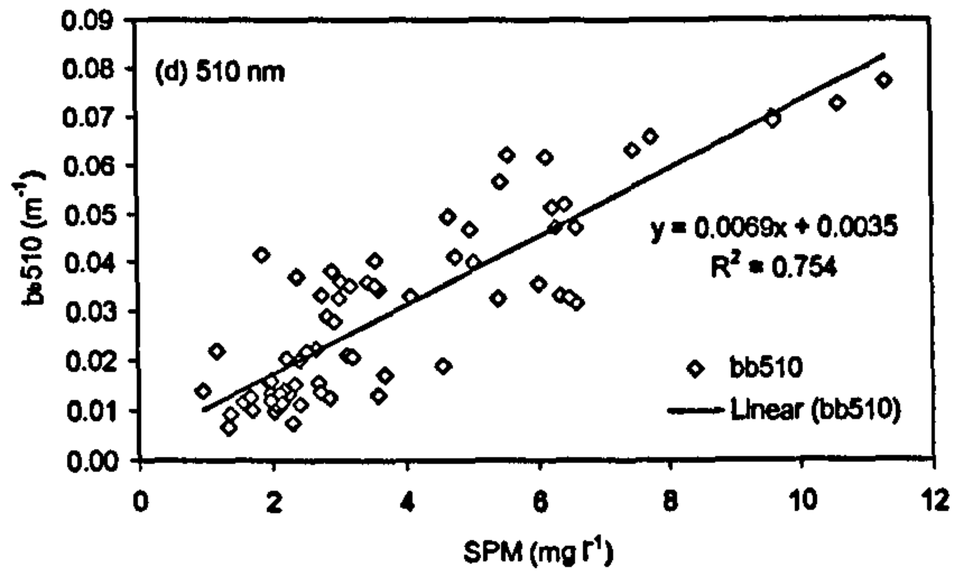

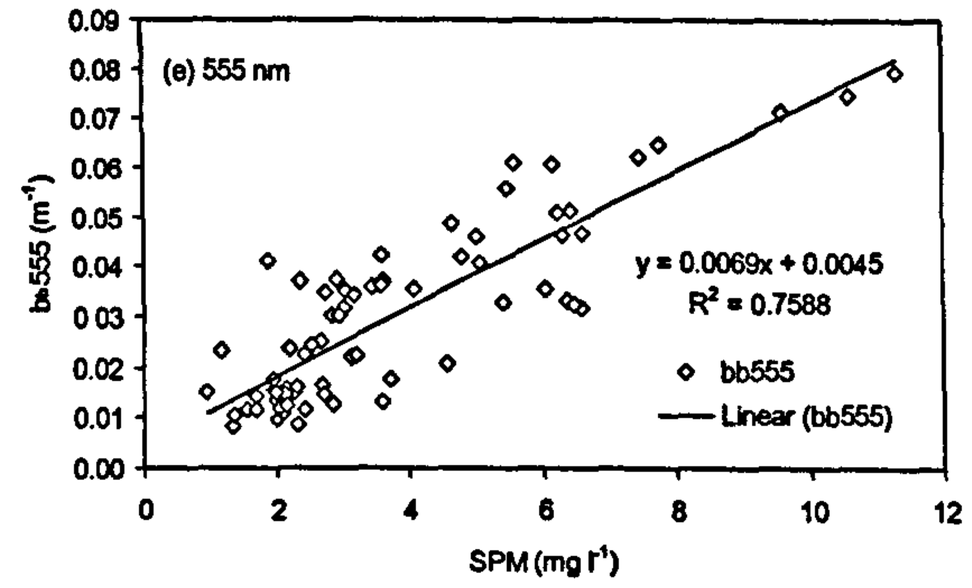

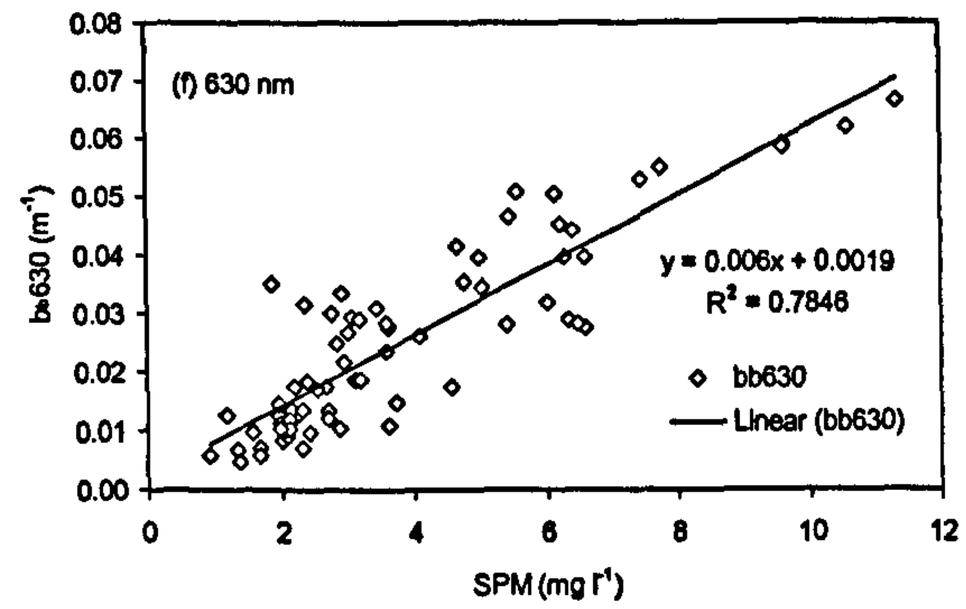

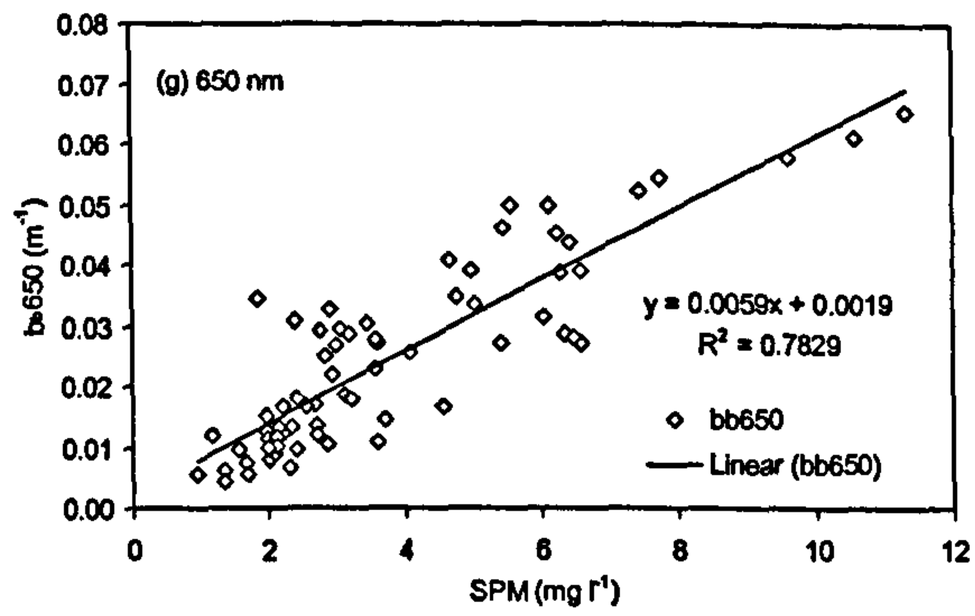

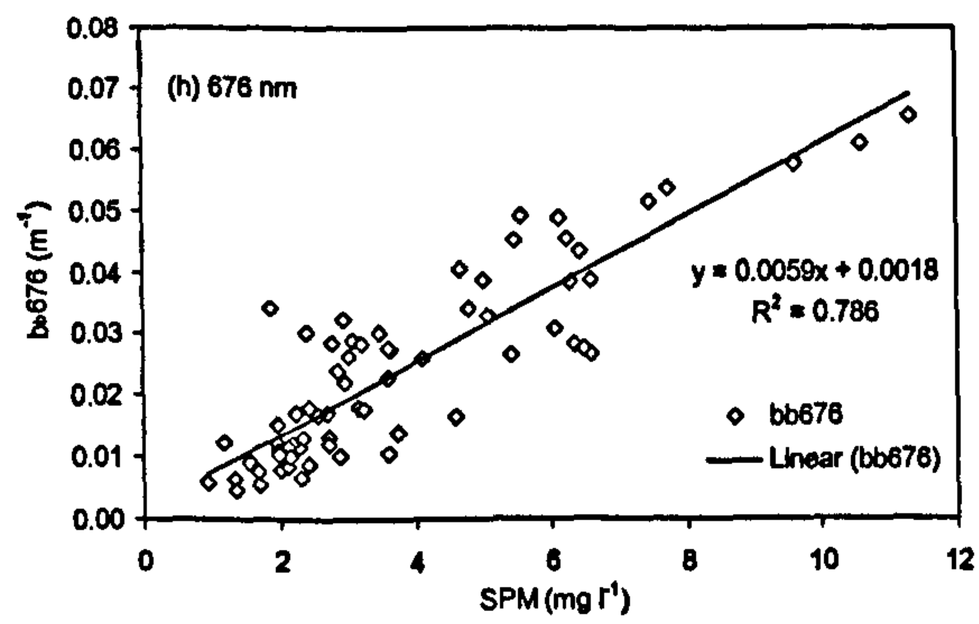

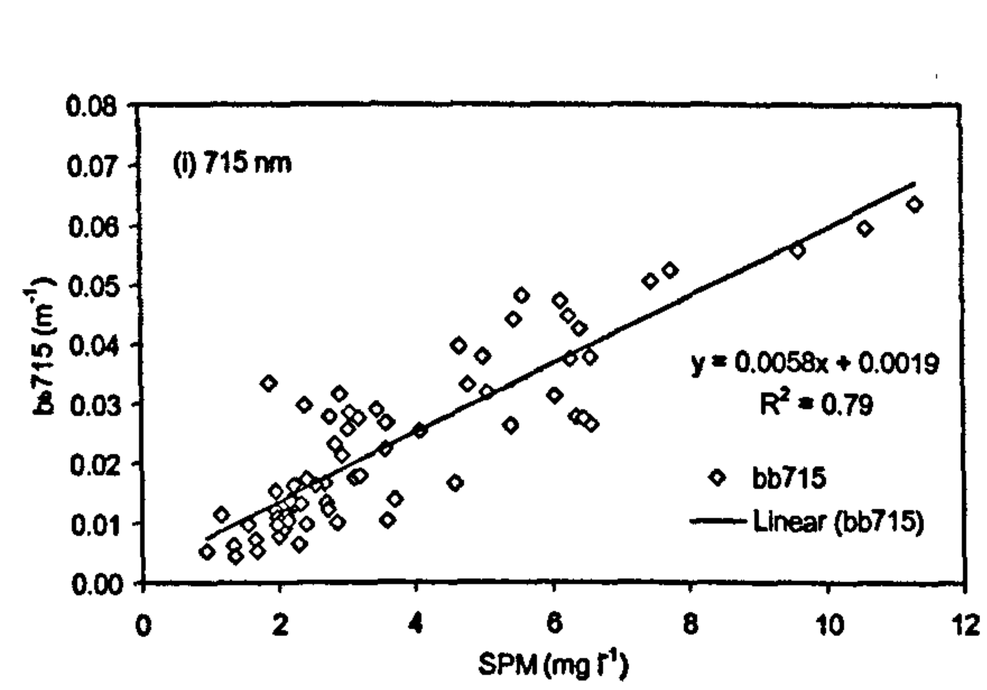

Figure 5.23: Relationship between spectral backscattering (m^{-1}) and SPM (mg l^{-1}). A total of 80 samples are used to develop the relationships between b_b and SPM.

The linear fit representing the relationship between backscattering and SPM is of the general form

$$b_b{}^{SPM}(\lambda) = SPM * \left(b_b{}^{SPM*}(\lambda)\right) + eb_b{}^{SPM*} \qquad \text{eq (5.18)}$$

In the linear fit, the derived slope is the SPM specific backscattering denoted as $b_b{}^{SPM*}(\lambda)$ with $eb_b{}^{SPM*}$ being the error term based on the distribution of the residual of regression that is normally distributed around zero.

In Figure 5.23(a-i), the R^2 values for linear fit are almost identical at all wavelengths. It increases by a very small (at 412 nm, R^2=0.73 and at 715 nm, R^2=0.79) value towards longer wavelengths, which maybe due to the small error associated with absorption at those wavelengths. The relationship between backscattering at 630 nm and SPM was considered for further work. This wavelength is far from the chlorophyll absorption band at 675 nm (Mobley, 1994) and also exhibits a reasonable R^2 (0.78) for the linear fit. As shown in Figure 5.23 (f), the relationship between SPM and $b_b(630)$ is as given in equation 5.19.

$$b_b{}^{SPM}(630) = SPM * 0.006 + 0.0019 \qquad \text{eq (5.19)}$$

The value of 0.006 $m^2\ g^{-1}$ is the mass specific backscattering at 630 nm. Moore and Aiken (2002) have suggested mass specific $b_b(490)$ value of 0.0212 $m^2\ g^{-1}$ whereas Strömbeck and Pierson (2001) estimated a value of 0.0524 $m^2\ g^{-1}$ for Swedish Lakes. As these values are estimated at different locations, it is not possible to compare them. In this research $b_b{}^{SPM*}$ at 440 and 488 was realised as 0.0076 $m^2\ g^{-1}$ and 0.0071 $m^2\ g^{-1}$. The difference in these estimates could be the influence of particle size distribution, particulate composition and concentration.

The spectral distribution of backscattering can be constructed using a power function (Gallie and Murtha 1992), see equation 5.20 and Figure 5.24. The relationship in equation 5.20 explains the influence of SPM concentration on spectral behaviour of b_b, which is further incorporated in the IOP model.

$$b_b{}^{SPM}(\lambda) = b_b{}^{SPM}(630) * \left(\frac{\lambda}{630}\right)^{\gamma b_b} \qquad \text{eq (5.20)}$$

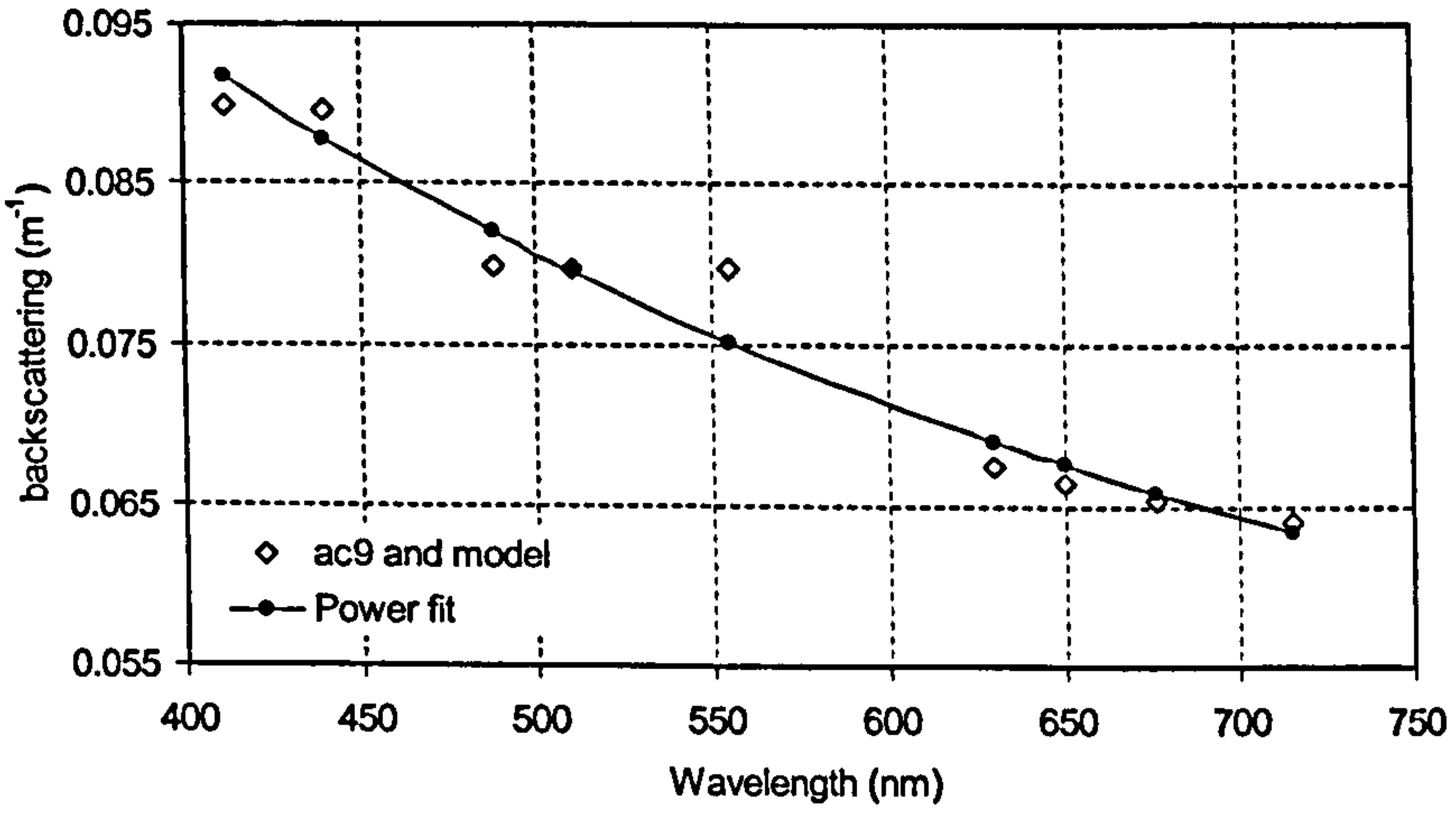

Figure 5.24: Example of spectral backscattering values (22 October 1999, Barn Pool). Dark circles indicate the power fit modelled backscattering values (eq 5.20) that explain the ac-9 derived backscattering (diamonds). SPM =7.5 mgl^{-1}.

5.3.2 Spectral CDOM absorption

Spectral CDOM absorption can be explained as an exponential relationship (Kirk 1994). This behaviour was explained in Chapter 4. In this research, spectral absorption measurements of both CDOM and total particulate material were made (Sections 4.3 and 4.4). Total particulate and dissolved absorption (a_{pg}) can be explained as the sum of absorption due to particulate material and dissolved material. Using the spectrophotometric absorption values, the percentage proportions were calculated and the ac-9 absorption values portioned accordingly.

The spectral CDOM absorption values were computed using the following relationship (Kirk 1994)

$$a_g(\lambda) = a_g(440)\exp(-S_y(\lambda - 440)) \qquad \text{eq (5.21)}$$

using the spectrophotometric percentage proportion values the ac-9 absorption was partitioned at 440 nm and equation 5.21 used to reconstruct the CDOM absorption spectra. S_y is the spectral slope of CDOM absorption. In figure 5.25, the dark diamonds are a_{pg} measurements and the solid line represents a_g calculated using equation 5.21.

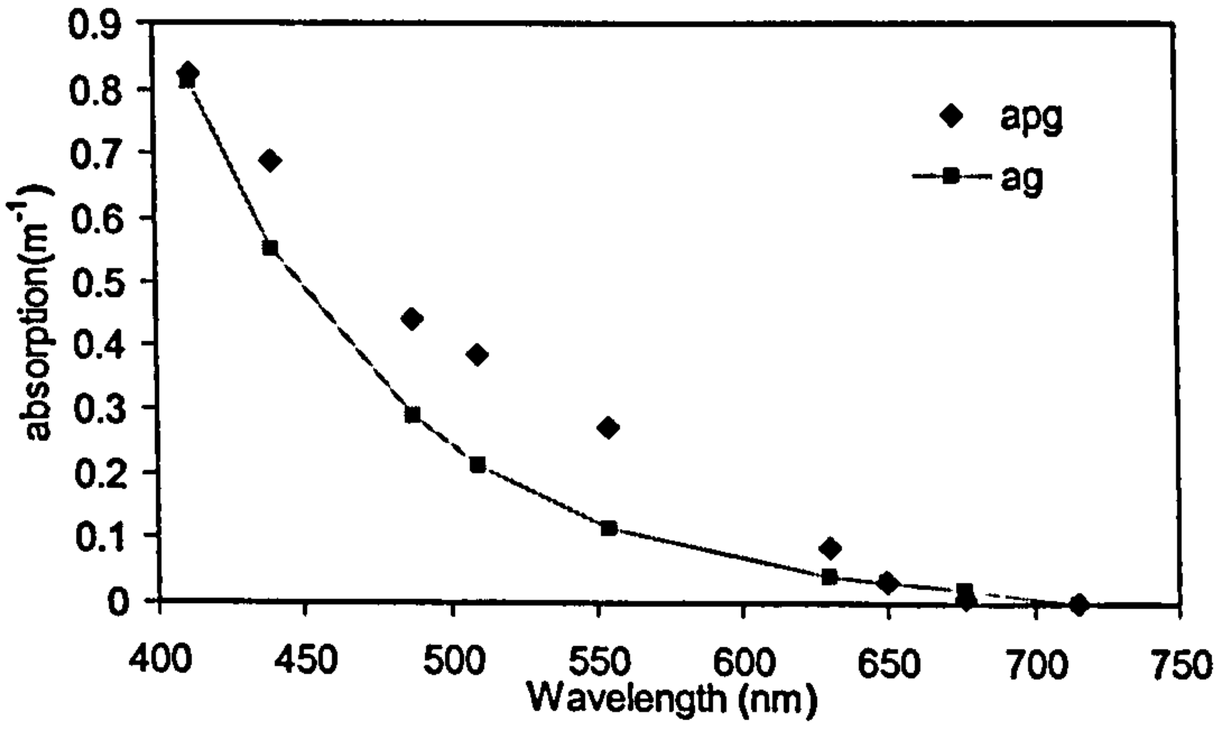

Figure 5.25: Absorption values from 09 December 1999, Barn Pool. a_{pg} is the total particulate and dissolved material absorption measured by ac-9. a_g is the CDOM contribution towards a_{pg}. Spectrophotometric absorption values at 440 nm were used to partition ac-9 measured a_{pg}. The grey line is absorption due to CDOM constructed using equation 5.21.

5.3.3 Suspended particulate material and particulate absorption

Suspended particulate material is a complex combination of organic and inorganic components. These components vary with time and location and in large proportions, which is typical of complex coastal waters. In coastal waters, SPIM is the dominant component (Figure 5.5) and so the absorption properties of these waters are mostly influenced by non-planktonic material. Figure 5.26 is a regression between the particulate absorption at 412 nm and SPM concentration. The mass specific particulate absorption (Figure 5.26) is higher than estimated by Bowers *et al.* (1996) and Babin *et al.* (2003b), which is presented as 0.0235 and 0.031 $m^2\ g^{-1}$ respectively. This difference could have resulted from the difference in particle composition and absorption propeties.

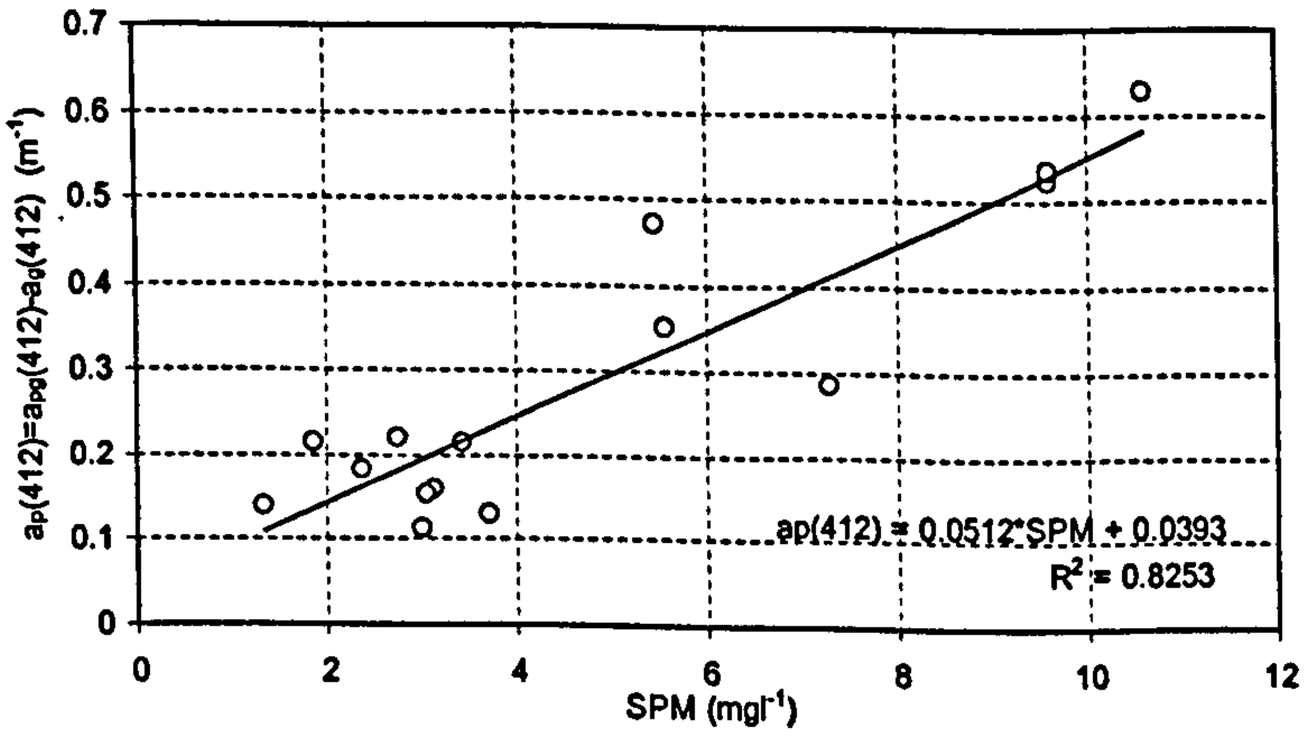

Figure 5.26: Linear regression between suspended particulate material and particulate absorption measurements from Plymouth Sound (1998-2000).

Absorption values, $a_{pg}(412)$, were chosen from those spectra with minimal planktonic influence and absorption due to CDOM was subtracted. These spectra were further screened for phytoplankton absorption peaks at 443 and 676 nm. The regression between $a_p(412)$ and SPM can be generalised as in equation 5.22.

$$a_p(412) = a_p^*(412) * SPM + e_{ap}^* \qquad \text{eq (5.22)}$$

The derived slope of the relationship is the SPM-specific absorption $a_p^*(412)$. e_{ap}^* is an error term based on the distribution of the residual of the regression, which is normally distributed around zero.

In coastal waters, the spectral absorption by SPM (in the presence of minimal optical activity from phytoplanktonic material) can then be calculated from the value of $a_p(412)$ as given in equation 5.23

$$a_p(\lambda) = a_p(412)e^{-S_d(\lambda-412)} \qquad \text{eq (5.23)}$$

where S_d is the shape factor that defines the spectral distribution and can be calculated by an iterative curve fit for each individual measured absorption spectra. Figure 5.27 represents the particulate absorption derived from the ac-9 measurements. The grey line is the reconstruction of the spectral absorption using the approach presented in equations 5.22 and 5.23.

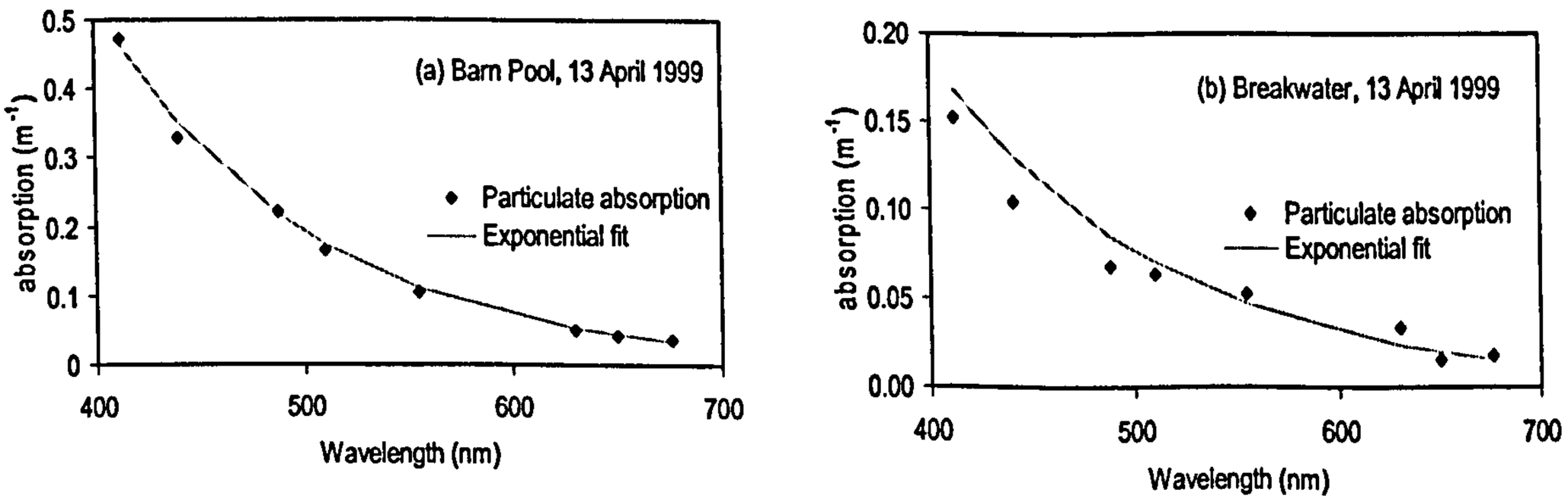

Figure 5.27: Spectral particulate absorption from (a) Barn Pool and (b) Breakwater, 13 April 1999. The dark diamonds represent the ac-9 derived particulate absorption measurements and the solid line is the exponential fit that explains this spectral distribution.

5.3.4 Simulating IOP ratio

Finally, the established relationships between biogeophysical components and optical properties were incorporated into the IOP ratio (Figure 5.28), which is part of the radiance reflectance and remote sensing reflectance equation as shown in equations 5.14 and 5.17. Figure 5.28 shows a comparison between the ac-9 derived and model simulated IOP ratio. The dark diamonds in the plots represent the ratio that used ac-9 absorption and backscattering modelled from ac-9 scattering. The squares represent the simulated ratio generated using relationships summarised in Figure 5.28. Table 5.6 presents the parameters used for simulations for these four examples and relative error estimates.

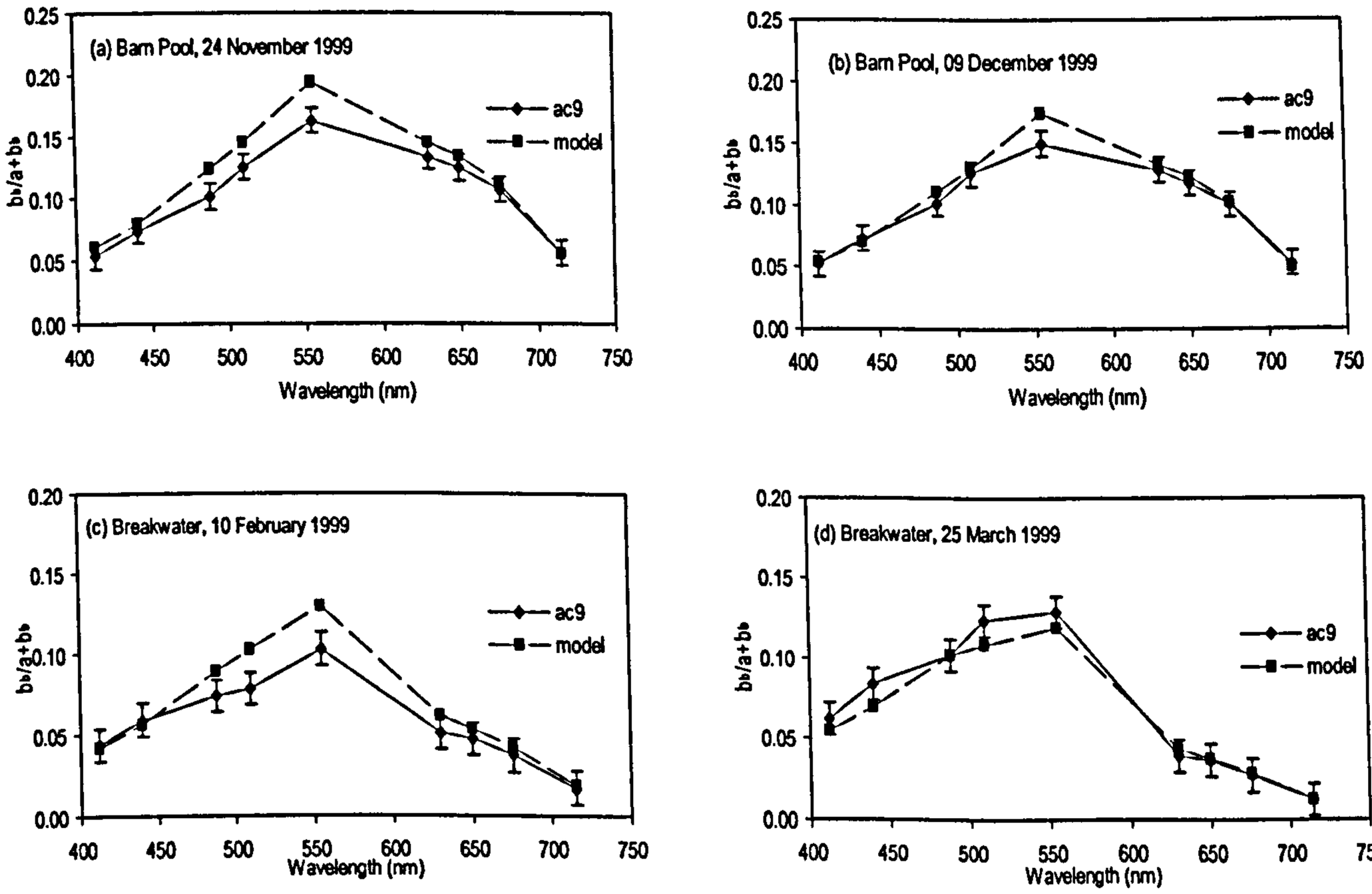

Figure 5.28: Comparison of IOP ratio $b_b/a+b_b$. Diamonds represnt ac-9 derived ratio and and the park circles and line represent the semi-empirical model outputs.

The spectral shape of the IOP ratio is due to particulate and dissolved absorption. In the shorter wavelengths, the shape is a contribution from CDOM absorption and in the near-infrared region it is defined by the absorption due to water. But the magnitude of this ratio is controlled by the backscattering component involved in the numerator as shown in the flowchart (Figure 5.29). The variation in magnitude of IOP ratio value is due to its direct dependency on the SPM concentration (equation 5.19 and 5.20).

The precision of ac-9 after temperature and scattering corrections is reported to be 0.002 m^{-1} (Chang *et al.*, 2003). The accuracy is dependent on wavelength; uncertainty in scattering correction for particulate absorption can result in accuracies up to 20% in the blue wavelengths (Zenveld *et al.*, 1994). The reported ac-9 calibration accuracy is 0.01 m^{-1} from 412-715 nm (www.wetlabs.com/products). All the above errors can have a cumulative affect, but it can be controlled by good quality control practice. In this research, the protocol (Section 4.6.2) followed assures a good quality of data, but the inherent calibration accuracy associated with instrument defines the minimum error. In Figure 5.28 a value of ±0.01 m^{-1} (representing the calibration accuracy) is used as the extent of error bars. The model predict values close to the ac-9 derived IOP ratio values. The calculated spectral relative error is an estimate of the performance of the model. Seventy percent of the total samples have a relative error less than 20%, which explains the reliability of the model.

Table 5.6: *In situ* measurement inputs used for simulating IOP ratio in Figure 5.28

Date	Location	SPM mgl^{-1}	%[a_t-a_g(440): a_g(440)]	%Relative error
24-Nov-99	Barn Pool	10.605	48:52	11.89
09-Dec-99	Barn Pool	9.6	40:60	4.93
10-Feb-99	Breakwater	3.13	26:74	16.48
25-Mar-99	Breakwater	1.95	17:83	-6.30

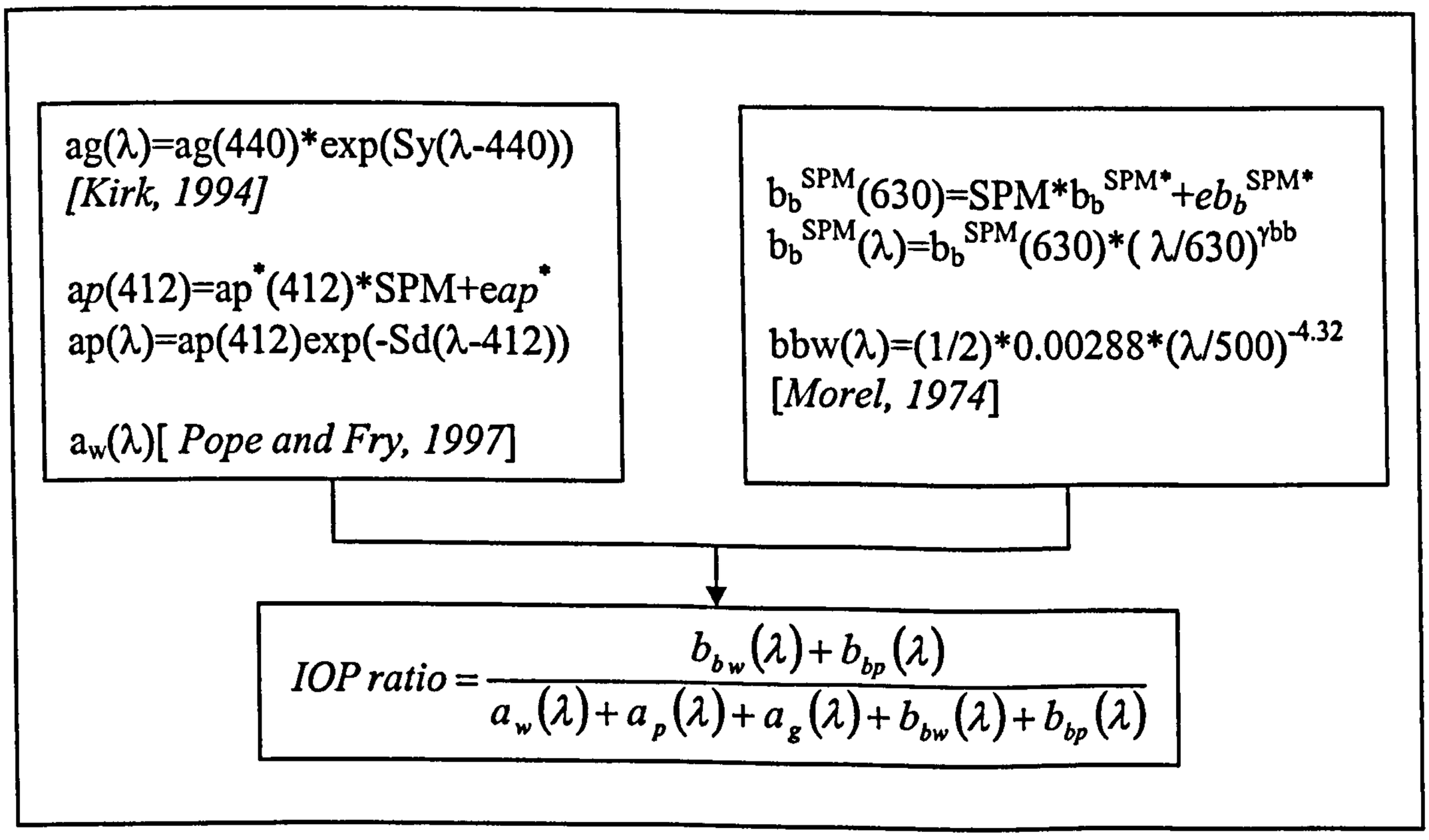

Figure 5.29: Scheme for the calculation of the IOP ratio.

5.3.5 Sensitivity analysis

The sensitivity of the model was tested by varying the concentrations and number of input parameters. The model concentrations were varied over the ranges measured during the *in situ* campaigns. In this model, SPM concentration and CDOM absorption are the two components that influence the optics spectra in coastal waters. The spectral slope of absorption and backscattering of these optically active constituents was also tested for their influence on the IOP ratio. The output of this model (IOP ratio) was also tested for errors induced by various regressions. The focus of this analysis was to understand the ability of the model to reproduce the optical behaviour of coastal waters, which are dominated by minerogenic SPM and CDOM and have a minimal planktonic contribution towards the optical behaviour.

5.3.5.1 Influence of SPM concentration

SPM measurements from all *in situ* data collection campaigns were compiled and the minimum and maximum values identified (Table 5.2 and 5.3). This minimum and maximum range was used as inputs to the model to simulate the IOP ratio and to understand its variability. The magnitude of the IOP ratio increases with increasing SPM concentrations (Figure 5.30). The SPM concentration was varied between 0.5 to 11.5 mgl^{-1} as observed *in situ*. All the other parameters were fixed for this simulation. The absorption of CDOM was fixed at 0.5 (m^{-1}) with a slope of 0.014 (nm^{-1}) and the slope of the particulate absorption was fixed at 0.01(nm^{-1}).

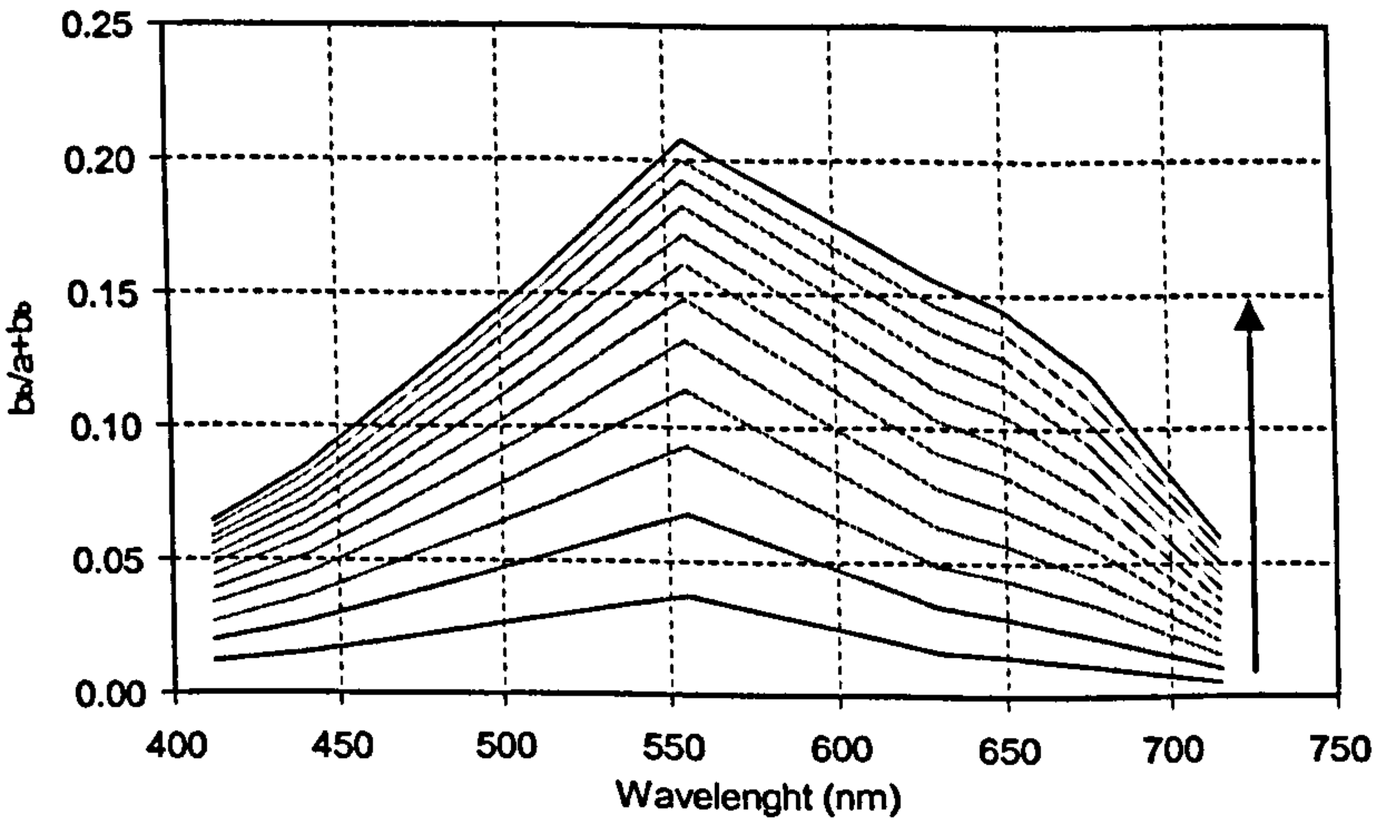

Figure 5.30: Sensitivity analysis that shows the variability in the magnitude of the IOP ratio with respect to increasing SPM concentration. The bottom and top line of the plot represents SPM concentrations of 0.5 mg l^{-1} and 11.5 mg l^{-1} respectively, with SPM increments of 1.0 mg l^{-1} (increasing in the direction of arrow).

From equations 5.19 and 5.20 it is clear that backscattering due to particulate material is directly dependent on the SPM concentrations. So an increase in SPM directly influences the IOP ratio as backscattering is in the numerator of the IOP ratio. This influence of SPM concentrations can also be observed in the *in situ* measurements presented in Figure 5.21 and 5.28.

5.3.5.2 Contribution of slope of spectral backscattering

As given in equation 5.20, backscattering is influenced by both the SPM concentration and backscattering slope (γ_{bb}), which distributes the magnitude spectrally. The value of γ_{bb} can be related to the particle size distributions following the explanations by Mie computations (Section 5.2.5). But for this research, no detailed investigations were made to establish a relationship between particle size distribution and slope of spectral backscattering, which would need intensive and high resolution *in situ* particle size and backscattering measurements. The value of γ_{bb} was varied in the range observed from the measurements of ac-9 derived b_b, between 0.4 and 0.9. The change in IOP ratio with respect to input γ_{bb} was more significant in the blue-green region than red or NIR, which migrated from the behaviour of spectral backscattering (Figure 5.31 b).

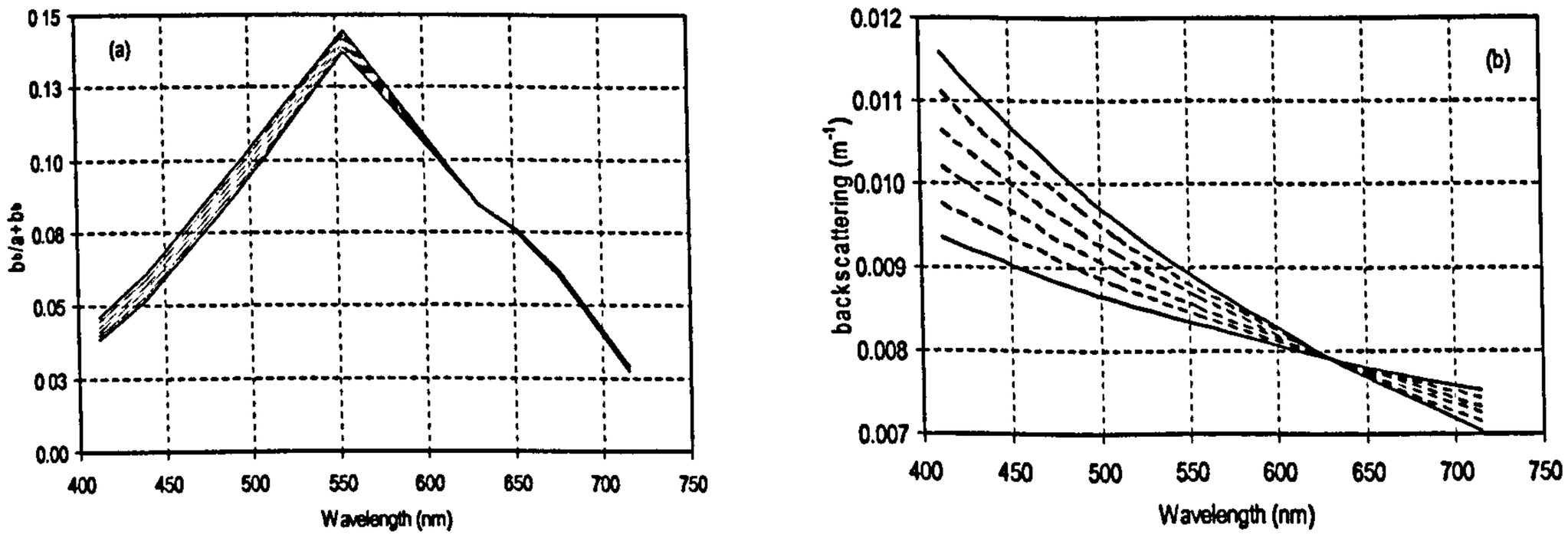

Figure 5.31: Sensitivity analysis showing the Influence of slope of spectral backscattering on IOP ratio. The bottom and top line of the plot represents the spectra simulated using backscattering slope 0.4 and 0.9 respectively, with intermediate increments of 0.1.

5.3.5.3 Influence of particulate absorption

Figure 5.32 explains the possibility of two conditions, one, in which the SPM is capable of contributing towards the total absorption and the other, is when SPM is non-absorbing (contribution is negligible). Figure 5.32a presents the response of the IOP ratio for varying SPM concentrations and the particulate material is of an absorbing nature (does not include planktonic material). Figure 5.32b presents the response in the presence of non-absorbing particulate material. Figures 5.32c and d present the IOP ratio at the extreme ends of the SPM distribution. From Figure 5.32 it was clear that the absorption properties of particulate material have a significant influence on the magnitude of the IOP ratio. It was also observed that the convex shape in the green-red region becomes concave in the presence of non-absorbing particulate material. In all the above situations/examples the values of $a_g(440)$ and S_y were fixed to 0.5 m^{-1} and 0.014 nm^{-1}.

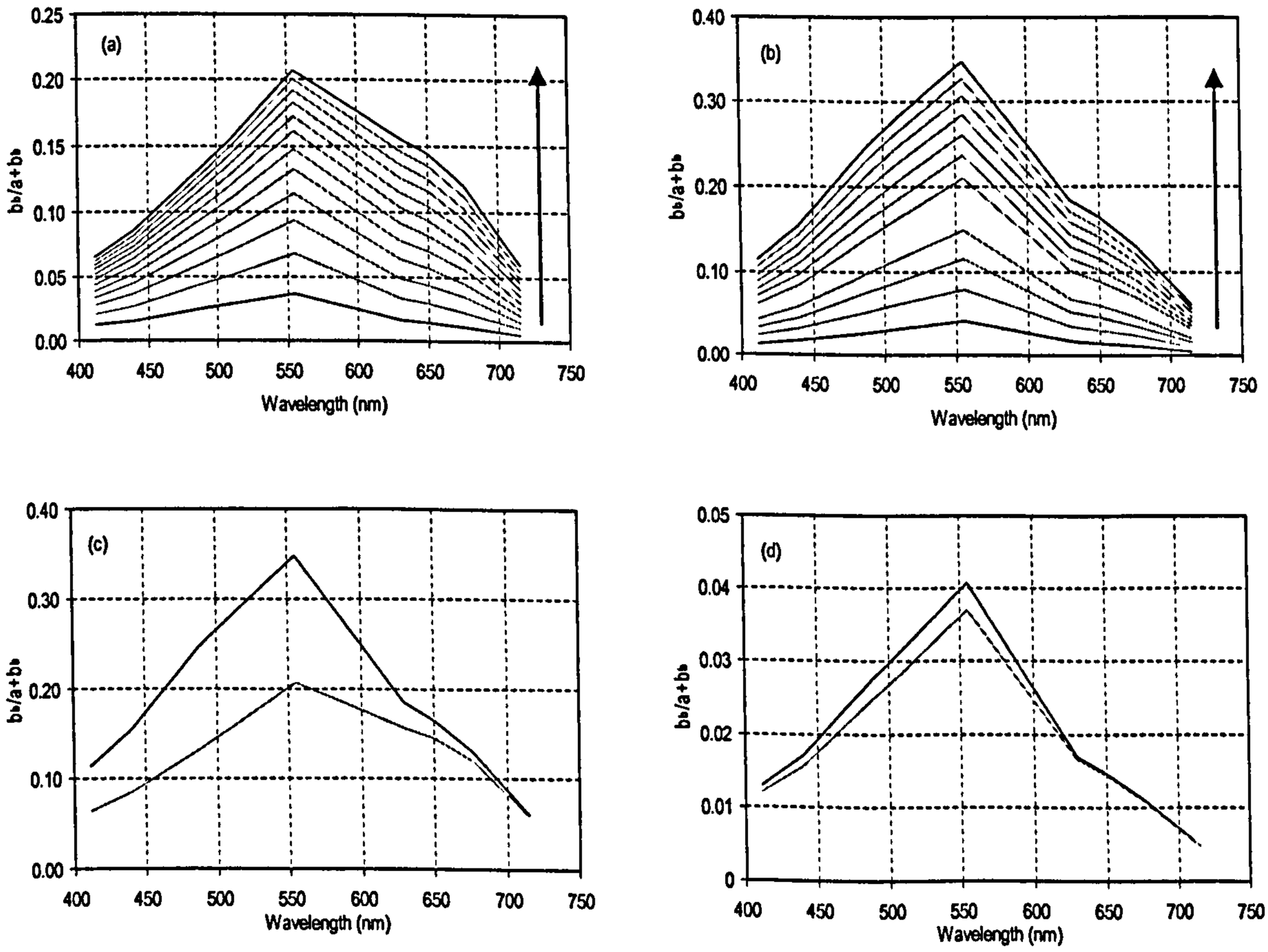

Figure 5.32: (a) Influence of absorbing SPM variability towards IOP ratio. (b) Influence of non-absorbing SPM variability towards IOP ratio. In both (a) and (b) the concentration of SPM increases between 0.5 -11.5 mg l^{-1} with an increment of 1.0 mg l^{-1} in the direction of the arrow. (c) Variability at 11.5 mg l^{-1}, top line represents non-absorbing particulate material and bottom line represents absorbing particulate material. (d) Variability at 0.5 mg l^{-1}, top line represents non-absorbing particulate material and bottom line represents absorbing particulate material.

5.3.5.4 Influence of dissolved and particulate material absorption

Figure 5.33 gives a clear explanation of the influence of absorption due to particulate and dissolved material on the IOP ratio. Different combinations of optically active components were introduced to test the sensitivity of the model. The SPM concentrations were varied in the range of 0.5-11.5 mgl^{-1}. When introduced, the CDOM absorption (a_g440) was set at 0.5 m^{-1} with a slope of 0.014. The slope of particulate absorption was set to the mean value of 0.01 with $a_p(412)$ values calculated using the approach proposed in equation 5.22.

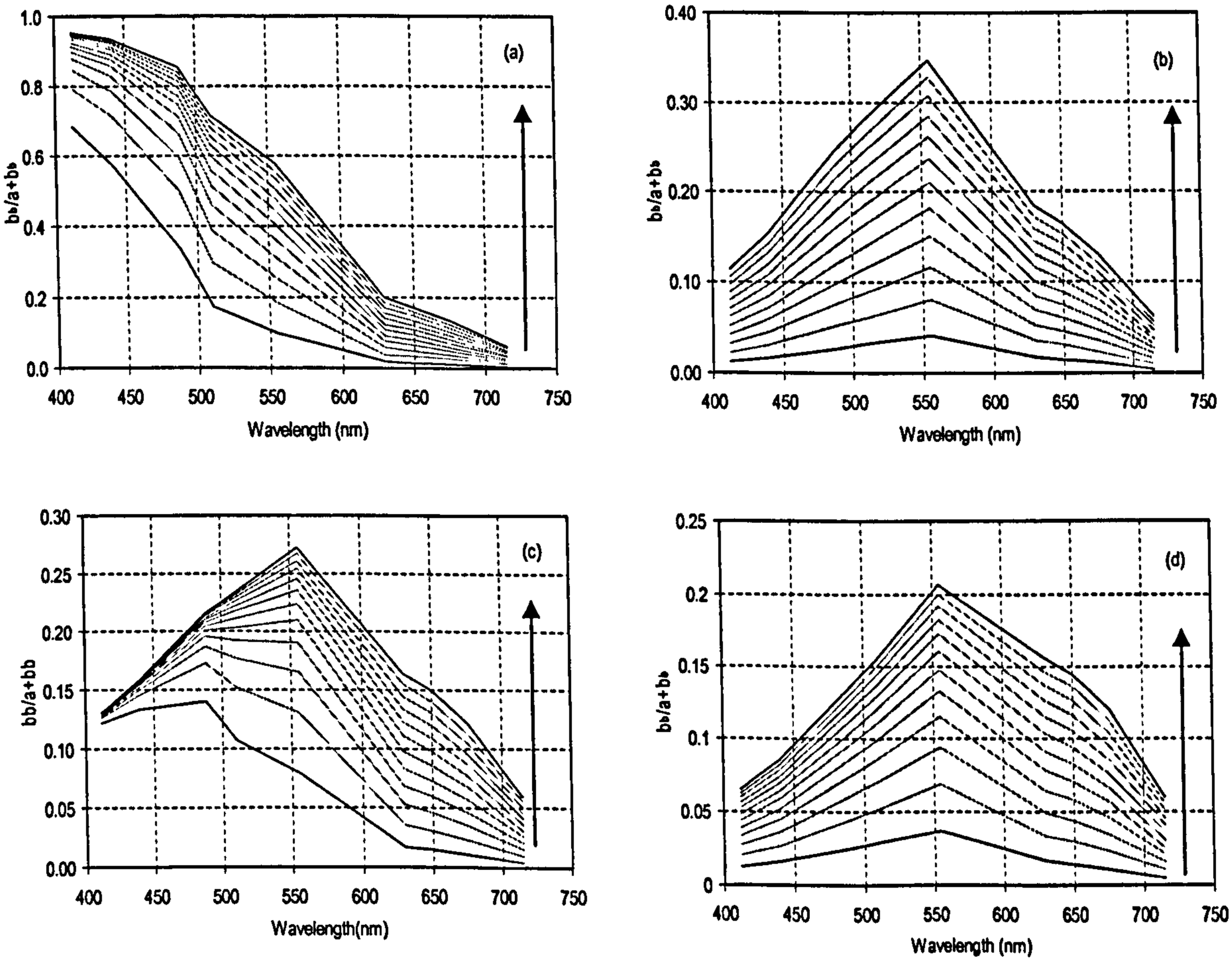

Figure 5.33: IOP ratio simulations for varying SPM concentrations with (a) no particulate or dissolved substance absorption; (b) absorption only due to dissolved susbstances; (c) absorption only due to particulate material; (d) absorption due to both particulate and dissolved material. In all the above figures the concentrations of SPM increases between 0.5 -11.5 mg l^{-1} with an increment of 1.0 mg l^{-1} in the direction of the arrow.

In the absence of absorbing agents the shape of the IOP ratio was significantly (absorption due to water remains) controlled by the particulate and molecular backscattering (Figure 5.33a). When CDOM absorption was introduced into this environment then the optical ratio in the blue-green region (Figure 5.33b) was

controlled by the absorption properties of the CDOM. When absorbing particulate material was introduced then the shape of the IOP ratio was modified as shown in Figure 5.33c. Finally, in the presence of optically active particulate and dissolved material (Figure 5.33d) the spectral shape of IOP ratio was controlled both by particulate and dissolved substance contributions. The higher absorption by particulate and dissolved substances influence the spectral shape in the blue-green region and the absorption by water dominates the contributions in the red-infrared region. But it was the backscattering due to water and particulate material that set the magnitude for the IOP ratio values.

5.3.5.5 Influence of CDOM absorption and its spectral slope

From the *in situ* measurements, a wide variety of spectral slopes for CDOM absorption was observed in the range of 0.014-0.025 m^{-1}. Figure 5.34 shows the influence of slope on IOP ratio. The SPM concentration was fixed at 5.0 mg l^{-1} to represent the mean value of its range and $a_g(440)$ was incremented from 0.2 to 0.8 m^{-1} (observed range). The top lines of on Figure 5.34 represent CDOM absorption of 0.2 m^{-1} and the bottom line represents a higher CDOM absorption of 0.8 m^{-1} with the lines in between being increments of 0.1 m^{-1}. The shape of the spectral IOP ratio was unaffected by the change in the slope of the spectral distribution, but the magnitude was clearly influenced (decreases with increasing absorption) and in particular the blue-green region.

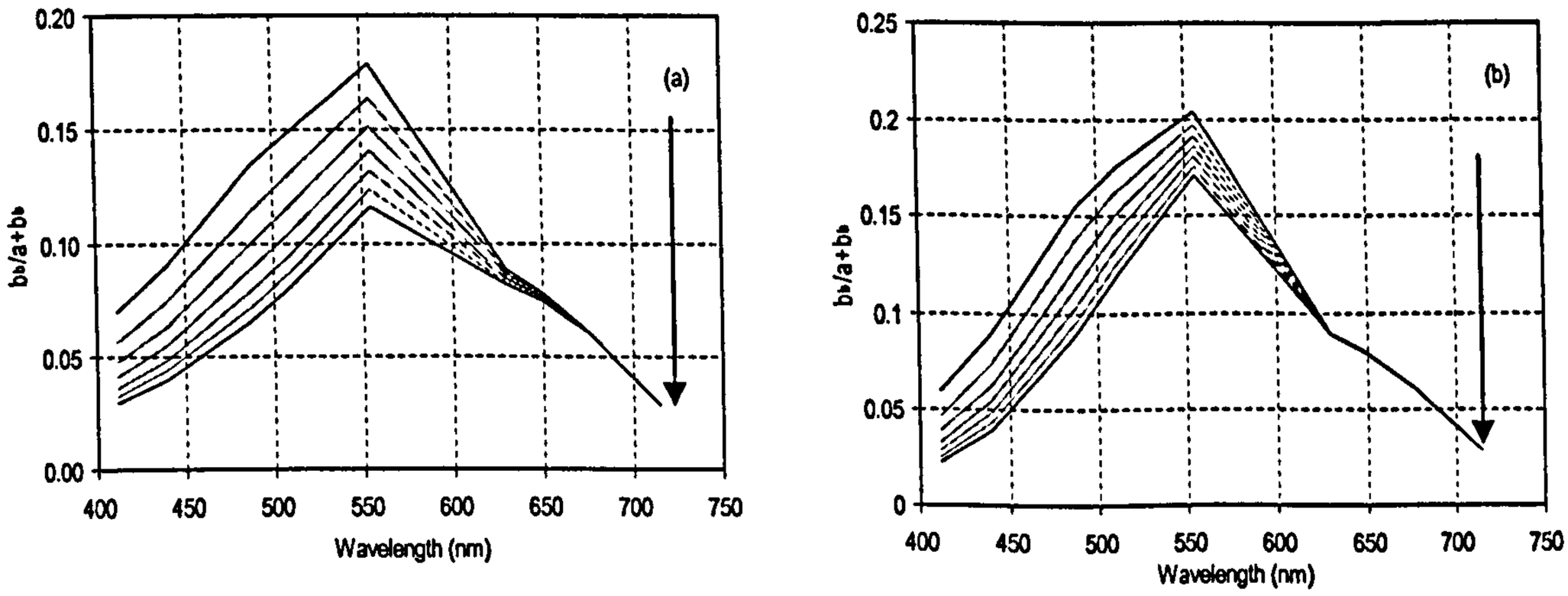

Figure 5.34: Sensitivity analysis to test the influence of spectral slope of CDOM absorption (a) S_y=0.014 nm^{-1} and (b) S_y=0.025 nm^{-1}. a_g440 increases from 0.2-0.8 m^{-1} with an increment of 0.1 m^{-1} in the direction the arrow.

5.3.5.6 Influence of regression residual errors

The model outputs were tested for the influence of two known errors, which are part of the regressions included for calculation IOP ratio. Figure 5.35 presents variability due to the change in the regression residual error in backscattering computations. The error is varied ±50% to observe its influence on the IOP ratio. The IOP ratio changes by ±2.15% spectrally. Whereas when the residual error is varied (±50%) for the particulate absorption it influences the IOP ratio only by ±1.35%. These two results show that the influence of residual errors is only minimal.

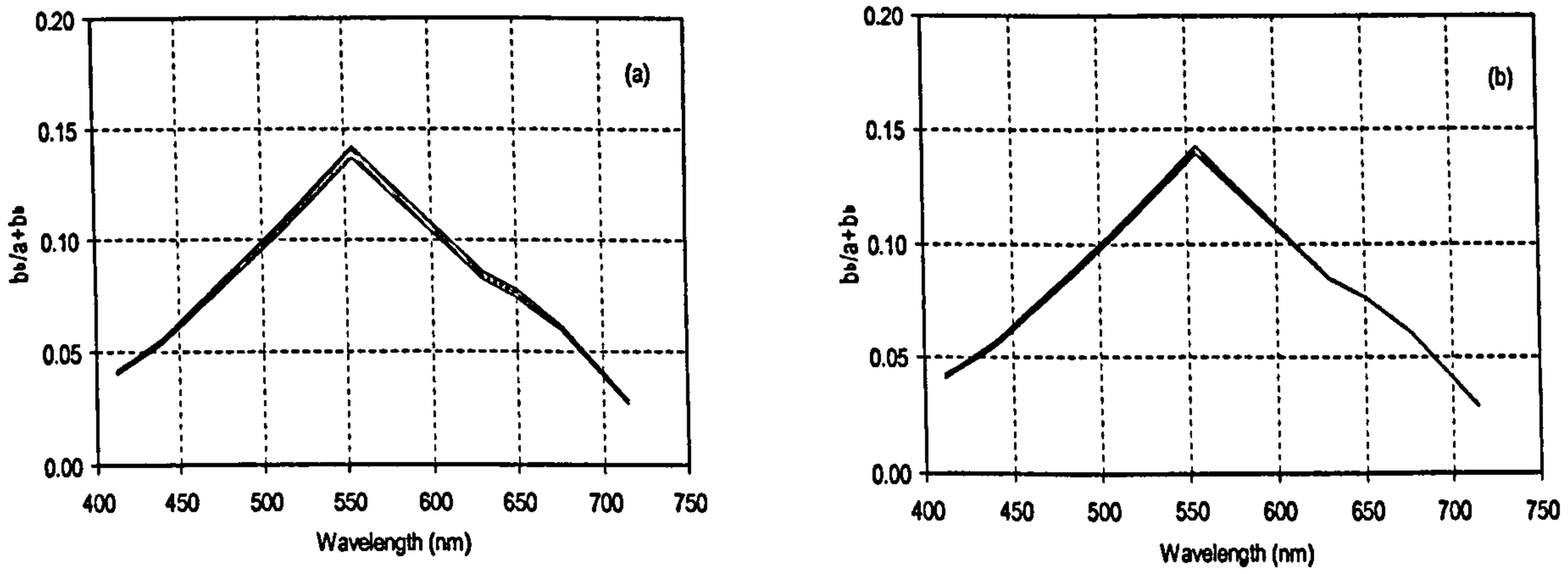

Figure 5.35: Sensitivity analysis, influence of regression residual errors. (a) Variations due to error in backscattering regression. (b) variations due to errors in particulate absorption regression.

Chapter 6 : Discussion

This chapter revisits the rationale of research, the results presented and then discusses the application of developed relationships.

6.1 IOP ratio model

A semi-analytical model has been developed that predicts the IOP ratio, in waters dominated by non-planktonic material, just below the water surface. This model can be extended to predict the radiance reflectance and remote sensing reflectance, where the IOP ratio is predicted as a function of the optically active substances in the water. These optically active substances are linked to the absorption and backscattering coefficients through a series of empirical relationships, and ultimately related to the radiance reflectance and remote sensing reflectance through the IOP ratio.

The development of the relationships, linking the optically active substances to the inherent optical properties, was based on a combination of *in situ* measurements and optical constants derived from numerical modelling. Simulated optical signatures generated using this semi-analytical model explained the spectral shape and magnitude observed *in situ* (Figure 5.26).

The semi-analytical model was used to predict the optical signature at different concentrations of SPM and CDOM absorption (Figure 5.27 and Table 5.6). These predictions are valid only in waters where non-planktonic material is the major contributor to the optical signature. This specific nature of the model is due to the use of SPM samples with a high percentage of inorganic content (Figure 5.5) as an input to various biogeophysical relationships.

6.2 Deriving particulate backscattering

Backscattering values were calculated by a combination of *in situ* inputs and knowledge from numerical modelling of optical behaviour. Mie computations were employed to understand the particulate optical response, with inputs from coulter counter electronic sizing and composition from x-ray diffraction analysis .

Coulter counter measurements were made with a 100 μm orifice, which is sensitive to particles in the 2.0 - 65.0 μm range. Particle numbers and size beyond this range were generated using extrapolation following Boss *et al.*, 2001 and it was also possible to use Laser particle sizing techniques (0.1-200 μm) (Malvern Instruments©). These techniques need a particle refractive index value as an input, which was a single value for all particles, thus including a bias in the calculations made.

For this research, particle sizing using coulter counter (Multi sizer II with a 100 μm orifice) was appropriate as very few large particles were observed beyond 40 μm. The measurement of small particles still remains a problem. Measurements using a flow cytometer can be considered for particles below 2 μm.. Laser particle sizing can be used if there exist, a confidence in the particulate refractive index as an input. There is no technique available at this stage, which is operational and economically viable for this research to examine the composition and size simultaneously.

For the calculation of backscattering probability, a bulk relative refractive index value representative of the dominating SPIM was supplied. Ideally the particle size distribution should be partitioned according to the particle composition and appropriate relative refractive index should be applied for the computation of backscattering probability. No suitable technique was identified that facilitates this partitioning on an operational basis, which resulted in the use of a bulk rather than specific refractive index value. Greater confidence can be achieved for the model predictions, if, specific and relevant relative refractive index is supplied along with *in situ* or water sample measurements for particles below 2 μm.

Particulate backscattering is a product of particulate scattering and the probability of backscattering. Scattering values were obtained from ac-9 attenuation and absorption measurements. The backscattering ratio (probability) was calculated using Mie computations. Calculations of backscattering were regressed against SPM concentrations and extrapolated through the visible-NIR region (Pierson *et.al.*, 2001). Spectral backscattering slope (γ_{bb}) is an important parameter that influences this spectral extrapolation, and depends on the particle size distribution (reference). The current version of the model uses a mean γ_{bb} value observed from the derived ac-9 spectral backscattering values. In future, it is essential to investigate and incorporate the γ_{bb} and particle size distribution (ξ) relationship in the optical model. This can be established only with a good synchronous dataset of *in situ* particle sizing and backscattering measurements.

6.3 Absorption by CDOM

From several previous studies (including Bricaud *et al.*, 1981 and Kirk 1994), absorption behaviour of CDOM was understood to be wavelength dependent, normally exhibiting an exponential behaviour over ultraviolet and visible region. The two components which explain the optical behaviour of CDOM are $a_g(440)$ and S_y. The absorption coefficient is used as an index of CDOM abundance, while the spectral slope S_y indicates the nature and composition of CDOM.

Generally, S_y is low in the coastal waters and higher in the open ocean (Ferrari 2000) and changes in S_y greatly influence the IOP ratio (Figure 5.33). So, to predict an accurate optical signature, it is important to choose an appropriate S_y value. It is easy to choose a S_y value for either coastal or open ocean waters as they have a defined range (Ferrari, 2000), but problems arise when attempting to predict the optical signature in a continuously mixing domain like an estuary. The tidal cycle mixes the water and its constituents continuously, which results in a highly dynamic optical domain. In this research only individual samples were used to simulate the optical signature, but while constructing a dynamic optical model, attention must be paid to include the mixing effects.

6.4 Absorption by particulate material

Absorption in natural waters is a cumulative contribution of water, CDOM and particulate material in suspension. Humic solids, planktonic and minerogenic particulate material are contributors towards total particulate absorption. In coastal waters, the particulate material is generally of an inorganic nature although this domination is controlled by the seasons. The organic contribution can become dominant in the summer due the dominant presence of phytoplankton.

An attempt was made to predict the optical signature only when the SPIM was dominating the particulate material, which implies that the model may not be applicable in the summer. It is important to investigate and include the contribution of absorption due to organic material, to make the model complete. This demands detailed optical compositional studies of both planktonic and humic particulate material, which is beyond the scope of this research.

6.5 *In situ* and laboratory measurements

A wide variety of measurements were made for this research, which provided an understanding of the optical and biogeophysical behaviour in coastal waters. *In situ* measurements included salinity, temperature, inherent and apparent optical properties. Water samples were collected and processed in the laboratory to measure the particle size, composition of particulate material, concentrations of suspended and dissolved material. Strict protocols were followed while making all measurements and no major bias was observed in the measurements made.

In situ optical data was available only from the monthly sampling conducted during COLORS project (1998-2000). More frequent (weekly) optical measurements would have been advantageous, because *in situ* measurements of backscattering can improve the confidence of the spectral backscattering model results.

XRD analysis has provided information about the abundance of different minerals present in the SPM, but it provides only an indication of abundance rather than a numerical value. This is a major disadvantage, from modelling point of view, as it forces the uses of a bulk relative refractive index value for the entire particle size distribution. No method was identified during this research, which is both operational and economical, to be implemented towards particle specific composition.

Particle size measurements were made in the laboratory as only bench based instruments were available for this research. Instead *in situ* measurements would have been better as this avoids the settling and flocculation of particulate material.

Chapter 7 : Conclusion and Future work

7.1 Conclusion

In this research a biogeooptical model was developed to predict the optical signature in coastal waters. The model is based on forward modelling approach, where marine constituents are related to the inherent optical behaviour. The results show that this model is a promising approach to explain the remote sensing signal. The three major achievements of this research maybe summarised as follows:

- The biogeooptical model is successfully applied to explain the reflectance signal in coastal waters dominated by minerogenic particulate material and chromophoric dissolved substances.
- The forward model is used to simulate the inherent optical ratio signal in the observed range of marine constituent concentrations. These simulations clearly demonstrate the applicability of this approach in the construction of lookup tables relating biogeophysical parameters and the optical signature.
- A spectral particulate backscattering probability model for coastal waters dominated by minerogenic material is proposed. Results show that this model can produce backscattering values in a more realistic way than with the constant probability value as proposed by Petzold. However, *in situ* backscattering measurements are required to further validate this approach.

7.2 Future work

The focus of future research would be in strengthening the relationships with more intensive *in situ* measurements and by collecting data from different coastal locations around the United Kingdom. These measurements would include hyperspectral optical measurements and biogeophysical measurements, compositional analysis to establish particle nature and high resolution particulate size and shape parameter measurements to provide better confidence in the optical model predictions.

This model could be inverted with a lookup table to predict constituent concentrations from reflectance. In turbid coastal waters, airborne and spaceborne sensors such as Compact Airborne Spectral Imager (CASI), CHRIS PROBA and MERIS can provide

high resolution data. If this high resolution data is atmospherically corrected (Moore *et al.*, 1999), the reflectance values from the sensors can be supplied to the inverse lookup table and the concentrations of constituent materials can be derived. The concentrations thus obtained can be used to run biogeochemical models, mapping suspended sediments, sediment flux monitoring, identification of blooms and pollution monitoring.

Appendix 1: Acronyms and Symbols

Acronyms

AOP	Apparent Optical Property
CDOM	Chromophoric Dissolved Organic Material
CTD	Conductivity, Temperature and Depth
COLORS	COastal region LOngterm measurements for colour Remote Sensing development and validation
IOP	Inherent Optical Property
JGOFS	Joint Global Ocean Flux study
PML	Plymouth Marine Laboratory
REVAMP	REgional VAlidation of MERIS Chlorophyll Products *in North sea coastal waters*
SPM	Suspended Particulate Material
SPIM	Suspended Particulate Inorganic Material
SPOM	Suspended Particulate Organic Material
TSM	Total Suspended Material
UoP	University of Plymouth
rri	Relative refractive index

Symbols

Φ	W	Radiant flux of energy
Φ_a	W	Absorbed radiant flux
Φ_b	W	Scattered radiant flux
Φ_i	W	Incident radiant flux
α		Size parameter
β	m^{-1}	Volume scattering function
ε	$F\ m^{-1}$	Electrical permittivity
ε_0	$F\ m^{-1}$	Permittivity of free space
ϕ	°	Azimuth angle
$\Delta\phi$		Azimuth difference
γ		Hyperbolic slope of particulate attenuation
γ_{pg}		Hyperbolic slope of attenuation due to both particulate and dissolved materail
λ	nm	Wave length
μ	$H\ m^{-1}$	Magnetic permeability
μ_0	$H\ m^{-1}$	Permeability of free space
$\bar{\mu}_d(z;\lambda)$		Average cosine of downwelling light
$\bar{\mu}_u(z;\lambda)$		Average cosine of upwelling light
ν	s^{-1}	frequency
θ_s	°	Sun zenith angle
θ_v	°	Viewing angle

θ_r	°	Refracted angle
ρ		Fresnel reflectance for upwelling irradiance
$\bar{\rho}$		Fresnel reflectance for down welling irradiance
$\rho\perp$		Reflectance for perpendicularly polarised light
$\rho\|\|$		Reflectance for parallel polarised light
σ	$W\ m^{-2}\ K^{-4}$	Stephan's constant
ξ	μm^{-1}	Differential particle slope parameter
A		Angstrom coefficient
$A(\lambda)$		Absorptance
$B(\lambda)$		Scatterance
B_n	T	Magnetic field
B_L	mg	Difference in blank filter weight
$C(\lambda)$		Atennuance
C_{sca}		Scattering cross section
D	μm	Diameter of spherical particulate material
$E(z, \lambda)$	$W\ cm^{-2}\ nm^{-1}$	Vector irradiance
E_n	$V\ m^{-1}$	Electric field
$E_d(z, \lambda)$	$W\ cm^{-2}\ nm^{-1}$	Downwelling Irradiance
$E_s(z, \lambda)$	$W\ cm^{-2}\ nm^{-1}$	Downwelling incident irradiance
$E_u(z, \lambda)$	$W\ cm^{-2}\ nm^{-1}$	Upwelling irradiance
$I(\theta,\phi)$		Radiant flux Φ per unit solid angle and in a particular direction
$L(z, \lambda)$	$W\ sr^{-1}\ cm^{-2}\ nm^{-1}$	Radiance
$L_u(z,\lambda)$	$W\ sr^{-1}\ cm^{-2}\ nm^{-1}$	Upwelling radiance
$L_w(z,\lambda)$	$W\ sr^{-1}\ cm^{-2}\ nm^{-1}$	Water leaving radiance
N(D)		Number of particles with diameter D
Q	sr	Irradiance-to-radiance ratio
Q_b		Scattering efficiency
Q_{bb}		Backscattering efficiency
$R(z,\lambda)$		Irradiance reflectance
$R_L(z,\lambda)$	sr^{-1}	Radiance reflectance
$Rrs(\lambda)$	sr^{-1}	Remote sensing reflectance
S_d	nm^{-1}	Spectral slope of SPM absorption
S_y	nm^{-1}	Spectral slope of CDOM absorption
T	°C	Temperature
$T(\lambda)$		Transmittance
W_{SF}	mg	Mass on filter
$a(\lambda)$	m^{-1}	Absorption coefficient
$a_{mts}(\lambda)$		Corrected(for temperature and salinity) absorption values of ac-9
$a_{mtsb}(\lambda)$		Corrected(for scattering) absorption values of ac-9
$b(\lambda)$	m^{-1}	Scattering coefficient
$c(\lambda)$	m^{-1}	Attenuance coefficient
$b_f(\lambda)$	m^{-1}	Farward scattering coeffecient
$b_b(\lambda)$	m^{-1}	Backscattering coefficent

$b_p(\lambda)$	m^{-1}	Particulate scattering
$\tilde{b}_b(\lambda)$		Backscattering to scattering ratio (backscattering probability)
$b_b^{SPM}(\lambda)$	m^{-1}	Backscattering due to SPM
$b_b^{SPM*}(\lambda)$	$m^2\ g^{-1}$	Mass-specific scattering coefficient of particles
$b_w(\lambda)$	m^{-1}	Absorption due to water
$b_{bw}(\lambda)$	m^{-1}	Backscattering due to water
$ap(\lambda)$	m^{-1}	Particulate absorption coefficient
$apg(\lambda)$	m^{-1}	Absorption due to particulate and dissolved material
$a_p^*(\lambda)$	$m^2\ g^{-1}$	Mass-specific absorption coefficient of SPM
$a_w(\lambda)$	m^{-1}	Absortion due to water
$a_g(\lambda)$	m^{-1}	Absorption due to CDOM
c	$m\ s^{-1}$	Speed of light
$c_{mts}(\lambda)$		Corrected(for temperature and salinity) attenuation values of ac-9
h	J s	Planks constant
n_a		Index of refraction for air
n_w		Index of refraction for water
V_a	$m\ s^{-1}$	Velocity of light in air
V_w	m s-1	Velocity of light in water
p	$g\ m\ s^{-1}$	Momentum of photon
m		Complex index of refraction
n_s		Real part of index of refraction for particulate matter
n_m		Real part of index of refraction for containment medium
k_s		Imaginary part of index of refraction for particulate matter
k_m		Imaginary part of index of refraction for containment medium
f		Function of ratio of molecular backscattering to total backscattering
$\bar{r}$		Water-air Fresnel reflectance for upwelling irradiance
z	m	depth

Appendix 2: IDL programs

A 2.1 IDL program to compute particulate backscattering probability

```
pro multi_bhmie, filename, output

;=============================================================================
; PROGRAM  : multi_bhmie
; DATE     : May 24,2004
; AUTHOR   : R C NAGUR CHERUKURU, University of Plymouth,
;            r.cherukuru@plymouth.ac.uk
; TASK     : Calculates Particulate backscattering probability using Mie theory
;          - calculates slope of PSD following BOSS etal
;          - models bb and b ratio at ac-9 wavelenghts using mie model
;          - releative refractive index is an avereage of the minerals
;            identified from XRD and organics
;FUNCTIONS:
;          TRANSREAD.PRO to read ASCII coulter counter data.
;          MPFITFUN.PRO (Levenberg-Marquardt least-squares fit - Craig B.
;          Markwardt) to calculate the differential slope of particle size
;          distribution.
;          BHMIE.PRO (Mie computations - P. J. Flatau) to calculate the
;          scattering and backscattering efficiency.
;          F_PSZ.PRO  hyperbolic fit function
; Variables   :
;          xsi          differential particle slope parameter
;          dia          diameter of particle
;          n0           particle number concentration
;          d0           reference diameter
;          nd           number of particles with diameter between D+dD
;          qb           scattering efficiency
;          qbb          backscattering efficiency
;          pa           projected area of the particle
;          xa           size parameter
;          rri          relative refractive index
;          b_sca        particulate scattering
;          b_back       particulate backscattering
;          bb_b         ratio of particulate backscattering to scattering
;=============================================================================

common slp,n0,d0
common fnm,fslp

openu,1,filename                              ;input file name

if (output eq 1) then begin
openu,2,'/home/nagur/cdrom/opt_mod/'+'bb_b.dat',/append ; output file name
endif
```

```
; Read coulter counter ASCII files

sl=0d & dia=0d & num=0d & vol=0d & area=0d
transread,1,sl,dia,num,vol,area,format='(d0.0,d0.0,d0.0,d0.0,d0.0)'

; Calculation of ξ from coulter counter data

r22=where(num gt 0.0)
sz1=size(r22,/n_elements)
j=0
nd=dblarr(sz1)
for i=0,sz1-2 do nd(j++)=num(r22(i))/(dia(r22(i+1))-dia(r22(i)))

n0=nd(fix(sz1/2))                          ; used in f_psz via common slp
d0=dia(r22(fix(sz1/2)))                    ; used in f_psz via common slp

xx=dia(r22)
yy=nd

rerr=1.0                                   ; weights for error bars
A=3.0d                                     ; inital guess of xsi
xsi=MPFITFUN('f_psz',xx,yy,rerr,A)         ; differential slope parameter xsi

; Calculation of number of particles in every one micron

cnt=intarr(100)
for io=0,100-1 do begin
        tt=where((dia gt io and dia lt io+1)and (num ne 0),count)
        cnt(io)=count
endfor
cf=indgen(100)
res6=LADFIT(alog(cf[3:20]),alog(cnt[3:20]))

; Diameter distribution between 1-2 and 2-3 micron

rc=fltarr(3)
for tk=1,2 do rc(tk)=fix((tk^res6[1])*exp(res6[0]))          ;Power law
rc(0)=fix((0.1^res6[1])*exp(res6[0])); this is to calculate num of possible
                                           ;diameters between 0.1 micron and 1.0 micron

;Extrapolating the diameter range

; 0.1 to 1.0 micron
dia1=fltarr(rc(0))
for io=0,rc(0)-1 do dia1(io)=0.0+(1.0/rc(0))*io

;1 -2 micron
```

```
dia2=fltarr(rc(1))
for io=0,rc(1)-1 do dia2(io)=1.0+(1/rc(1))*io

;2-3 micron
dia3=fltarr(rc(2))
for io=0, rc(2)-1 do dia3(io)=2.0+(1/rc(2))*io

sz=size(dia)
r1=where(dia1 lt min(dia(r22)))
r2=where(dia2 lt min(dia(r22)))
r3=where(dia3 lt min(dia(r22)))

; Combining extrapolated and coulter counter data

dia4=[dia1(r1),dia2(r2),dia3(r3)]; extrapolated diamenters less than  min_of_dia(r22)
d22=[dia4,dia(r22)]                ; concatenation of extrapolated and CC diameters

; Calculation of new nd using the entire particle range
r4=where(d22 gt 0.0)
d2=d22(r4)

nd_new=n0*(d2/d0)^(-1*xsi)

;Create arrays for Qb and Qbb

qb=fltarr(size(d2,/n_elements))
qbb=fltarr(size(d2,/n_elements))

; calculation of particle projected area

pa=(3.14/4)*((d2/10^6)^2)          ; diameter expressed in meters

; Average RRI= RRI of Kaolinite, Muscovite, Quartz, Chlorite, Albite, Orthoclase and
;organics, Mineral RRI Babin et al., (2003a) and Optical Mineralogy, Nesse (2001)

rri=1.1506143                      ; avg rri of mineral plus organic matter

b_back=dblarr(9)
b_sca=dblarr(9)

wave_l=[412,440,488,510,555,630,650,676,715]
for iw=0,8 do begin

        ; Calculation of Size parameter

        xa=(3140/(wave_l(iw)))*(d2)  ; 3140 is the conversion factor for wavelength
                                     ; and diameter

        nang=90
```

```
; Call BHMIE.PRO for Qbb and Qb calculation

for jj=0,size(d2,/n_elements)-1 do begin
        bhmie,xa(jj),rri,nang,s1,s2,qext,qsca,qback,gsca
        qbb(jj)=qback           ; backscattering efficiency
        qb(jj)=qsca             ; scattering efficiency
endfor

d21=size(d2,/n_elements)-1

        ; Scattering and backscattering computations

        bb_p=qbb*pa*nd_new
        b_p=qb*pa*nd_new

        d2_2=where(d2 gt 0.0)

        b_sca(iw)=int_tabulated(d2(d2_2),b_p(d2_2))       ; integration
        b_back(iw)=int_tabulated(d2(d2_2),bb_p(d2_2))     ; integration

endfor;

; Calculation of probability of backscattering

bb_b=b_back/b_sca ;

; Print backscattering probability values into output file

printf,2,filestem,xsi,bb_b(0),bb_b(1),bb_b(2),bb_b(3),bb_b(4),bb_b(5),$
,bb_b(6),bb_b(7),bb_b(8),format='(A0,",",d0.0,",",d0.0,",",d0.0,",",d0.0,",",$
,d0.0,",",d0.0,",",d0.0,",",d0.0,",",d0.0,",",d0.0)'

close,/all                      ; close all files

end                             ; end of program
```

A 2.2 IDL program to compute Radiance reflectance and Remote sensing reflectance from ac-9 measurements

```
pro reflectance
;=============================================================================
; PROGRAM  : reflectance
; DATE     : May 24,2004
; AUTHOR   : R C NAGUR CHERUKURU, University of Plymouth,
;            r.cherukuru@plymouth.ac.uk
; TASK     : Calculates Radiance reflectance and Remote sensing reflectance
;FUNCTIONS :
;            TRANSREAD.PRO to read CSV ac-9  data.
;            MPFITFUN.PRO (Levenberg-Marquardt least-squares fit - Craig B.
;            Markwardt) to calculate the attenuation slope
; VARIABLES:
;       xsi                 differential particle slope parameter
;       a412-a715           absorption from ac-9
;       c412-c715           attenuation from ac-9
;       b412-b715           scattering from ac-9
;       fq412-fq715         f/Q from LUT
;       aw412-aw715         water absorption at ac-9 wavelengths Pope and Fry(1997)
;       bbw412-bbw715       backscattering from Morel(1974)
;       gma2                Slope of particulate attenuation
;       rL412-rL715         Radaince reflectance
;       rrs412-rrs715       Remote sensing reflectance
;=============================================================================

;Open to read ac-9 data for absorption and scattering

openr,1,'/home/nagur/cdrom/opt_mod/ac9_csv/hydro_ab.csv'

; Open output file

openw,2,'/home/nagur/cdrom/opt_mod/rrs_1m2.csv',/append

;Read ac-9 data

date=" & time=" & dep=" & lon=0d & lat=0d & depth=0d
a412=0d & a440=0d & a488=0d & a510=0d & a555=0d
a630=0d & a650=0d & a676=0d & a715=0d
c412=0d & c440=0d & c488=0d & c510=0d & c555=0d
c630=0d & c650=0d & c676=0d & c715=0d

transread2,1,date,time,lon,lat,depth, c412,c440,c488,c510,c555,c630,c650,c676, $
c715, a412,a440,a488,a510,a555,a630,a650,a676,a715, $
format='(A10,A9,d0.0,d0.0,I0,d0.0,d0.0,d0.0,d0.0,d0.0,d0.0,d0.0,d0.0,d0.0,d0.0,d0.0,
d0.0,d0.0,d0.0,d0.0,d0.0,d0.0,d0.0)'
```

```
;Calculation of scattering from ac-9 attenuation and absorption

b412=c412-a412
b440=c440-a440
b488=c488-a488
b510=c510-a510
b555=c555-a555
b630=c630-a630
b650=c650-a650
b676=c676-a676

wave_l=[412,440,488,510,555,630,650,676,715]; ac-9 wavelengths

;Calculation of f/Q values using ac-9 a and b with Look-up Table (Moore et al., 1999)

x=set_geom(45*!dtor,0,0)

dc=where(depth gt 0.0 and depth lt 1.5)

for i=0,size(dc,/n_elements)-1 do begin       ;Loop for different depths and samples

        fq412=f_ab(a412(dc(i)),b412(dc(i)),0)
        fq440=f_ab(a440(dc(i)),b440(dc(i)),1)       ; ac-9 (440) = SPMR (443)
        fq488=f_ab(a488(dc(i)),b488(dc(i)),1)       ; ac-9 (488) = SPMR (490)
        fq510=f_ab(a510(dc(i)),b510(dc(i)),3)
        fq555=f_ab(a555(dc(i)),b555(dc(i)),4)
        fq676=f_ab(a676(dc(i)),b676(dc(i)),5)       ; ac-9 (676) = SPMR (670)

        ; Interpolation for red and infrared  wavelengths

        res=ladfit([555,670],[fq555,fq676])
        fq630=res(0)+res(1)*630
        fq650=res(0)+res(1)*650
        fq715=res(0)+res(1)*715

        ; Calculation of attenuation slope from ac-9 attenuation values

att=[c412(dc(i)),c440(dc(i)),c488(dc(i)),c510(dc(i)),c555(dc(i)),c630(dc(i)),c650(dc(i)),c676(
dc(i))]

        c_slope=LADFIT(alog(wave_l(0:7)),alog(att)); initial guess for att. slope
        rerr=1.0
        gma=mpfitfun('att_fit',wave_l,att,rerr,c_slope)       ;Levenberg-Marquardt
                                                              ;least-squares fit
        gma2=0.7227*gma(1)+0.0186       ; gamma equation for gamma_ag
                                        ; compensation
        gma(1)=gma2

        ; Calculation of differential slope parameter xsi
```

xsi=gma2+3-0.5*exp(-6*gma2); *psd slope*

; Calculation of backscattering probability using differential slope
; parameter(Chapter5, Section 2)

bb_prob412=0.0059*(xsi^3)-0.0561*(xsi^2)+0.1578*xsi-0.1002
bb_prob488=0.0075*(xsi^3)-0.0766*(xsi^2)+0.2446*xsi-0.2231
bb_prob555=0.0028*(xsi^3)-0.0215*(xsi^2)+0.0331*xsi+0.0438
bb_prob630=-0.0008*(xsi^3)+0.0206*(xsi^2)-0.1279*xsi+0.2441

a=[a412(dc(i)),a440(dc(i)),a488(dc(i)),a510(dc(i)),a555(dc(i)),a630(dc(i)),
a650(dc(i)),a676(dc(i)),a715(dc(i))]
b=[b412(dc(i)),b440(dc(i)),b488(dc(i)),b510(dc(i)),b555(dc(i)),b630(dc(i)),
b650(dc(i)), b676(dc(i)),b715(dc(i))]

; Calculation of backscattering from ac-9 scattering values

bb412=bb_prob412*b412(dc(i))
bb440=bb_prob412*b440(dc(i))
bb488=bb_prob488*b488(dc(i))
bb510=bb_prob488*b510(dc(i))
bb555=bb_prob555*b555(dc(i))
bb630=bb_prob630*b630(dc(i))
bb650=bb_prob630*b650(dc(i))
bb676=bb_prob630*b676(dc(i))
bb715=bb_prob630*b715(dc(i))

bb=[bb412,bb440,bb488,bb510,bb555,bb630,bb650,bb676,bb715]

;Backscattering of pure water Morel 1974

bbw=0.5*(0.00288*(wave_l/500.0)^(-4.32))

;Pure water absorption Pope and Fry (1997)

aw412=0.00452 & aw440= 0.00635 & aw488=0.0144 & aw510=0.0325 &
aw555=0.0565 & aw630=0.2916 & aw650=0.34 & aw676=0.448 & aw715=1.007

aw=[aw412,aw440,aw488,aw510,aw555,aw630,aw650,aw676,aw715]

;Calculation of IOP ratio (bb/a+bb)

r412=(bb412+bbw(0))/(a412(dc(i))+aw412+bb412+bbw(0))
r440=(bb440+bbw(1))/(a440(dc(i))+aw440+bb440+bbw(1))
r488=(bb488+bbw(2))/(a488(dc(i))+aw488+bb488+bbw(2))
r510=(bb510+bbw(3))/(a510(dc(i))+aw510+bb510+bbw(3))
r555=(bb555+bbw(4))/(a555(dc(i))+aw555+bb555+bbw(4))
r630=(bb630+bbw(5))/(a630(dc(i))+aw630+bb630+bbw(5))
r650=(bb650+bbw(6))/(a650(dc(i))+aw650+bb650+bbw(6))

```
r676=(bb676+bbw(7))/(a676(dc(i))+aw676+bb676+bbw(7))
r715=(bb715+bbw(8))/(a715(dc(i))+aw715+bb715+bbw(8))

;Calculation of Radiance reflectance from ac-9 measurements
; (Chapter 5, Section 2)

rL412=fq412*r412
rL440=fq440*r440
rL488=fq488*r488
rL510=fq510*r510
rL555=fq555*r555
rL630=fq630*r630
rL650=fq650*r650
rL676=fq676*r676
rL715=fq715*r715
rL=[rL412,rL440,rL488,rL510,rL555,rL630,rL650,rL676,rL715]

;Calculation of Remote sensing reflectance(Chapter 5, Section 2)

rrs412=(0.54)*(1/(1-0.48*0.52*r412))*fq412*r412
rrs440=(0.54)*(1/(1-0.48*0.52*r440))*fq440*r440
rrs488=(0.54)*(1/(1-0.48*0.52*r488))*fq488*r488
rrs510=(0.54)*(1/(1-0.48*0.52*r510))*fq510*r510
rrs555=(0.54)*(1/(1-0.48*0.52*r555))*fq555*r555
rrs630=(0.54)*(1/(1-0.48*0.52*r630))*fq630*r630
rrs650=(0.54)*(1/(1-0.48*0.52*r650))*fq650*r650
rrs676=(0.54)*(1/(1-0.48*0.52*r676))*fq676*r676
rrs715=(0.54)*(1/(1-0.48*0.52*r715))*fq715*r715

rrs=[rrs412,rrs440,rrs488,rrs510,rrs555,rrs630,rrs650,rrs676,rrs715]

; Print radiance reflectance to output file

printf,2,date(dc(i)),dep(dc(i)),time(dc(i)),lat(dc(i)),lon(dc(i)),depth(dc(i)),gma2,xsi, $
rL412,rL440,rL488,rL510,rL555,rL630,rL650,rL676,rL715, $
format='(A0,A0,A0,",",d0.0,",",d0.0,",",d0.0,",",d0.0,",",d0.0,",",d0.0,",",d0.0,",",d0.0
,",",d0.0,",",d0.0,",",d0.0,",",d0.0,",",d0.0,",",d0.0)

;Option to print Remote sensing reflectance

printf,2,date(dc(i)),time(dc(i)),lat(dc(i)),lon(dc(i)),depth(dc(i)),gma2,xsi,rrs412, $
rrs440,rrs488,rrs510,rrs555,rrs630,rrs650,rrs676,rrs715, $
format='(A0,A0,d0.0,",",d0.0,",",d0.0,",",d0.0,",",d0.0,",",d0.0,",",d0.0,",",d0.0,",",d0.
0,",",d0.0,",",d0.0,",",d0.0,",",d0.0,",",d0.0)

endfor                    ; Endfor (samples/depths)

close, /all               ; close all files

end                       ; end of program
```

A 2.2.1 IDL Function to calculate Differential slope parameter

```
function f_psz,x,A
;=============================================================
; FUNCTION   : f_psz.pro
; TASK       : Differential slope parameter calculation
; AUTHOR     : RC NAGUR CHERUKURU
;=============================================================

common slp, n0,d0 ; variables from reflectance.pro

ndn=n0*((x/d0)^(-1*A))

return, ndn

end
```

A 2.2.2 IDL Function to calculate Spectral attenuation slope

```
function att_fit,x,ft
;=============================================================
; FUNCTION  : att_fit.pro
; TASK      : Spectral particulate attenuation slope calculation
; AUTHOR    : RC NAGUR CHERUKURU
;=============================================================

cp=ft(0)*x^(-ft(1))

return,cp

end
```

A 2.3 IDL program to simulate IOP ratio

```
pro simulation,output
;=============================================================================
; PROGRAM  : simulation.pro
; DATE     : May 24,2004
; AUTHOR   : R C NAGUR CHERUKURU, University of Plymouth,
;            r.cherukuru@plymouth.ac.uk
; TASK     : Simulation of IOP ratio
; Variables :
;       ap              particulate absorption
;       ay              CDOM absorption
;       bb_mod          Spectral backscattering
;       aw412-aw715     water absorption at ac-9 wavelengths Pope and ;
                        Fry(1997)
;       bbw412-bbw715   backscattering from Morel(1974)
;       SPM             SPM concentration (mg/l)
;       bb_gma          Slope of spectral particulate backscattering
;       Sy              Slope of CDOM absorption
;       Sd              Slope of particulate absorption
;       rrs             Remote sensing reflectance
;=============================================================================

close,/all

; Open output file


if (output eq 1) then begin
openw,2,'d:/pml_sample/results_opt_model/simulation33_ap_err.csv'
endif

cnt=0

; Simulation wavelengths


wave_l=[412,440,488,510,555,630,650,676,715]

;Absorption due to water Pope and Fry (1997)


aw412=0.00452 & aw440= 0.00635 & aw488=0.0144 & aw510=0.0325 &
aw555=0.0565
aw630=0.2916 & aw650=0.34 & aw676=0.448 & aw715=1.007
aw=[aw412,aw440,aw488,aw510,aw555,aw630,aw650,aw676,aw715]

;Spectral backscattering Morel (1974)
```

```
bbw=0.5*(0.00288*(wave_l/500.0)^(-4.32));
bb_gm=0.6                    ; Option to change slope of spectral backscattering

;Options to include and modify CDOM absorption

ay440=0.3
sy=0.014
ay_in=1.0       ; Option to include CDOM  absorption 1-Yes, 0-No
;Options to include and modify particulate absorption

sd=0.01
ap_in=1.0       ; option to include particulate absorption 1-Yes, 0-No

cnt=0

; For loop to change the concentration of SPM

for spm=0.5,12.0,0.5 do begin

        cnt=cnt+1

        ;Spectral backscattering model (Chapter 5, Section II)

        bb_mod=(0.006*spm+0.0019)*(wave_l/630.0)^(-bb_gm)

        ;Absorption due to CDOM (Chapter 5, Section II)

        ay=ay440*exp(-sy*(wave_l-440))
        ay=ay-ay(8)
        ay=ay*ay_in

        ;Particulate absorption model (Chapter 5, Section II)

        ap=(0.0512*spm+0.0393)*(exp(-sd*(wave_l-412)))
        ap=ap*ap_in

        ;IOP ratio(Chapter 5, Section II)

        ratio_mod=(bbw+bb_mod)/(aw+ay+ap+bbw+bb_mod)

        Plot,wave_l,ratio_mod

        PRINTF,2,spm,bb_gm,ay440,sy,sd,ratio_mod(0),ratio_mod(1), $
        ratio_mod(2),ratio_mod(3),ratio_mod(4),ratio_mod(5),ratio_mod(6), $
        ratio_mod(7),ratio_mod(8), $
        format='(d0.0,",",d0.0,",",d0.0,",",d0.0,",",d0.0,",",d0.0,",",d0.0,",",d0.0,",",
        d0.0,",",d0.0,",",d0.0,",",d0.0,",",d0.0,",",d0.0)'

endfor                  ; SPM loop
end                     ; end of program
```

References

Adamenko, V.n., Kondratyev, K.Ya., Pozdnyakov, D.V., and Chekhin, L.P. (1991). Radiative Regime and Optical Properties of Lakes, Gidrometeoizdat Publishing Co., Leningrad, 300.

Arrigo, K.R. and Brown, C.W. (1996). Impact of chromophoric dissolved organic matter on UV inhibition of primary productivity in the sea. *Mar. Eco. Prog. Ser.* 140, 207-216.

Audouze, J. and Vauclair, S. (1980). An introduction to nuclear astrophysics. D. *Reidel publishing company*, 51-54.

Babin, M., A. Morel, V. Fournier-Sicre, F. Fell and D. Stramski (2003a). Light scattering properties of marine particles in coastal and oceanic waters as related to the particle mass concentration. *Limnol. Oceanogr.*, 48, 843-859

Babin, M., Stramski, D. Ferrari, G.M., Claustre, H., Bricaud, A., Obolensky, G., and N. Hoepffner (2003b). Variations in the light absorption coefficients of phytoplankton, non-algal particles, and dissolved organic matter in coastal waters around Europe. *J. Geophys. Res.*, 108,C7, 3211-3232.

Blough, N. V., Zafiriou, O. C., and Bonilla, J. (1993). Optical absorption spectra of waters from the orinoco river outflow: Terrestrial input of colored organic matter to the Caribbean. *J. Geophys. Res.*, 98, 2271-2278.

Blough, N.V. (2001). Photochemical Processes. In: Encyclopedia of Ocean Sciences (J.Steele, S. Thorpe and K. Turekian, Eds.), *Academic Press*, 2162-2172.

Blough, N.V. and Vecchio, R.D. (2002). Biogeochemistry of Marine dissolved organic matter, Edited by: Hansell, D.A. and Carlson, C.A. *Academic Press* 509-546

Blough, N.V. and Zepp, R.G. (Eds). (1990). Effects of solar ultraviolet radiation on biogeochemical dynamics in aquatic environments, Woods Hole Oceanographic Institution Technical report, WHOI-90-09.

Blough, N.V. and Zepp, R.G. (1995). Reactive oxygen species in natural waters. In *Active oxygen: Reactive oxygen species in chemistry*, Foote, C.S. et al. (eds), Chapman and Hall, 280-333.

Bohren, C.F. and Huffman, D.R. (1983). Absorption and Scattering of light by small particles, *J.Wiley and Sons*, New York, 530.

Boss, E., Pegau, W.S., Gardner, W.D., Zaneveld, J.R.V., Barnard, A.H., Twardowski, M.S., Chang, G.C. and Dickey,T.D. (2001). Spectral particulate attenuation and particle size distribution in the bottom boundary layer of a continental shelf. *J. Geophys. Res.*, 105(C5), 9509-9516.

Boss, E., Twardowski, M.S., and Herring, S. (2001). Shape of the particulate beam attenuation spectrum and its inversion to obtain the shape of particulate size distribution. *Appl. Opt.*, 40 (27), 4885-4893.

Bowers,D.G., Harker, G.E.L, and Stephan, B. (1996). Absorption spectra of inorganic particles in the Irish sea and their relevance to remote sensing of chlorophyll. *Int. Jour. of Rem. Sen.*, 17(12), 2449-2460.

Bricaud, A., Morel, A. and Prieur, L. (1981). Absorption by dissolved organic matter of the sea (yellow substance) in the UV and visible domains, *Limnol. Oceanogr.*, 26, 43-53.

Bukata, R.P., Jerome, J.H., Kondratyev, K.Y. and Pozdnyakov, D.V. (1995).Optical Properties and Remote sensing of Inland and Coastal Waters. *CRC Press*, 115-133.

Butler, W.L, Katajima,M. (1975). A tripartite model for chloroplast fluorescence. In: Avron, M, ed. Third interm. Congress on Photosynthesis. Amstradam: *Elsevier*, 13-24.

Carder, K.L., Steward, R.G., Harvey, G.R. and Ortner, P.B. (1989). Marine humic and fulvic acids: Their effects on remote sensing of ocean chlorophyll. *Limnol. Oceanogr.*, 34, 68–81.

Chang, G.C., Dickey, T.D., Mobley, C.D., Boss, E. and Pegau, W.S. (2003). Toward clouser of upwelling radiance in coastal waters. *Appl. Opt.*, 42(9), 1574-1582.

Chen, R.F. and Bada, J.L. (1992). The fluorescence of dissolved organic matter in seawater, *Marine. Chemistry.* 37, 191–221.

COLORS. (2001). Final report: COastal region LOng-term measurements for colour Remote Sensing development and validation.

Conde, D., L. Aubriot, L., Sommaruga,R. (2000). Changes in UV penetration associated with marine intrusions and freshwater discharge in a shallow coastal lagoon of the southern Atlantic Ocean. *Mar. Ecol. Prog. Ser.*, 207, 19-31.

De Souza Sierra, M.M., Donard, O.F.X. and Lamotte, M. (1997). Spectral identification and behaviour of dissolved organic fluorescent material during estuarine mixing processes. *Mar. Chem.* 58, 51–58.

De Souza Sierra, M.M., Donard, O.F.X., Lamotte, M., Belin, C. and Ewald, M. (1994). Fluorescence spectroscopy of coastal and marine waters. *Mar. Chem.* 47, 127–144.

Donard, O.F.X., Lamotte, M., Belin, C. and Ewald, M. (1989). High-sensitivity fluorescence spectroscopy of Mediterranean waters using a conventional or a pulsed laser excitation source. *Mar. Chem.* 27, 117–136.

Doerffer, R. (1992). Imaging Spectroscopy for Detection of Chlorophyll and Suspended Matter. GKSS 92/E/54.

Droppo, I. G. (2001). Rethinking what constitutes suspended sediment. *Hydrological Processes* 15, 1551–1564.

Esima, D. (1993). Suspended matter in the Aquatic environment. *Springer-Verlag.*

Falkowski, P.G. and J. Raven. (1997). Aquatic Photosynthesis, Blackwell, *Oxford* 375.

Fargion, G.S. and Mueller, J.L. (2000) Ocean Optics Protocols For Satellite Ocean Color Sensor Validation, Revision 2. NASA/TM-2000-209966.

Ferrari, G. M. (2000). The relationship between chromophoric dissolved organic matter and dissolved organic carbon in the European Atlantic coastal area and in the west Mediterranean Sea (Gulf of Lions), *Mar. Chem.*, 70, 339– 357.

Feynman, R.P., Leighton, R.B. and Sands, M. (1966). The Feynman lectures on physics (*Mainly electromagnetism and matter*). *Addison-Wesley*, Reading, Massachusetts. 18.1 – 28.14.

Findlay, S. and Sinsabaugh R.L. (1999). Unravelling the sources and bioavailability of dissolved organic matter in lotic aquatic ecosystems. *Mar. Freshwater Res.*, **50**, 781–790.

Flatau, P.J. (1996). Mie scattering IDL code, http://atol.ucsd.edu/~pflatau/

Gallie, E.A and Murtha, P. A. (1992). Specific absorption and backscattering spectra for suspended minerals and Chlorophyll-a in chilko Lake, British Columbia. *Rem. Sen. Envi.*, 39, 103-118.

Gibbs, R.J. (1977). Transport phases of transition metals in the Amazon and Yukon rivers. *Bull. Geol. Soc. Am.* 88,829-843.

Gordon, H.R., Brown, O.B., Evans, R.H., Brown, J.H., Smith, R.C., Baker, K.S. and Clark, D. K. (1988). A Semianalytic Radiance Model of Ocean Color. *J. Geophys. Res.*, 93(D9), 10909-10924.

Gordon,H,J., Brown,O.B., and Jacobs, M.M. (1975) "Computed relationships between the inherent and apparent optical properties of a flat homogeneous ocean," *Appl. Opt.* 14, 417-427

Green, S.A. and Blough, N.V. (1994). Optical absorption and fluorescence properties of chromophoric dissolved organic matter in natural waters. *Limnol. Oceanogr.* 39, 1903–1916.

Gustafsson, O. & Gschwend, P. M. (1997). Aquatic colloids: concepts, definitions and current challenges. *Limnol. Oceanogr.*, 42, 519–528.

Häder, D.P., Kumar, H.D., Smith, R.C., and Worrest, R.C. (1998). Effects on aquatic ecosystems, Journal *of Photochemistry and Photobiology B-Biology*, 46 (1-3), 53-68.

Helz, G.R., Zepp, R.G. and Crosby, D.(Eds.). (1994). Aquatic and Surface Photochemistry, *CRC/Lewis Publishers*, Boca Raton, FL, 552, 100.

Herbelin, S.E. (1994). 'Photophysics and photochemistry of natural waters with emphasis on radical probe development and application'. MS Thesis, MIT/WHOI.

Hoge, F.E., Williams, M.E., Swift, R.N., Yungel, J.K. and Vodacek, A. (1995). Satellite retrieval of the absorption coefficient of chromophoric dissolved organic matter in continental margins. *J. Geophys. Res.*, 100, 24,847–24,854.

Højerslev N.K. (1988). Natural occurrences and optical effects of Gelbstoff Kobenhavns Universitet Geofysisk Inst. Rep no. 50, pp 29.

Højerslev N.K., Aas E. (2001). Spectral light absorption by yellow substance in the Kattegat-Skagerrak area, *Oceanologia*, 43 (1), 39–60.

IOCCG. (2000). Remote Sensing of Ocean Colour in Coastal, and Other Optically-Complex, Waters (Report number: 3).

Jeffrey S.W., Montoura, R.F.C., Wright, S.W. (1997). Phytoplankton pigments in oceanography guidelines to modern methods, UNESCO

Jenkins, F.A. and Harvey, W.E. (1957). Fundamentals of Optics. *McGraw-Hill Book Company*, 536-540.

JGOFS. (1994). Protocols for the Joint Global Ocean Flux Study Core Measurements. Intergovernmental Oceanographic Commission, Scientific Committee on Oceanic Research. Manual and Guides, UNESCO. 29, 91-96.

Kerker, M. (1969). The scattering of Light and other Electromagnetic Radiation. *Academic Press*, New York, 66.

Kirk, J.T.O. (1984). Dependence of relationship between inherent and apparent optical properties of water on solar altitude. *Limnol. Oceanogr.* 29, 350-356.

Kirk, J.T.O. (1991). Volume scattering function, average cosines, and the underwater light field. *Limnol. Oceanogr.* 36, 455-467

Kirk, J.T.O. (1994). Light and Photosynthesis in Aquatic Ecosystems, *Cambridge University Press*, 2nd ed.

Kitchen, J.C., Zaneveld, J.R.V and Pak, H. (1982). Effect of particle size distribution and chlorophyll content on beam attenuation spectra, *Appl. Opt.*, 21, 3913-3918.

Kouassi, A.M. and Zika, R.G. (1992). Light-induced destruction of the absorbance property of dissolved organic matter in seawater, *Toxicol. Environ. Chem*, 35, 195-211.

Kouassi, M., Zika, R.G., and Plane, J.M.C.(1990). Photochemical modelling of marine humus fluorescence in the ocean. *Neth. J. Sea Res.*, 27, 33-41.

Krane, K.S. (1996). Modern Physics. New York ; Chichester : *Wiley*.

Lakovicz, J.R. (1983). 'Principle of Fluroscence Spectroscopy', 1st ed. *Plenum Press*, New York.

Lang, K.R (1995). Sun, Earth and Sky. *Springer*. 25-28.

Luthy, R. G., Aiken, G. R., Brusseau, M. L., Cunningham, S. D., Gschwend, P. M., Pignatello, J. J., Reinhard, M., Traina, S. J., Weber, W. J. Jr. & Westall, J. C. (1997). Sequestration of hydrophobic organic contaminants by geosorbents. *Environmental Science and Technology*, 31, 3341–3347.

Mobley, C. D. (1994). Light and Water, Radiative Transfer in Natural Waters. *Acedemic Press*, Elsevier Science(USA), 77-80.

Moore, G.F., Aiken, J and Lavender, S.J.(1999). The atmospheric correction of water color and the quantitative retrieval of suspended particulate matter in Case II waters: application to MERIS. *Int. Jour. of Rem. Sen.*, 20(9), 1713-1733.

Mopper, K. and Kieber, D. J. (2002). Photochemistry and the cycling of carbon, sulfur, nitrogen and phosphorus. *In:* "Biogeochemistry of Marine Dissolved Organic Matter" Chapter 9. D. Hansell and C. Carlson, (Eds.), *Academic Press*, 455-489.

Moran, M. A., Sheldon, W. M. and Zepp, R. G. (2000). Carbon loss and optical poperty changes during long-term photochemical and biological degradation of estuarine dissolved organic matter. *Limnol. Oceanogr.* 45, 1254-1264.

Moran, M.A. and Zepp, R.G. (1997). Role of photoreactions in the formation of biologically labile compounds from dissolved organic matter. *Limnol. Oceanogr.*, 42, 1307-1316.

Morel, A and Prieur, L. (1977). Analysis of variations in ocean color. *Limnol. Oceanogr.*, 22, 709-721.

Morel, A. (1974). Optical properties of pure water and pure seawater. In: Jerlov & E. Steeman Nielsen (eds.). Optical aspects of oceanography. *Academic press*, 1-24

Morel, A. and Gentili, B. (1991). Diffuse reflectance of oceanic waters: its dependence on sun angle as influenced by the molecular scattering contribution. *Appl. Opt.*, 30, 4427-4438.

Morel, A., (1973). Diffusion de la lumiere par les eaux de mer: Resultata experimentaux et approche theorique, in AGARD *Lect. Ser.*, 61, 3.1.1-3.1.76.

Mueller, J.L., and Austin, R.W. (1992). Ocean Optics Protocols for SeaWiFS Validation. NASA Tech. Memo. 104566, Vol. 5, S.B. Hooker and E.R. Firestone, Eds., NASA Goddard Space Flight Center, Greenbelt, Maryland, 43 .

Neale, P. J. and D. J. Kieber. (2000). Assessing biological and chemical effects of UV in the marine environment: Spectral weighting functions. *In* R. E. Hester and R. M. Harrison [eds.], Causes and Environmental Implications of Increased U.V.-B. Radiation. Royal Society of Chemistry. *Issues in Environmental Science and Technology*, 14, 61-83.

Nesse, W.D. (2000). Introduction to mineralogy. *Oxford University Press*. 39-158.

Pegau, W.S. and J. R. V. Zaneveld. (1993). Temperature dependent absorption of water in the red and near infrared portions of the spectrum, *Limnol. Oceanogr.*, 38, 188-192.

Petzold, T.J., (1972). Volume scattering functions for selected ocean waters, SIO Ref. 72-78, Scripps Inst. Oceanogr., La Jolla, 79 pp. Condensed as Chapter 12 in *Light in the Sea*, Edited by J.E. Tyler, Dowden, Hutchinson & Ross, Stroudsberg, 1977, 150-174.

Pierson, D.C. and Strömbeck, N. (2001). Estimation of Radiance Reflectance and the Concentrations of Optically active substances in Lake Malaren, Sweden based on direct and inverse solutions of a simple model. *Science of Total Environment,* 268, 171-188.

Pope, R.M. and Fry, E.S. (1997). Absorption spectrum (380-700 nm) of pure water II. Integrating cavity measurements. *Appl. Opt.*, 36(33), 8710 - 8723.

Raman, C.V. (1922). On molecular scattering of light in water and the colour of the sea. *Proc. Royal Acad.* London, A, 101, 64-80.

Risović, D. (2002). Effect of suspended particulate-size distribution on the backscattering ratio in the remote sensing of sea water. *Appl. Opt.*,41(33),7092-7101.

Shuleikin, V.V. (1922). On the color of the sea. Izv. *Inst. Phys. Biophys.*, 2, 119-136.

Sieburth, J. McN. and Jensen, A. (1968) Studies on algal substances in the sea. I. Gelbstoff (humic material) in terrestrial and marine waters. *J. Exp. Mar. Biol. Ecol.*, 2, 174-189.

Sieburth, J.McN. and Jensen, A. (1969). Studies on algal substances in the sea. II. The formation of gelbstoff (humic material) by exudates of phaeophyta. *J. Exp. Mar. Biol. Ecol.*, 3: 275-289.

Smith, R. C., and Baker, K. S. (1981) Optical properties of the clearest natural waters (200–800 nm), *Appl. Opt.*, *20*, 177–184

Spitzy, A. and V. Ittekot (1986). Gelbstoff: an uncharacterized fraction of dissolved organic carbon. In: The influence of yellow substance on remote-sensing of seawater-constituents from space, 2, GKSS Geesthacht Research Center, Geesthacht, Germany, 1-31.

Stedmon, C.A., Markager, S., Kaas, H. (2000). Optical properties and signatures of chromophoric dissolved organic matter (CDOM) in Danish coastal waters. *Estuarine, Coastal and Shelf Science, 51,* 267-278.

Stramski, D. and Kiefer, D.A. (1991). Light scattering by micro organisms in the open ocean. *Prog. Oceanog.*, 28, 343-383.

Strömbeck, N. and Pierson, D.C. (2001). The effects of variability in the inherent optical properties on estimations of chlorophyll *a* by remote sensing in Swedish waters. *The Science of Total Environment,* 268, 123-137.

Tassan, S., and Ferrari, G. M. (1995). An alternative approach to absorption measurements of aquatic particles retained on filters, *Limnol. Oceanogr.,* 40, 1358 – 1368.

Tilstone, G.H. and Moore G.F. (2002). Regional Validation of MERIS Chlorophyll products in North Sea coastal waters, EVG1-CT-2001-0049.

Turner, A. and Millward, G.E. (2002). Suspended Particles: Their Role in Estuarine Biogeochemical cycles. *Estuarine, Coastal and Shelf Science,* 55, 857-883.

Tipler, P.A. (1999). Physics for scientists and Engineers. W.H.Freeman and company.

Twardowski, M.S., and Donaghay, P.L. (2001). Separating *in situ* and terrigenous sources of absorption by dissolved material in coastal waters. *J. Geophys. Res.*, 106(C2), 2545-2560.

Twardowski, M.S., Boss, E., Macdonald, J.B., Pegau, W.S., Barnard, A.H and Zaneveld, J.R.V. (2001). A model for estimating bulk refractive index from the optical backscattering ratio and the implications for understanding particle composition in case I and case II waters. *J. Geophys. Res.*, 106(C7), 14129-14142.

UNESCO. (1981). Background papers and supporting data on the International Equation of state of Seawater 1980. Report:38.

UNESCO. (2003). The Integrated Strategic design Plan for Coastal ocean observations Module of Global Ocean Observing System, 33-49.

Van de Hulst, H.C. (1981). Light scattering by small particles. *Dover Publications Inc.*, New York.

Van der Linde, D. (1998). Protocol for Total Suspended Matter estimate. *JRC Technical Note*

Vodacek, A., Degrandpre, M.D., Peltzer, E.D., Nelson, R.K. and Blough, N.V. (1997). Seasonal variation of CDOM and DOC in the Middle Atlantic Bight: terrestrial inputs and photooxidation. *Limnol. Oceanogr.*, 42, 674-686.

Vodacek, A., Hoge, F. E., Swift, R. N., Yungel, J. K., Peltzer, E. T., and Blough N. V. (1995). The use of *in situ* and airborne fluorescence measurements to determine UV absorption coefficients and DOC concentration in surface waters, *Limnol. Oceanogr.*, 40, 411-415.

Volz,F. (1954). Die Optik und Meteorologie der atmospharishen Trubung, Ber. Dtsch. Wetterdienstes, 13, 1-47.

Wang, F. Y., Chen, J. S., Chen, H. L. & Forsling, W. (1997). Surface properties of natural aquatic sediments. *Water Research,* 31, 1796–1800.

WETLabs. (2000). ac-9 Protocol Document, Revision B, 10 February 2000. (http://www.wetlabs.com/Products/pub/ac9/ac9proti.pdf)

WETLabs. (2004). Absorption and Attenuation Meters, 20 September 2004. (http://www.wetlabs.com/Products)

Whitlock, C.H., Poole, L.R., Usry, J.W., Houghton, W.M., Witte, W.G., Morris, W.D and Gurganus,E.A. (1981). Comparison of reflectance with backscatter and absorption parameters for turbid waters. *Appl. Opt.*,20(3),517-521.

Williamson, C.E., Stemberger, R.S., Morris, D.P., Frost, T.M. and Paulsen, S.G. (1996). Ultraviolet radiation in North American lakes: attenuation estimates from DOC measurements and implication for plankton communities. *Limnol. Oceanogr.*, 41, 1024-1034.

Zenveld, J. R. V., Kitchen, J. C, and Moore, C. (1994). The scattering correction of reflecting-tube absorption meters in Ocean Optics XII, Ackleson, S.G. ed., Proc. SPIE 2258, 44-55.

Zepp, R.G., T.V. Callaghan, and D.J. Erickson. (1998). Effects of enhanced ultraviolet radiation on biogeochemical cycles. *J. Photochem. Photobiol.* B, 46, 69-82.

Zirin, H. (1988). Astrophysics of the sun. *Cambridge University Press*, 98-100.